

**MAINBELT ASTEROIDS:
RESULTS OF ARECIBO AND GOLDSTONE RADAR
OBSERVATIONS OF 37 OBJECTS DURING 1980-1995**

CHRISTOPHER MAGRI

*University of Maine at Farmington
39 High Street--Preble Hall, Farmington, ME 04938
207-778-7369, fax -7365
e-mail: magri@maine.maine.edu*

STEVEN J. OSTRO, KEITH D. ROSEMA, AND MICHAEL L. THOMAS

*300-233, Jet Propulsion Laboratory, California Institute of Technology,
Pasadena, California 91109-8099*

DAVID L. MITCHELL

*Space Sciences Laboratory, Centennial Drive @ Grizzley Peak Blvd, University of California,
Berkeley, CA 94720*

DONALD B. CAMPBELL

Department of Astronomy, Space Sciences Bldg., Cornell University, Ithaca, NY 14853-6801

JOHN F. CHANDLER AND IRWIN I. SHAPIRO

Center for Astrophysics, 60 Garden St., Cambridge, MA 02138

AND

JON D. GIORGINI AND DONALD K. YEOMANS

*301-150, Jet Propulsion Laboratory, California Institute of Technology,
Pasadena, California 91109-8099*

June 1998

Draft of paper to be submitted to *Icarus*

OUTLINE

TITLE PAGE	1
ABSTRACT	2
1. INTRODUCTION	3
2. OBSERVATIONS	4
3. ANALYSIS STRATEGIES AND USE OF PRIOR INFORMATION	5
3.1. <i>Reference Ellipsoid Dimensions</i>	5
3.2. <i>Comments on Particular Targets</i>	7
3.3. <i>Radar Properties</i>	9
3.4. <i>Radar-Based Pole Constraints</i>	10
4. RESULTS FOR INDIVIDUAL TARGETS	12
5. STATISTICAL ANALYSES	17
5.1. <i>Correlations Between Radar/Optical Properties</i>	17
5.2. <i>Inter-Class Comparisons: Histograms</i>	17
5.3. <i>Inter-Class Comparisons: Statistical Tests</i>	17
6. DISCUSSION	21
7. CONCLUSION	24
ACKNOWLEDGMENTS	25
REFERENCES	26
FIGURE CAPTIONS	31
FIGURES 1 - 15	
TABLES I - XVI	

MAINBELT ASTEROIDS: RESULTS OF ARECIBO AND GOLDSTONE
RADAR OBSERVATIONS OF 37 OBJECTS DURING 1980-1995

Christopher Magri

Steven J. Ostro, Keith D. Rosema, and Michael L. Thomas

David L. Mitchell

Donald B. Campbell

John F. Chandler and Irwin I. Shapiro

Jon D. Giorgini and Donald K. Yeomans

ABSTRACT

We report detailed results of Arecibo and Goldstone radar observations of 30 mainbelt asteroids (MBAs) during 1980-1997. In addition to estimates of radar cross section, radar albedo, and circular polarization ratio, we obtain new pole constraints for several asteroids, with those for 21 Lutetia being particularly restrictive. We carry out statistical analyses of disc-integrated properties (radar albedo and polarization ratio) of all 37 radar-observed MBAs. There is good reason to believe that M asteroids tend to have higher radar albedos and a wider range of albedos than do the other taxonomic classes; there is no evidence that C and S MBAs have different albedo distributions; and there is some suggestion, worthy of future study, that primitive B, F, G, and P asteroids are not as radar-bright as C and S objects. There currently is no statistical evidence that different taxonomic classes have different polarization ratio distributions, despite suggestions to the contrary based on visual inspection of these distributions. The similarity between the C and S albedo distributions implies similar near-surface regolith bulk densities. If typical lunar porosities are assumed, then the hypothesis of ordinary chondritic composition for the S-class asteroids is more consistent with the radar data. Nevertheless, it is possible that some of these targets have high-porosity regoliths of stony-iron composition. Our M-class sample presumably contains both metallic objects (such as Kleopatra and, probably, Psyche) and less metallic objects, some of which might resemble enstatite chondrites.

1. INTRODUCTION

Radar observations are a potentially powerful source of otherwise unavailable information about asteroid physical properties. In 1980 a systematic program of radar observations of mainbelt asteroids (MBAs) was begun at Arecibo. It continued through 1992, just before the upgrading of the telescope began. Additionally, Goldstone observations of MBAs have been conducted since 1990. A total of 37 MBAs were observed during 1980-1997; see <http://echo.jpl.nasa.gov/asteroids/index.html> for a tabulated history of asteroid radar detections.

Ostro *et al.* (1985, henceforth OCS85) presented a summary of results for 20 MBAs. They reported that each asteroid appears much rougher than the Moon at some scale(s) between several meters and many kilometers. They also reported that the dispersion of MBA radar albedos implies substantial variations in surface porosity and/or metal concentration. Their highest albedo estimate, for 16 Psyche, was found to be consistent with a metallic composition and lunar porosities. de Pater *et al.* (1994) carried out Goldstone-VLA aperture synthesis observations of four asteroids, obtaining novel constraints on the pole directions of MBAs 7 Iris and 324 Bamberga. Mitchell *et al.* (1995) presented detailed analyses of echoes from 7 Iris, 9 Metis, 12 Victoria, 216 Kleopatra, and 654 Zelinda, which show evidence for large-scale topography. They found that Kleopatra is a more reflective radar target than Psyche, making it the best main-belt candidate for a metallic asteroid. Mitchell *et al.* (1996) presented detailed analyses of echoes from Ceres, Pallas, and Vesta. They found that Pallas has a somewhat denser surface than Ceres and that both objects are much smoother than the Moon at decimeter scales but much rougher (rms slopes $> 20^\circ$) on larger scales, whereas Vesta is unusually rough at small scales.

Here we present detailed analyses of Arecibo and Goldstone observations not discussed by Mitchell *et al.* (1995, 1996); these experiments involve 30 asteroids. We then carry out statistical analyses of disc-integrated properties (radar albedo and polarization ratio) of all 37 radar-observed MBAs. The next two sections describe our observations, which were similar for all the targets, and our analysis strategies, which were tailored for the strength of each target's echoes as well as for the nature of prior information about dimensions and spin vector. To the degree possible, we have relegated information about the observations, prior information, and analysis results to tables. Section 4 is devoted to comments on various aspects of our investigations of individual targets, and Section 5 presents our statistical analyses of the entire MBA radar dataset. Section 6 summarizes physical implications of our results.

2. OBSERVATIONS

Our observations used continuous-wave (cw) waveforms and yielded distributions of echo power vs. Doppler frequency. These echo power spectra constitute one-dimensional images that can be thought of as scans of radar brightness taken through a slit that is kept parallel to the asteroid's spin vector as it is moved across the asteroid's disc.

Most of our observations used transmission of a circularly polarized wave and simultaneous reception of echoes in the same circular as transmitted (the SC sense) and in the opposite circular (OC). Techniques for data acquisition and reduction were nearly identical to those described by Ostro *et al.* (1992).

Observations of a target with roundtrip echo time delay RTT consisted of transmission for approximately RTT seconds followed by reception for a similar duration. Power spectra usually were recorded in real time and were blocked into groups several minutes long. Reduction of data within each group produced a background-free OC/SC spectral pair in units of the r.m.s. noise. Our data format tags each spectral pair with several dozen relevant quantities, including the radar-cross-section equivalent of the r.m.s. noise, the start/stop-receive epochs, the transmitter frequency, the spectral resolution, and radar telescope parameters (*e.g.*, antenna gain, transmitter power, and system temperature). This format, which is being used in archiving data with the Planetary Data System, lets additional tags (*e.g.*, rotation phase and the radar cross section) be added during analysis of data and formation of sums of data subsets. Table I lists observational parameters for our experiments.

3. ANALYSIS STRATEGIES AND USE OF PRIOR INFORMATION

3.1. Reference Ellipsoid Dimensions

We model all targets as triaxial ellipsoids with axis lengths $2a \geq 2b \geq 2c$. We use axis ratios a/b and b/c that have been estimated for some objects (e.g., Magnusson 1995) as a byproduct of the amplitude-magnitude pole determination method (Zappalà *et al.* 1984). For the other targets, which have not been observed extensively enough to warrant such treatment, we estimate a/b from the published maximum lightcurve amplitude Δm :

$$\frac{a}{b} \approx 10^{0.4 \Delta m} \quad (1)$$

In these cases we generally assume a prolate spheroid ($b/c = 1.0$) and assign uncertainties to the axis ratios that we believe to be conservative. In particular, once we have chosen an error interval for a/b , we usually choose the interval for b/c by allowing the reference ellipsoid to be as flattened as it is elongated.

Reliable radiometric diameters D_{IR} -- usually derived from IRAS data -- have been published for most of our radar targets. For the three targets not observed by IRAS, we use TRIAD diameters (Bowell *et al.* 1979) and assign a 15% error that is intended to cover both estimation bias due to departures from a spherical shape (Brown 1985) and low precision relative to IRAS data.

Our method for determining the axis lengths from D_{IR} and the axis ratios depends on whether or not an estimate for the asteroid's pole direction is available. The projected area of a triaxial ellipsoid viewed at sub-observer latitude δ and rotational phase ϕ is

$$A_{\text{proj}} = \pi ab \left\{ \sin^2 \delta + \left(\frac{c}{b} \right)^2 \cos^2 \delta - \left[1 - \left(\frac{b}{a} \right)^2 \right] \left(\frac{c}{b} \right)^2 \cos^2 \delta \sin^2 \phi \right\}^{\frac{1}{2}} \quad (2)$$

where $\phi = 0^\circ, 180^\circ$ correspond to the maximum-breadth orientations. We can define a factor ζ such that the model ellipsoid's projected area averaged over all observations is equal to $\zeta \pi ab$. (Note that $c/a \leq \zeta \leq 1$.) When the pole direction -- and hence δ -- is known, the expectation value of ζ is $1/\pi ab$ times the mean of Eq. (2) over all ϕ :

$$\langle \zeta \rangle = \frac{2}{\pi} E(k) \sqrt{\sin^2 \delta + \left(\frac{c}{b} \right)^2 \cos^2 \delta} \quad (3)$$

Here $E(k)$ is the complete elliptic integral of the second kind,

$$E(k) = \int_0^{\frac{\pi}{2}} \sqrt{1 - k^2 \sin^2 \theta} \, d\theta \quad (4)$$

whose modulus k is given by

$$k = \sqrt{\frac{1 - \left(\frac{b}{a}\right)^2}{\left(\frac{b}{c}\right)^2 \tan^2 \delta + 1}} \quad (5)$$

If we know the sub-observer latitudes of IRAS and radar observations (δ_{IR} and δ_{rad}), we can insert them into Eq. (3) to compute area factors ζ_{IR} and ζ_{rad} . We can then use the model axis ratios and the IRAS diameter D_{IR} to determine the axis lengths of our reference ellipsoid. Setting $\pi D_{IR}^2 / 4 = \zeta_{IR} \pi ab = \zeta_{IR} \pi a^2 (b/a)$, we obtain the maximum diameter

$$2a = D_{max} = D_{IR} \sqrt{\frac{\left(\frac{a}{b}\right)}{\zeta_{IR}}} \quad (6)$$

from which we can then obtain $2b$ and $2c$. The two area factors can also be used to find the mean projected area viewed by the radar:

$$\langle A_{proj} \rangle = \frac{\zeta_{rad}}{\zeta_{IR}} \frac{\pi}{4} D_{IR}^2 \quad (7)$$

For elongated asteroids, incomplete IRAS or radar rotational phase coverage will increase the uncertainties associated with these estimates. If, for example, only two IRAS sightings were made and the target happened to be viewed nearly end-on both times, we would underestimate the axis lengths and $\langle A_{proj} \rangle$. The opposite problem (all sightings at maximum-breadth orientations) is equally likely. We therefore assume that incomplete phase coverage increases the variances of our estimators without biasing them.

The main hindrance in determining radar phase coverage for a given opposition is the lack of absolute phase information; none of the targets discussed here show unambiguous bandwidth variations which would establish the epoch at which $\phi = 0^\circ$. IRAS observations involve several brief sightings spaced weeks or months apart, so phase coverage is more difficult to assess. Hence we simply use the number of sightings as a guide to making subjective estimates of IRAS phase coverage quality.

The pole directions of 13 of our targets are unknown. In these cases we estimate the area factor ζ_{IR} by assuming that all viewing geometries are equally likely; that is, we numerically average Eq. (2) over all ϕ and $\sin \delta_{IR}$, then divide by πab . We can then use Eq. (6) to compute axis lengths as before, but with larger uncertainties which now depend on the degree of flattening. In the absence of pole information we assume that IRAS and the radar viewed the same projected area: $\langle A_{proj} \rangle = \pi D_{IR}^2 / 4$. Such estimates are again highly uncertain for flattened asteroids, except in cases where IRAS and the radar viewed the target at similar coordinates or at opposite points on the sky.

We can combine the estimated axis lengths with the rotation period P to derive $B_{max}(\delta_{rad}=0)$, the predicted echo bandwidth when the target is oriented with its maximum breadth D_{max} normal to the line of sight:

$$B_{\max}(\delta_{\text{rad}} = 0) = \frac{4\pi D_{\max}}{\lambda P} \quad (8)$$

For a sum of noise-free spectra obtained at all rotation phases, the observed zero-crossing bandwidth B will equal $B_{\max}(\delta_{\text{rad}}=0) \cos \delta_{\text{rad}}$.

3.2. Comments on Particular Targets

Prior information for all of our radar targets is listed in Table II. We now discuss the derivation of these parameters for some of these asteroids.

21 Lutetia

Magnusson (1995) lists the results of six different pole/shape studies, and Michałowski (1996) has recently produced a seventh (Table III). Two broadly defined prograde rotation states are favored, with each represented by six individual solutions. The individual solutions do not agree well with each other: predictions of sub-radar latitude range from 42° to 84° . On the other hand, a/b appears to be well determined, with Magnusson giving 1.3 as a "synthesis" value. We adopt this ratio with an error of ± 0.1 . There is poorer agreement for b/c . We discard the two extremely high values in Table III and choose $b/c = 1.15 \pm 0.15$ as an *a priori* estimate.

27 Euterpe

Euterpe was not observed by IRAS, but Dunham (1996) fits an elliptical profile to 1993 occultation data. The nine observed chords yield a "rather extreme" ellipse whose major and minor axes are 124.2 ± 1.7 km and 75.2 ± 1.3 km. The major axis is close to the TRIAD value of 118 km (Bowell *et al.* 1979; Morrison 1974), but the high degree of flattening is surprising, given a maximum lightcurve amplitude of only 0.15 mag (Lagerkvist *et al.* 1989).

These data can be reconciled if we model Euterpe as a triaxial ellipsoid viewed with the line of sight roughly parallel to the intermediate diameter during the occultation. The measured maximum value of Δm yields the rough estimate $a/b = 1.15 \pm 0.15$. This implies that $b/c = 1.43 \pm 0.20$ in order to reproduce the occultation ellipse, but we note that the observed chords do not densely cover the profile. Hence we adopt the "safe" value $b/c = 1.3 \pm 0.3$, covering every possibility from a prolate spheroid to the shape implied by the occultation fit. With these axis ratios we expect $2c$ to be approximately $(1.43/1.3)$ times 75 km, or 83 km. If the infrared observations were made pole-on, we would have $D_{\text{IR}} = 2\sqrt{ab}$; our adopted axis ratios would then imply axis lengths 127 x 110 x 85 km. This value of $2c$ is roughly what we were expecting, whereas IR observations away from the pole would yield larger dimensions. We therefore adopt these lengths for our reference ellipsoid.

78 Diana

Harris and Young (1989) determine a rotation period of 7.23 hr, based on observations from 1980. They compare their lightcurve to that obtained by Taylor *et al.* (1976) for 1969 data, and thereby argue that "the pole of Diana probably lies within about 20° of the direction of the 1980 observations," which was $(\lambda, \beta) = (33^\circ, +13^\circ)$. We adopt this as our pole direction, with a 20° error radius.

80 Sappho

Magnusson (1995) does not list any pole determinations for this object, but Michałowski (1993) has obtained a pair of prograde solutions that imply nearly pole-on viewing for both Arecibo and IRAS.

The formal errors listed for the pole longitudes and latitudes are about six degrees, but we will assign larger errors: $|\delta_{\text{rad}}| = 75^\circ \pm 15^\circ$ and $|\delta_{\text{IR}}| = 78^\circ (+12^\circ, -18^\circ)$.

Michałowski's model ellipsoid is long and flat, with $a/b = 1.36 \pm 0.20$ and $b/c \approx 1.9 \pm 0.3$. He notes that the large errors on the axis ratios probably result from the fact that only one of the four lightcurves used absolute photometry.

Since Michałowski's pole solutions are based on few lightcurves, we redid the analysis pretending that no published solutions exist. We used the maximum lightcurve amplitude $\Delta m = 0.40$ mag (Lagerkvist *et al.* 1996) to obtain the rough estimate $a/b = 1.45 \pm 0.25$. For simplicity we took Sappho to be a prolate spheroid ($b/c = 1.0$), but we allowed b/c to be as high as 1.7 in constructing error estimates. The resulting values of $B_{\text{max}}(\delta_{\text{rad}}=0)$ and $\langle A_{\text{proj}} \rangle$ are essentially the same as those obtained via Michałowski's solutions, so we adopt the latter.

84 Klio

Klio's rotation period and shape are not well constrained by published lightcurves. Zeigler and Wampole (1988) obtain a period of 5.80 ± 0.02 hr based on three nights of observations in October 1985. Their composite lightcurve has an amplitude of only 0.06 ± 0.01 mag, and has three maxima and minima per rotational cycle. On the other hand, the single lightcurve published by Weidenschilling *et al.* (1990) was obtained only one week later, but is at best "marginally compatible" with the results of Zeigler and Wampole. Unless two data points taken at high air mass are rejected, this lightcurve implies a period significantly longer than six hours.

Because photometry of Klio covers just one longitude, we cannot decide whether the low lightcurve amplitude results from a nearly spherical shape or from nearly pole-on viewing. Our *a priori* model is a sphere whose diameter is within 25% of D_{IR} . The predicted 13-cm $B_{\text{max}}(\delta_{\text{rad}}=0)$ is equal to 2190 ± 590 Hz divided by the rotation period in hours. Future photometry could greatly reduce the errors on the model's parameters.

105 Artemis

No pole determination been published for Artemis, and the rotation period is uncertain. Schrober *et al.* (1994) estimate that $P = 16.84 \pm 0.01$ hr, but the composite lightcurve they present appears to have much greater scatter than their stated precision would indicate. We adopt this period estimate but assign a 3-hr uncertainty. An incorrect value for the period would primarily influence our radar-based pole constraints; it would not affect the quality of the radar phase coverage, which was poor for *any* long rotation period.

139 Juewa

Juewa's rotation period is two-fold ambiguous, with either 20.9 hr or 41.8 hr permitted by the photometric data. Michałowski (1993) has published the only pole determination for this object; he states that 20.91 hr is the most probable sidereal period, but notes that this value "may be completely wrong." Hence we consider the implications of both of these candidate periods for obtaining radar-based pole constraints.

Michałowski obtains a single pole solution at $\lambda = 117^\circ \pm 14^\circ$, $\beta = +50^\circ \pm 12^\circ$. The corresponding axis ratios for a model ellipsoid are $a/b = 1.21 \pm 0.20$ and $b/c = 1.68 \pm 0.45$. This solution has not been confirmed by independent studies, and it does not yield an unambiguous sidereal period and rotation sense. Therefore we will increase Michałowski's stated errors on the pole direction. We assume that the pole lies within a 25° radius of $(\lambda, \beta) = (117^\circ, +50^\circ)$, and that the axis ratios are $a/b = 1.2 \pm 0.2$ and $b/c = 1.7 \pm 0.5$.

192 Nausikaa

There previously was a discrepancy in Nausikaa's taxonomic class: it was designated S on the Tholen system, but V0 according to the G-mode classification (Tholen 1989). Birlan *et al.* (1996) recently repeated the G-mode analysis using revised IRAS albedos; they now assign Nausikaa to the S1 subclass.

230 Athamantis

The rotation period of this asteroid is probably 24 hr, but a value of 12 hr is not ruled out (Harris and Young 1989). A 24-hr period implies poor phase coverage for the radar data.

324 Bamberga

Bamberga was discussed by de Pater *et al.* (1994), who considered monostatic data from Arecibo and Goldstone along with bistatic Goldstone-VLA measurements. Here we consider only the monostatic spectra, largely in order to give separate tabular summaries of the 13-cm and 3.5-cm data. There is only one minor revision to note. The latest IRAS estimate of Bamberga's diameter is 229 ± 7 km (Tedesco 1997); this is 5% smaller than the older IRAS value of 242 ± 7 km used by de Pater *et al.*, but agrees with the occultation diameter estimate of 228 ± 2 km (Millis *et al.* 1989). This downward revision of D_{IR} results in radar albedo estimates 10% higher than those of de Pater *et al.*

Bamberga has a maximum lightcurve amplitude of 0.05 mag (Lagerkvist *et al.* 1996), which implies that our reference ellipsoid has a maximum breadth $2a$ nearly as large as the 242 km value used by de Pater *et al.* for their model sphere. This means that the predicted 13-cm and 3.5-cm $B_{\text{max}}(\delta_{\text{rad}}=0)$ values -- and hence the pole constraints -- are essentially unchanged from that paper.

796 Sarita

This asteroid was classified XD by Tholen (1989), based on (B-V) and (U-B) colors. Both Rivkin *et al.* (1995) and Belskaya and Lagerkvist (1996) treat it as an M-class object. The visual albedo $p_v = 0.197 \pm 0.013$ is more than twice as large as the albedo of any of the 58 unambiguously classified D and P objects observed by IRAS, but is typical of M-class asteroids ($\langle p_v \rangle = 0.170$, s.d. = 0.047, N = 36).

3.3. Radar Properties

Almost all radar data considered in this paper are Doppler spectra simultaneously received in orthogonal (OC and SC) circular polarizations. Single scattering from large, smooth "facets" gives a purely OC echo. Processes which can produce both SC and OC echo power include single scattering from wavelength-scale near-surface structure and multiple scattering of all sorts.

We estimate bandwidth B from the innermost zero-crossings of spectra which have been formed, first, by summing all data together, and second, by averaging the positive- and negative-frequency halves of these sums. Such "folded" spectra are $\sqrt{2}$ stronger. We then smooth the folded sum to an appropriate effective frequency resolution. Wishing to smooth just enough to minimize the influence of random baseline noise on our estimate, we compute B for several frequency resolutions. These values sometimes exhibit large fluctuations at fine resolutions, but they become more stable, and increase slowly and steadily at coarser resolutions. In such cases, stated values of B refer to an optimal resolution at the boundary between these two regimes; otherwise we use the raw resolution as the optimal resolution. Uncertainties are subjectively determined by inspecting the fluctuations in B near the optimal resolution.

An alternative, more sophisticated method for estimating B would be to fit a model spectrum to the data, based on an assumed parametric form for the target's shape and angular scattering law (*e.g.*, Mitchell *et al.* 1995, 1996). Yet the asteroids discussed here have radar datasets too weak, or else axis lengths too imprecisely known, for such fits to yield accurate, meaningfully interpreted results. Hence we rely on the subjective method outlined above.

Another bandwidth estimator is the equivalent bandwidth B_{eq} , defined as

$$B_{eq} = \frac{\left(\int S(f) df\right)^2}{\int S^2(f) df} = \frac{\left(\sum_i S_i\right)^2}{\sum_i (S_i)^2} \Delta f \quad (9)$$

where Δf is the frequency channel width and S_i is the signal in the i th channel (Tiuri 1964). A rectangular spectrum has $B_{eq} = B$, while any other spectral shape yields $B_{eq} < B$. Hence it serves as a conservative lower limit on B . We find that B_{eq} is much less sensitive than zero-crossing bandwidth B to frequency smoothing. We estimate it in the same manner described above for B , except that we use unfolded spectra.

Integration of "raw" (unsmoothed and unfolded) OC and SC spectra yields the radar cross sections σ_{OC} and σ_{SC} . Radar cross section is equal to the projected area of a metal sphere (*i.e.*, a perfect isotropic scatterer), located at the target's position, which would produce the echo power received from the target. We occasionally consider the "total circular" cross section $\sigma_{TC} = \sigma_{OC} + \sigma_{SC}$ as well. The cross section uncertainty due to random receiver noise is estimated as the noise power within a bandwidth equal to B_{eq} . This is dwarfed, however, by absolute flux calibration errors, which are typically at least 25%.

Normalization of the radar cross sections to target projected area gives the radar albedos, $\hat{\sigma}_{OC}$, $\hat{\sigma}_{SC}$, and $\hat{\sigma}_{TC}$. We also use the circular polarization ratio $\mu_C = \sigma_{SC}/\sigma_{OC}$. Systematic errors cancel out of this ratio, so the error propagates solely from the receiver noise in the OC and SC channels. To be conservative, however, we assign the larger of these two cross section errors to *both* cross sections before computing μ_C and its uncertainty. All errors on ratios in this paper have been estimated as described in the Appendix of Ostro *et al.* (1983).

Two asteroids (41 Daphne and 393 Lampetia) were also observed in orthogonal linear polarizations. Here we define cross sections σ_{SL} and σ_{OL} , as well as "total linear" cross section $\sigma_{TL} = \sigma_{SL} + \sigma_{OL}$. Single scattering from smooth facets produces a purely SL echo, so the linear polarization ratio $\mu_L = \sigma_{OL}/\sigma_{SL}$ depends on multiple scattering and wavelength-scale structure in much the same way that μ_C does. However, because of the Arecibo telescope's feed rotation between transmit and receive times, the polarization of the "OL" received wave was not orthogonal to that of the transmitted signal, strongly biasing our μ_L estimates upward and undermining their value.

3.4. Radar-Based Pole Constraints

Consider an average of spectra obtained at all rotation phases. As noted earlier, the observed zero-crossing bandwidth B will equal $B_{max}(\delta_{rad}=0) \cos \delta_{rad}$ in the absence of noise. If we now assume that equality indeed holds, we can use the measured value of B to determine the sub-radar latitude:

$$|\delta_{rad}| = \cos^{-1} \left(\frac{B}{B_{max}(\delta_{rad}=0)} \right) \quad (10)$$

Given that B and $B_{max}(\delta_{rad}=0)$ will have associated uncertainties, this relation restricts the object's pole to a pair of annuli on opposite sides of the celestial sphere. In cases where we can place only a lower limit on B , we can still use Eq. (10) to exclude from consideration two circular regions on the sphere, one centered on the target direction and one on the opposite direction.

Unless otherwise stated our assigned uncertainties are estimated standard errors. In assigning these values, we have tried to account for systematic as well as statistical sources of error in a conservative manner.

4. RESULTS FOR INDIVIDUAL TARGETS

Weighted spectral sums for all radar experiments are displayed in Fig. 1. Echo power, in units of standard deviations of the noise, is plotted vs. Doppler frequency. 0 Hz corresponds to echoes from the center of mass, as predicted by our ephemerides.

Table IV lists the radar parameters -- SNR, B_{eq} , B , μ_C , σ_{OC} , and $\hat{\sigma}_{OC}$ -- obtained for each experiment listed in Table II. Table V gives the average polarization ratio and OC albedo for each MBA radar target, taking into account all data obtained since 1980. Note that the eight asteroids recently discussed by Mitchell *et al.* (1995, 1996) are included here. The same information is given in the second part of Table V, but is ordered from high μ_C to low; the third part does the same thing for $\hat{\sigma}_{OC}$. Lastly, Table VI shows the pole constraints derived by combining the measured bandwidths given in Table IV with the predicted maximum-breadth bandwidths listed in Table II. Comments on particular targets follow.

5 *Astraea*

Given the similar viewing aspects during the 1983 and 1987 experiments, and given the radar SNRs (23 and 24), one would expect similar echo spectra. This is what we find. In particular, the statistically identical zero-crossing bandwidths suggest that, despite incomplete phase coverage, we captured *Astraea*'s maximum-breadth orientations during both experiments.

7 *Iris*

Mitchell *et al.* (1995) analyzed monostatic data obtained at Arecibo in 1980 and 1984 and at Goldstone in 1991. They note that the polarization ratios obtained for these three experiments are significantly different from each other, suggesting "the possibility of either regional or scale-dependent variations in small-scale structure."

Iris was observed again from Goldstone in 1995 (Fig. 1), yielding a particularly large μ_C value. The results to date (Table VII) are consistent with the hypothesis that equatorial views and short observing wavelengths yield higher polarization ratios.

16 *Psyche*

OCS85 presented 1980 results for this object, the largest M-class asteroid. They interpreted *Psyche*'s radar albedo -- at 0.29, the highest then known for any main-belt object -- as evidence of a largely metallic composition.

1985 results for $\hat{\sigma}_{OC}$ and μ_C are consistent with the 1980 results. The pole constraint $56^\circ \leq |\delta_{rad}| \leq 70^\circ$ derived from the 1980 data (Table VI) conflicts with the prediction $\delta_{rad} = 45^\circ \pm 10^\circ$ obtained via photometric pole determinations (Table II). Yet the SNR of the 1980 radar data is only 10, so we do not give much weight to this discrepancy.

18 *Melpomene*

We obtain consistent estimates of radar albedo and polarization ratio for the 1985 Arecibo and 1995 Goldstone experiments. The large polarization ratio indicates considerable near-surface roughness at decimeter scales.

The 3.5-cm data have high enough SNR to reveal a broad spectral feature which shifts from negative to positive Doppler over 60° of rotation. As shown in Fig. 2, this feature is evident on at least two of the three individual dates which covered these rotation phases. Such shifts are predicted for rotating limb-darkened ellipsoids (Jurgens 1982); the middle panels in Fig. 2 represent the maximally

"end-on" radar view of Melpomene. We also expect an identical shift one-half rotation later, but these phases were viewed on only one date, so the SNR is insufficient to test the prediction.

Pole constraints derived from the two experiments are depicted in Fig. 3. The two optical pole solutions of Hoffmann and Geyer (1990) have large uncertainties, so neither one is ruled out by the radar data.

19 Fortuna

Although the projected area of this G-class asteroid is not well determined, the OC cross section estimates for the 1982 and 1986 radar experiments are in close agreement. The circular polarization ratios also agree to within the errors.

21 Lutetia

Our radar observations resulted in the strong (SNR = 15) summed spectrum shown in Fig. 1. The zero-crossing bandwidth is $B = 58 \pm 10$ Hz, where we set the uncertainty to twice the frequency resolution. This yields the 95% confidence interval $78^\circ \leq |\delta_{rad}| \leq 85^\circ$.

Let us consider possible effects of incomplete radar phase coverage. The instantaneous zero-crossing bandwidth for noise-free spectra and a triaxial ellipsoid target is given as a function of rotation phase ϕ via

$$B(\phi) = B_{\max}(\delta_{rad}=0) \cos \delta_{rad} \sqrt{\cos^2 \phi + \left(\frac{b}{a}\right)^2 \sin^2 \phi} \quad (11)$$

Our observations covered about 120° of rotational phase, with only a small (25°) gap within this interval. It is conceivable, but unlikely, that our sampled phases are centered on a minimum-breadth orientation, in which case the square-root factor in the above equation never exceeds 0.948 ± 0.024 . The equation would then imply that $\cos \delta_{rad} = B / [(0.948 \pm 0.024) B_{\max}(\delta_{rad}=0)]$. Let us use the value 0.900 -- two standard deviations in the direction of weaker pole constraints -- in the right-hand-side denominator. We then obtain the result $76^\circ \leq |\delta_{rad}| \leq 85^\circ$ at the 95% confidence level.

Fig. 4 displays this constraint as a pair of narrow annuli in ecliptic coordinates. The figure also plots the various pole determinations listed in Table III. Most of these optically derived solutions are strongly incompatible with the radar data. The exceptions are the solutions published by Michałowski (1993) and by Lagerkvist *et al.* (1995), with the latter results favored. We use these two solutions to revise our reference ellipsoid. The axis ratios are now less precisely known than before. The two a/b values agree well, so we estimate that $a/b = 1.25 \pm 0.15$. The b/c ratios do not agree at all, and we feel that Michałowski's result $b/c \approx 2.7 \pm 1.0$ is both too high and too imprecise to be given much weight. We therefore take the Lagerkvist *et al.* value and assign a large subjective error: $b/c = 1.4 \pm 0.3$.

The properties of our revised reference ellipsoid are listed in Table VIII. The *a posteriori* adjustment made to $B_{\max}(\delta_{rad}=0)$ does not change (to the nearest degree) the radar-based pole constraint obtained earlier: $76^\circ \leq |\delta_{rad}| \leq 85^\circ$.

Lutetia has the lowest radar albedo measured for any M-class MBA. This asteroid has already been noted as atypical for its taxonomic class. Its infrared spectrum is unusually flat (Howell *et al.* 1994), and optical polarimetry reveals a large negative polarization depth and inversion angle (Dollfus *et al.* 1989; Belskaya and Lagerkvist 1996). Belskaya and Lagerkvist state that Lutetia's infrared spectrum and polarimetric properties are better explained by a carbonaceous chondritic composition than by metallic composition. Rivkin *et al.* (1997) recently detected the 3- μ m water of hydration feature, further evidence that Lutetia is largely nonmetallic.

41 Daphne

Daphne was observed for six days in 1985. Three of these dates were devoted to dual-circular polarization measurements, while the other three were used to obtain dual-linear polarization data. The weighted spectral sums for both the dual-circular and the dual-linear observing modes are shown in Fig. 5, and the corresponding measured parameters are shown for both experiments in Table IX.

If Daphne's surface is smooth at scales within an order of magnitude of the observing wavelength (13 cm), we expect the received echoes to have (a) low values of both μ_C and μ_L , and (b) σ_{OC} roughly equal to σ_{SL} . One can see from Fig. 5 that the OC and SL signals are indeed qualitatively similar, and the cross sections listed in Table IX are consistent within the stated errors. Although μ_L is somewhat higher than μ_C , this conflict is an illusion, since feed rotation during the 18-minute echo time delay strongly biases μ_L upward.

We find that bandwidths B_{eq} and (especially) B are larger for the SL than for the OC echo, for all combinations of folding and frequency smoothing (see Table IX). (Note that these two datasets represent similar rotation phase coverage.) Since the cross sections agree well (as discussed earlier), and since the SNR is only about 12 for each of these two spectral sums, we are not concerned about this apparent discrepancy. We simply estimate that B must be at least as large as the smaller (OC) value: $B \geq 540$ Hz.

78 Diana

We find (with 95% confidence) that $|\delta_{rad}| \leq 48^\circ$ for Diana. Our radar observations were probably closer to equatorial than to polar viewing, which is consistent with the Harris and Young (1989) pole.

84 Klio

The summed OC signal for Klio lets us place only a lower limit on the zero-crossing bandwidth: $B \geq 105$ Hz. Since $B_{max}(\delta_{rad}=0) \geq B$, this is also a lower limit on $B_{max}(\delta_{rad}=0)$. Given the assumption that $B_{max}(\delta_{rad}=0) = 4\pi D/\lambda P$, we obtain the inequality $P \leq 4\pi D/\lambda B$. This tells us that $P \leq 32$ hr at the 95% confidence level.

97 Klotho

Klotho was observed at 13 cm in 1981 (OCS85). Only OC spectra were obtained, and these were weak (SNR = 6).

OC and SC echoes were simultaneously received in the 1993-94 Goldstone 3.5-cm experiment. The OC signal has SNR = 14. The Goldstone data achieve much better phase coverage than do the Arecibo data, spanning about three-quarters of a full rotation.

The 1981 data result in the weak pole restriction $|\delta_{rad}(1981)| \leq 71^\circ$. The Goldstone experiment yields a more interesting result: $|\delta_{rad}(1993-94)| \leq 37^\circ$ at 95% confidence. Thus it is probable that Goldstone's view of Klotho was closer to equatorial than to polar. These two pole constraints are graphically depicted in Fig. 6. The 1981 data do not improve the 1993-94 constraint.

105 Artemis

Some of the data obtained during the 1988 experiment were delay measurements obtained for astrometric purposes (Ostro *et al.* 1991a). For the cw data, the OC signal is strong (SNR = 28), but the zero-crossing bandwidth is nonetheless difficult to measure precisely. As shown in Fig. 7, the folded sum has wide, extremely weak spectral wings which, if real, are evidence of highly specular scattering. Yet these might be due to random noise fluctuations. Hence we estimate that $B \geq 70$ Hz.

We note a possible variation in μ_C across the surface. The cw data cover two rotation phase intervals, corresponding to two days of observations. Summed spectra from each of these two dates (Fig. 8) yield statistically identical OC cross sections (Table X), but polarization ratios which differ by roughly

two standard deviations: 0.22 ± 0.05 vs. 0.06 ± 0.05 . Observations with the upgraded Arecibo telescope should easily reveal whether or not this apparent difference is real.

393 *Lampetia*

Lampetia's rotation period has a factor-of-two ambiguity, with 38.7 hr preferred over 19.35 hr (Scaltriti *et al.* 1979). Figure 9 shows the phase coverage of our Arecibo data for each of these two possible periods, along with smoothed, summed spectra obtained on the five observing dates. In the central polar plots in this figure, each radial line segment represents a four-minute block of data which contributed to the spectral sum. The length of the line segment is proportional to the r.m.s. noise level for those data; the angular position of the line segment is the target's mean rotational phase (relative to an arbitrarily chosen epoch) over that four-minute interval.

Multi-date OC and SL summed spectra are shown in Fig. 10. We received polarized echoes on each of the five dates, with SNR ranging from 17 to 26 (see Table XI). There is no significant day-to-day variation in σ_{OC} or σ_{SL} , but the weighted mean value of σ_{SL} is about 25% lower than that of σ_{OC} . We also find that σ_{TL} is about 25% lower than σ_{TC} , suggesting a systematic difference in the linear and circular measurements. This difference in cross-sections is not due to variations in projected area, as neither of the two phase-coverage patterns depicted in Fig. 9 offers any way to have an elongated *Lampetia* viewed nearly end-on for both of the SL dates but none of the three OC dates. Telescope pointing errors, or else some unidentified system problem, may be responsible for the apparent difference between our σ_{OC} and σ_{SL} estimates.

In principle, bandwidth variations over the course of the experiment could help us to resolve the period ambiguity. Hence we created and analyzed weighted spectral sums within various rotation phase intervals. For a 38.7 hr period, the top half of Fig. 9 shows that the appropriate phase intervals are those five which correspond to the five observing dates. (We refer to these sums by date and polarization sense: 16 OC, 19 SL, etc.) The 16 OC and 20 SL data overlap in phase if $P = 19.35$ hr (Fig. 9, bottom half), so we also analyzed a "16 OC + 20 SL" spectrum that includes all data from both of these dates. (The systematic cross section discrepancy discussed earlier should have little influence on the width of this combined spectrum.)

The maximum lightcurve amplitude of 0.14 mag (Lagerkvist *et al.* 1989) indicates that bandwidth variations are likely to be of order ten percent. This ruled out the use of the zero-crossing bandwidth B , as our estimates of B for a given spectrum varied by 10% depending on how much smoothing in frequency we used and on whether or not we folded the spectrum. Hence we tested a number of other bandwidth estimators, settling on two which were less prone to these problems: the equivalent bandwidth B_{eq} ; and the width $B_{2\sigma}$ between the innermost two-sigma crossing points.

Results are listed in Table XI. Although bandwidth differences are present at the 5-10% level, we do not find credible evidence for periodic variations. Hence the bandwidth estimates do not favor either rotation period.

What is clear from Fig. 9 is that there is real variation in spectral shape. Subtracting one side of each spectrum from the other side (not shown) confirms that statistically significant off-center peaks exist for some spectra. We chose not to use the skew statistic to quantify this asymmetry, because that estimator is highly sensitive to noise fluctuations near the spectral edges. Instead we computed the three location parameters given in Table XI: the midpoint $f_{2\sigma}$ between the innermost two-sigma crossing points; the median f_{med} (which has half the integrated echo to each side); and the frequency f_{peak} of the maximum signal. A spectrum with positive skew -- that is, one which has an extended positive-frequency tail -- would have $f_{2\sigma} > f_{med} > f_{peak}$. This is just what is observed for 19 SL and 20 SL, while we see the opposite trend (negative skew) for 16 OC and 17 OC. Of the five single-date spectral sums, only 18 OC is nearly symmetric.

This skew is important because it is in opposite senses for 16 OC and 20 SL, as seen both in Fig. 9 and in Fig. 11. (This is why the "16 OC + 20 SL" spectrum is symmetric by the criterion described above.) The bottom half of Fig. 9 indicates that the views on these two dates were almost identical for a 19.35-hr period, so it is difficult to see why they should produce different spectral shapes. Unfortunately, the changes in asymmetry do not easily fit a 38.7-hr period, either. For example, if Lampetia were a limb-darkened ellipsoid, the echo's shape and centroid would vary at twice the rotation frequency (Jurgens 1982), leading us to predict (incorrectly) the same shape for 16 OC and 20 SL (see Fig. 9, top half). Those two spectra could be explained by a lopsided target -- say, an ovoid -- but we then would expect the 17 OC and 19 SL echoes to look more like the 20 SL and 16 OC echoes, respectively, contrary to what is actually observed.

In all, our data indicate that Lampetia is not spherical, not uniformly scattering, or both, but the SNR and (more importantly) rotational phase coverage are insufficient to support more specific conclusions about shape. Hence we are unable to resolve the period ambiguity, and will examine the implications of each candidate period for interpretations of the radar cross section and bandwidth of our multi-date OC spectral sum.

a. $P = 38.7$ hr

We estimate that $B = 105 \pm 10$ Hz. Inserting this zero-crossing bandwidth and a 38.7-hr period into Eq. (8), we find that the target's maximum breadth is given by $D_{\max} \geq (146 \pm 14 \text{ km}) / \cos \delta_{\text{rad}}$. We now set D_{\max} equal to $(146 \pm 14 \text{ km}) / \cos \delta_{\text{rad}}$, keeping in mind that off-center rotation would make this an overestimate while incomplete phase coverage could make it an underestimate.

Given the IRAS diameter estimate of 97 ± 31 km, we can best satisfy this relation for D_{\max} by maximizing $\cos \delta_{\text{rad}}$ -- that is, by setting $\delta_{\text{rad}} \approx 0$ (equatorial view). On this assumption, the radar data indicate that Lampetia's maximum breadth is 146 ± 14 km, and hence we must rule out the lower half of the IRAS confidence interval (97 ± 31 km) as extremely unlikely. Data for two of the three IRAS sightings in fact indicate a diameter of roughly 125 km, while the third gives 45 - 75 km. The radiometric TRIAD diameter estimate (Bowell *et al.* 1979) is 117 km. Combining our radar estimates with the infrared data (but ignoring the third IRAS sighting), we use an equivalent spherical diameter $D_{\text{eff}} = 125 \pm 10$ km in our analysis.

b. $P = 19.35$ hr

Radar constraints on Lampetia's physical properties are much less interesting if the shorter period is correct. For example, repeating the preceding analysis for this period leads to the result $D_{\max} = (73 \pm 7 \text{ km}) / \cos \delta_{\text{rad}}$. If we now equate this to the IRAS diameter estimate $D_{\text{IR}} = 97 \pm 31$ km, we obtain the 95% confidence interval $|\delta_{\text{rad}}| \leq 64^\circ$ for the sub-radar latitude. Hence unless we make additional assumptions, we can place no new constraints on the diameter and only weak constraints on the pole direction.

532 Herculina

Our Herculina data are weak. Moreover, data taken on different dates for the same rotation phase interval give highly discrepant OC cross sections. Observations of 2 Pallas made on these dates had unusually low SNR relative to data taken at two other oppositions (Mitchell *et al.* 1996), so we believe that system problems were responsible for Herculina's strong σ_{OC} variations. We analyze the weighted sum of spectra taken on all four observing dates, but assign a 50% error to our cross sections.

5. STATISTICAL ANALYSES

Table XII lists means, standard deviations, ranges, and sample sizes for μ_C and $\hat{\sigma}_{OC}$ as a function of taxonomic class. In addition to the five M objects, the 14 S objects, the seven C objects, and Vesta (V), we have nine objects which are listed as B, FC, G, P, or CP by Tholen (1989). The B, F, G, and P classes are similar to the C class in that they are mineralogically associated with primitive meteorites (Bell *et al.* 1989; Gaffey *et al.* 1989); here we group them into the "BFGP" class for analysis purposes. BFGP, in other words, consists of primitive radar targets which are not, or might not be, type C. Note that this group includes seven of the nine "C" objects discussed by OCS85.

5.1. Correlations Between Radar/Optical Properties

Figure 12 displays our estimated radar albedos and polarization ratios plotted as functions of radiometric diameter D_{IR} and visual geometric albedo p_V . For each of the variable pairs represented in these plots, linear regression analysis (Table XIII) yields the probability that the null hypothesis (uncorrelated variables) is valid. Small listed probabilities imply that we should instead favor the alternative hypothesis (correlated variables). The last column of Table XIII indicates that for the full sample of 37 objects, the trends that are significant (at the 95% level or higher) are that μ_C is correlated with p_V while $\hat{\sigma}_{OC}$ is anticorrelated with D_{IR} . Yet if we remove Ceres from the latter analysis, the significance of the trend is lowered from 95.5% to 92.5%. Similarly, ignoring the high- μ_C object Vesta reduces the significance of the μ_C vs. p_V correlation from 97.5% to 83%. Within individual classes, the only significant relationship we find is that $\hat{\sigma}_{OC}$ is anticorrelated with p_V for the five M-class objects. We conclude that inter-class comparisons of radar scattering properties will be little influenced by underlying dependencies on D_{IR} and p_V .

Figure 13 shows polarization ratio as a function of OC albedo for all radar targets. Linear regression (Table XIII) shows that there is no significant correlation for the full sample. The only single-class trend which is significant at the 95% level is for the M-class MBAs, but this is due to the high-albedo, low- μ_C object Kleopatra.

5.2. Inter-Class Comparisons: Histograms

Do the different taxonomic classes have different distributions of radar albedo or polarization ratio? The four classes considered are those for which we have more than one member: BFGP, C, S, and M. Figure 14 shows the univariate μ_C and $\hat{\sigma}_{OC}$ distributions for each of these classes. The corresponding distributions for the full sample (including 4 Vesta) are displayed in Fig. 15. Noteworthy features include the broad, flat μ_C distribution for S-class MBAs, the low albedos and polarization ratios for BFGP, the high mean M-class albedo, and the similarity between $\hat{\sigma}_{OC}$ distributions for C and S objects.

Restricting our attention to the albedo histograms, we see that there is only slight overlap between BFGP and M, and that the mean albedo is significantly higher for the M-class objects. These two populations clearly differ in their $\hat{\sigma}_{OC}$ properties. Another firm conclusion is that there is very little difference between the S and C distributions. (Note that the means and standard deviations listed in Table XII are nearly identical.) Other comparisons are more ambiguous – for example, whether M-class MBAs have higher albedos than S-class objects, or whether the primitive C and BFGP classes differ significantly from each other.

5.3. Inter-Class Comparisons: Statistical Tests

These visual impressions cannot substitute for inter-class statistical tests. Furthermore, we cannot simply compare carry out six pairwise comparisons between our four samples. To see this,

suppose that the four $\hat{\sigma}_{oc}$ samples were drawn from *identical* parent populations. Let us now compare two sample means at a time -- using, say, a *t*-test (Zar 1996, pp. 123-130) -- and let us adopt the 95% significance level. This means that we have a 95% probability of accepting the null hypothesis (equal population means) if the two population means are in fact equal. Given that we have postulated identical parent distributions, this amounts to a 95% probability of obtaining the right answer. If each of three independent comparisons (for example, M vs. BFGP, M vs. C, and M vs. S) has a 95% probability of yielding the correct answer, the probability that *all three* results are correct is only $(0.95)^3 \approx 0.86$. There is, in other words, a 14% chance of incorrectly finding at least one difference between these three pairs of means. The rest of the calculation is complicated by the fact that the other three pairwise tests are not independent of the first three. For example, accepting the null hypothesis for M vs. S and for M vs. C implies that the S and C means are not extremely different from each other, so the probability of concluding that they are identical is greater than 95%. For the relatively simple case of equal-size samples with normally distributed means, the probability of correctly accepting the null hypothesis for all six comparisons is 80%.

Hence a test with a 5% chance of yielding "false positives" (Type I errors) can yield an overall error rate of 20% when applied to six sample pairs. Essentially, the more samples we draw, the greater the probability that we will obtain at least one unrepresentative sample skewed toward extreme values. Note that we cannot remedy this problem by increasing sample sizes. Larger samples are indeed less likely to have a large fraction of members with inordinately high (or low) values; but tests carried out on pairs of such samples are sensitive to smaller differences (since the standard errors on the sample means are smaller). We conclude that we must consider all four classes simultaneously, rather than inspecting Table XII for potentially interesting differences and then applying two-sample tests.

Let us first analyze the radar albedo data. All statistical test results (probabilities) discussed below are listed in Table XIV. In that table, moderate and large tabulated probabilities indicate samples whose distributions are similar to each other (or to a specified theoretical distribution), whereas small probabilities imply significant differences.

Because our samples are small, skewed, or both, it is dangerous to assume that they are drawn from a normal distribution. Hence we rely heavily on robust and nonparametric tests, as implemented in the Prophet statistical software package (BBN Technologies 1997). The Shapiro-Wilk test (Conover 1980, pp. 363-366) is used to evaluate whether or not a given population is normally distributed; it measures how well the ordered data for that sample agree with the "normal scores," that is, with the expected ordered values for a sample of equal size taken from a normal distribution. (We do not use the Kolmogorov goodness-of-fit test because it is conservative when the mean and variance of the hypothesized normal distribution must be estimated from the data [Conover 1980, p. 357].) For the BFGP sample, the probability that the null hypothesis (normal parent distribution) is valid is only 0.013, so we conclude that it is unsafe to accept this hypothesis. Looking at Fig. 14, we see that two of the nine BFGP members, 84 Klio and (especially) 554 Peraga, have albedos much higher than those of the other seven, giving this distribution a marked positive skew.

To check whether or not the population variances can be considered equal, we use Levene's test (Snedecor and Cochran 1980, pp. 253-254), which is less sensitive to outliers than the analysis of variance (ANOVA) F test (since it relies on absolute values of deviations from the class mean rather than on squared deviations). We obtain a 7.7% probability that the null hypothesis of equal variances is valid; this is sufficiently large that we need not reject the hypothesis. Thus we can consider the possibility that the four distributions are identical except for location shifts. This is accomplished via a Kruskal-Wallis test, a nonparametric analog to one-way ANOVA which operates on ranks rather than on the estimated radar albedos themselves (Daniel 1990, pp. 226-231; Zar 1996, pp. 197-202). The null hypothesis that the four population medians are identical has only a 0.0013 probability of being valid, so

we can be confident that at least one of the six possible sample pairs shows a significant difference. The Kruskal-Wallis test itself does not reveal which one(s) of the six this is, so we apply a *post hoc* (multiple comparisons) test. The Dunn *post hoc* test (Zar 1996, p. 227) shows that the BFGP and M classes are likely to have different median radar albedos (Table XIV).

A data transformation can bring the four sample variances closer together while also reducing the skew of the BFGP distribution. We find that the transformation $s = \ln(\hat{\sigma}_{OC} + 0.05)$ meets these requirements. The Shapiro-Wilk test now tells us that it is fairly safe to assume normality for all four classes, and Levene's test yields a high probability that the four population variances are equal. Hence we can use one-way unblocked ANOVA (Zar 1996, pp. 180-191) on the transformed data. (This is a slightly more powerful test than Kruskal-Wallis if the distributions are indeed normal.) The null hypothesis that the four distributions are identical is highly improbable, leading us to favor the alternative hypothesis that at least two of the four distributions have different means.

A decision about which samples differ from which others depends on which *post hoc* test we use. Both the liberal Newman-Keuls test and the moderately conservative Tukey "honestly significant difference" test (Zar 1996, pp. 212-218) imply (at the 95% significance level) that the BFGP class differs from the S and C classes, and that all three differ from the M class. Yet the highly conservative Scheffé test (Zar 1996, pp. 222-225) indicates only that the M class differs from the other three. Evidently, reliable determination of whether or not C-class MBAs have higher radar albedos than other primitive asteroids hinges on our obtaining larger samples.

Table XIV also lists similar results for various combinations of OC and SC albedo. We carry out a Kruskal-Wallis test whenever Levene's test indicates greater than 5% probability of equal variances. For ANOVA, we also require a data transformation that yields four approximately normal distributions with similar variances, thus enabling us to use ANOVA. Blank table entries represent violations of one or more of these conditions.

Results for "total circular" albedo $\hat{\sigma}_{TC}$ are similar to those just described for $\hat{\sigma}_{OC}$, as expected for a sample of low- μ_C MBAs. We also compute the difference $\hat{\sigma}_{OC} - \hat{\sigma}_{SC}$; this is proportional to the echo power due to single-scattering from smooth surface elements under the assumption that all other scattering processes contribute a randomly polarized signal. While the M-class objects still differ from BFGP and from S, no other reliable differences are present for this variable. Single scattering from wavelength-scale structure can produce a variety of SC/OC ratios, and therefore we have also considered the variables $\hat{\sigma}_{OC} - 2\hat{\sigma}_{SC}$ and $\hat{\sigma}_{OC} - 3\hat{\sigma}_{SC}$. Most of the corresponding entries in Table XIV are blank, however, because the variance of the M sample is much larger than that of the other three. The object most responsible for this problem is 216 Kleopatra, which has the largest OC albedo (0.44) of any MBA, but which has $\hat{\sigma}_{SC} = 0$. Hence we cannot use Kruskal-Wallis or ANOVA to look for inter-class differences here -- although, of course, this large variance is itself a significant difference between M-class and other asteroids.

Taking the Kruskal-Wallis and ANOVA results together, we conclude that there is good reason to believe that M asteroids tend to have higher radar albedos and a wider range of albedos than do the other three classes; there is no evidence that C and S MBAs have different albedo distributions; and there is some suggestion, worthy of future study, that BFGP asteroids are radar-darker than are C and S objects.

We can apply a similar analysis to the polarization ratios (Table XIV). The presence of a zero value for 78 Diana gives the C distribution a strong negative skew, and the Shapiro-Wilk test indeed indicates that this distribution is non-normal. Levene's test allows us to assume equal variances, so we can apply a Kruskal-Wallis test; the result is that no credible differences between medians are present. In particular, the Kruskal-Wallis test fails to confirm the visual impression that BFGP objects have especially low μ_C values (Section 5.2). We cannot transform the data so as to reduce the skew -- say, by

squaring the μ_c values -- because that would increase the disparities between the sample variances. As a result we cannot apply one-way ANOVA to these data. We conclude that there currently is no convincing evidence that different taxonomic classes have different polarization ratio distributions.

Throughout these analyses we have not made use of the estimated errors on μ_c and $\hat{\sigma}_{oc}$ listed in Table V. In principle we could perform numerous simulations using "bootstrap" resampling (e.g., Efron and Tibshirani 1993). Each simulation would start with the creation of a 37-member numerical sample; the radar albedos and polarization ratios would be randomly drawn (with replacement) from normal distributions whose means and standard deviations are set equal to the estimates and one-sigma errors listed in Table V. We then would subject each such sample to the same analysis described above, and would thereby estimate the probability that the inter-class differences in $\hat{\sigma}_{oc}$ could result from measurement uncertainty. Yet we choose not to carry out such a procedure, since we feel that the main limitation on the validity of our conclusions is small sample size rather than measurement error. The need for more data on M-class and BFGP asteroids is particularly acute.

6. DISCUSSION

For an asteroid with $SC/OC = 0$, the echo would be due almost entirely to single backscattering from surface elements that are large and smooth at scales near the wavelength. In this case we can write $\hat{\sigma}_{OC} = gR$, where R is the power reflection coefficient at normal incidence (or simply the reflectivity) and g is the backscatter gain, which would be unity for a smooth sphere, that is, an isotropic scatterer. For a sphere with surface facets having rms slope s_0 , g would be of order $1 + s_0^2/2$, which for realistic slope distributions does not exceed unity by more than a few tens of percent; see, for example, the results of Mitchell *et al.* (1996) for Ceres and Pallas. For our generally nonspherical targets, we expect that the rotation-phase averaging of the echoes leads to values of g that are comparable to or slightly larger than unity.

For targets with nonzero μ_C , some of the echo power is due to single scattering from rough surfaces or irregularly shaped particles, or to multiple scattering. Let us use the term "diffuse" to refer collectively to all echo not due to specular reflection from smooth surface elements. If the diffuse echo is characterized by OC albedo $\hat{\sigma}_{OC, diff}$ and by polarization ratio $\mu_{C, diff}$, then we can write

$$\hat{\sigma}_{OC, diff} = \frac{\hat{\sigma}_{SC}}{\mu_{C, diff}} = \frac{\mu_C \hat{\sigma}_{OC}}{\mu_{C, diff}} \quad (12)$$

so the part of the OC albedo due to specular reflection from smooth surface elements is

$$\hat{\sigma}_{OC, spec} = \hat{\sigma}_{OC} - \hat{\sigma}_{OC, diff} = \hat{\sigma}_{OC} \left(1 - \frac{\mu_C}{\mu_{C, diff}} \right) \quad (13)$$

Analyses based on disc-resolved echoes from the Moon and inner planets (Harmon and Ostro 1985 and references therein) and on empirical and theoretical information about the polarization ratios for diffuse scattering processes (*e.g.*, Cuzzi and Pollack 1978 and references therein) suggest that a reasonable guess for $\mu_{C, diff}$ is in the realm of 0.5. For purposes of discussion, we list corresponding values for $\hat{\sigma}_{OC, spec}$ in the second column of Table XV. In the same spirit, let us take g to be 1.2; this is the gain of a sphere with an r.m.s. slope of about 32 degrees. For relevant rocks and minerals, it is reasonable to treat R as a function of bulk density d_{bulk} , and we will use the empirical relationship presented by Garvin *et al.* (1985):

$$d_{bulk}(R) = 3.2 \ln \left(\frac{1 + \sqrt{R}}{1 - \sqrt{R}} \right) \quad (14)$$

The table lists bulk densities corresponding to $R = \hat{\sigma}_{OC, spec} / 1.2$, as well as solid rock densities d_{solid} corresponding to a porosity, $p = 0.5$, which is a typical value for the upper 30 cm of the lunar regolith (Heiken *et al.* 1991, Table 9.5).

Thus Table XV uses reasonable guesses for $\mu_{C, diff}$, g , and porosity to translate disc-integrated radar properties into solid-rock densities. The uncertainties in these guesses propagate into a systematic uncertainty of about 50% in the numbers listed for d_{solid} . For comparison, typical meteorite values of d_{solid} (Ostro *et al.* 1991b and references therein) are 7.6 g cm⁻³ for irons, 4.9 g cm⁻³ for stony irons, 3.5 g cm⁻³ for ordinary and enstatite chondrites, and 2.7 g cm⁻³ for carbonaceous chondrites (which range from 2.2

g cm^{-3} for CI to 3.4 g cm^{-3} for CO/CV). Given the canonical plausible associations of asteroid classes with meteorite types (Bell *et al.* 1989 and references therein; Gaffey *et al.* 1989), the entries for d_{solid} in Table XV seem reasonable for the S and M classes but high for the C and BFGP classes. Perhaps many members of the last two classes have low-porosity regoliths.

Estimates of the bulk densities of the G asteroid Ceres and the B asteroid Pallas ($2.1 \pm 0.1 \text{ g cm}^{-3}$ and $2.6 \pm 0.5 \text{ g cm}^{-3}$; see discussion by Mitchell *et al.* 1996 and references therein) are larger than that for the C asteroid Mathilde ($1.3 \pm 0.2 \text{ g cm}^{-3}$; Yeomans *et al.* 1997), which is comparable to that estimated for C asteroids from their effects on the orbit of Mars (E. M. Standish, pers. comm.; see Yeomans *et al.* 1997). Our C and BFGP values of d_{bulk} are in the middle of this suite of non-radar density estimates. The most reliable S-class estimate of d_{bulk} , $2.6 \pm 0.5 \text{ g cm}^{-3}$ for Ida (Belton *et al.* 1995), is on the high side of the "error" interval in Table XV.

Now let us comment on possible implications of the statistical results from the previous section:

1. The polarization ratio distributions of the C, S, BFGP, and M classes are broad.

There are significant target-to-target variations in near-surface roughness, irrespective of class. (Note, however, that the distribution of near-Earth asteroid polarization ratios is about three times broader than the MBA distribution.)

2. The radar albedo distributions of the C, S, BFGP, and M classes are broad.

The OC albedos of the Moon, Mercury, Venus, and Mars span the narrow range 0.06 to 0.11 (Ostro 1993, Table 2); even the C and S-class $\hat{\sigma}_{\text{OC}}$ distributions are broad by comparison. Near-surface bulk density -- and hence solid-rock density, metal fraction, and/or porosity -- varies dramatically among main-belt asteroids, and even among MBAs of a given taxonomic class.

3. There is no reliable evidence that the C, S, BFGP, and M classes have different polarization-ratio distributions.

Despite the likely compositional distinctions between classes, the degree of centimeter-to-decimeter-scale roughness does not depend on class.

4. There is good reason to believe that M asteroids tend to have higher albedos and a wider range of albedos than the C, S, and BFGP classes.

The radar-brightest M asteroids are likely to be iron-meteorite analogues. The radar-darkest members of this class have lower metal concentrations and might be enstatite chondrite analogues.

5. For the M class, radar albedo is anticorrelated with visual albedo.

Visual albedo may offer a criterion for splitting the M class into relatively metal-rich and metal-poor subclasses.

6. There is no reason to believe that the C and S classes have different radar albedo distributions.

If the *only* difference between S and C asteroids were their solid-rock density d_{solid} , then, if forced to choose between stony irons and ordinary chondrites as the S-class meteorite analogue, we would have to favor ordinary chondrites, because their solid-rock densities are less removed from those of carbonaceous chondrites. On the other hand, high-porosity stony-iron analogues and low-porosity ordinary-chondrite analogues could have identical bulk densities and therefore identical radar reflectivities.

7. *There is an indication that BFGP asteroids are radar-darker than our other sampled classes.* These objects are likely candidates for being mineralogically similar to the lowest- d_{solid} meteorites (CI and CM chondrites).

7. CONCLUSION

In terms of the size of the MBA radar sample, radar observations are where UBV photometry stood three decades ago (Chapman and Zellner 1978). However, the upgrading of the Arecibo Observatory has doubled that telescope's range, extending it roughly from the main belt's inner edge to its outer edge. Hundreds of MBAs are now detectable at single-date SNRs much larger than those achieved in the observations reported here (Table XVI).

Obviously it is desirable to perform a thorough survey of MBA radar properties. Since SNR increases as the square root of the integration time, there are many objects for which a week or two of daily observations could yield dataset SNRs of at least several hundred. This is strong enough for delay-Doppler imaging to permit the construction of accurate models of target shape and backscatter gain (Hudson 1993), and hence of radar reflectivity and surface bulk density.

ACKNOWLEDGMENTS

We thank the Goldstone and Arecibo technical staffs for their assistance. CM greatly benefitted from a NASA-ASEE 1997 Summer Faculty Fellowship in Aeronautics and Space Research. He also thanks Lance Benner for technical aid and helpful discussions during his stay at JPL, and Al Harris for information on several lightcurves. The Arecibo Observatory is part of the National Astronomy and Ionosphere Center, which is operated by Cornell University under a cooperative agreement with the National Science Foundation and with support from NASA. Part of this research was conducted at the Jet Propulsion Laboratory, California Institute of Technology, under contract with the National Aeronautics and Space Administration (NASA).

REFERENCES

- BBN Technologies 1997. *Prophet 5.0* statistical software. Available at <http://www-prophet.bbn.com/>.
- Bell, J. F., D. R. Davis, W. K. Hartmann, and M. J. Gaffey 1989. Asteroids: The big picture. In *Asteroids II* (R. P. Binzel, T. Gehrels, and M. S. Matthews, Eds.), pp. 921-945. Univ. of Arizona Press, Tucson.
- Belskaya, I. N., and C.-I. Lagerkvist 1996. Physical properties of M class asteroids. *Planet. Space Sci.* **44**, 783-794.
- Belton, M. J. S., and 16 colleagues 1995. Bulk density of asteroid 243 Ida from the orbit of its satellite Dactyl. *Nature* **374**, 785-788.
- Birlan, M., M. Fulchignoni, and M. A. Barucci 1996. Effects of IRAS albedo correction on the G-mode asteroid taxonomy. *Icarus* **124**, 352-354.
- Bowell, E., T. Gehrels, and B. Zellner 1979. Magnitudes, colors, types and adopted diameters of the asteroids. In *Asteroids* (T. Gehrels, Ed.), pp. 1108-1129. Univ. of Arizona Press, Tucson.
- Brown, R. H. 1985. Ellipsoidal geometry in asteroid thermal models: The standard radiometric model. *Icarus* **64**, 53-63.
- Chapman, C. R., and B. Zellner 1978. The role of Earth-based observations of asteroids during the next decade. In *Asteroids: An Exploration Assessment* (D. Morrison and W. C. Wells, Eds.), pp. 183-191. NASA Conf. Pub. 2053.
- Conover, W. J. 1980. *Practical Nonparametric Statistics*, 2nd ed., John Wiley & Sons, New York.
- Cuzzi, J. N., and J. B. Pollack 1978. Saturn's rings: particle composition and size distribution as constrained by microwave observations. I. Radar observations. *Icarus* **33**, 233-262.
- Daniel, W. W. 1990. *Applied Nonparametric Statistics*, 2nd ed., PWS-Kent, Boston.
- de Pater, I., P. Palmer, D. L. Mitchell, S. J. Ostro, D. K. Yeomans, and L. E. Snyder 1994. Radar aperture synthesis observations of asteroids. *Icarus* **111**, 489-502.
- De Angelis, G. 1995. Asteroid spin, pole and shape determinations. *Planet. Space Sci.* **43**, 649-682.
- Dollfus, A., M. Wolff, J. E. Geake, D. F. Lupishko, and L. M. Dougherty 1989. Photopolarimetry of asteroids. In *Asteroids II* (R. P. Binzel, T. Gehrels, and M. S. Matthews, Eds.), pp. 594-616. Univ. of Arizona Press, Tucson.
- Dotto, E., M. A. Barucci, M. Fulchignoni, M. Di Martino, A. Rotundi, R. Burchi, and A. Di Paolantonio 1992. M-type asteroids: Rotational properties of 16 objects. *Astron. Astrophys. Suppl. Ser.* **95**, 195-211.

Dunham, D. W. 1996. 1993 October 9 occultation of 8.3-mag. SAO 128735 by (27) Euterpe. Available at <http://www.anomalies.com/iota/more/euterpe.htm>.

Efron, B. and R. J. Tibshirani 1993. *An Introduction to the Bootstrap*, Chapman and Hall, New York.

Gaffey, M. J., J. F. Bell, and D. P. Cruikshank 1989. Reflectance spectroscopy and asteroid surface mineralogy. In *Asteroids II* (R. P. Binzel, T. Gehrels, and M. S. Matthews, Eds.), pp. 98-127. Univ. of Arizona Press, Tucson.

Harmon, J. K., and S. J. Ostro 1985. Mars: Dual-polarization radar observations with extended coverage. *Icarus* **62**, 110-128.

Harris, A. W., and J. W. Young 1989. Asteroid lightcurve observations from 1979-1981. *Icarus* **81**, 314-364.

Heiken, G. H., D. T. Vaniman, and B. M. French 1991. *Lunar Sourcebook*. Cambridge Univ. Press, New York.

Hoffmann, M., and E. H. Geyer 1990. A photometric study of 18 Melpomene. In *Asteroids, Comets, Meteors III* (C.-I. Lagerkvist, H. Rickman, B. A. Lindblad, and M. Lindgren, Eds.), pp. 111-114. Uppsala University.

Howell, E. S., E. Merényi, and L. A. Lebofsky 1994. Classification of asteroid spectra using a neural network. *J. Geophys. Res.* **99**, 10,847-10,865.

Hudson, R. S. 1993. Three-dimensional reconstruction of asteroids from radar observations. *Remote Sensing Reviews* **8**, 195-203.

Jurgens, R. F. 1982. Radar backscattering from a rough rotating triaxial ellipsoid with applications to the geodesy of small asteroids. *Icarus* **49**, 97-108.

Lagerkvist, C.-I., A. W. Harris, and V. Zappalà 1989. Asteroid lightcurve parameters. In *Asteroids II* (R. P. Binzel, T. Gehrels, and M. S. Matthews, Eds.), pp. 1162-1179. Univ. of Arizona Press, Tucson.

Lagerkvist, C.-I., A. Erikson, H. Debehogne, L. Festin, P. Magnusson, S. Mottola, T. Oja, G. De Angelis, I. N. Belskaya, M. Dahlgren, M. Gonano-Beurer, J. Lagerros, K. Lumme, and S. Pohjolainen 1995. Physical studies of asteroids. XXIX. Photometry and analysis of 27 asteroids. *Astron. Astrophys. Suppl. Ser.* **113**, 115-129.

Lagerkvist, C.-I., P. Magnusson, I. Belskaya, J. Piironen, J. Warell, and M. Dahlgren 1996. *Asteroid Photometric Catalogue*, Fourth Update, Uppsala Astron. Obs. Also available at <ftp://ftp.astro.uu.se/pub/Asteroids/Photometry/>.

Lebofsky, L. A., and J. R. Spencer 1989. Radiometry and thermal modeling of asteroids. In *Asteroids II* (R. P. Binzel, T. Gehrels, and M. S. Matthews, Eds.), pp. 128-147. Univ. of Arizona Press, Tucson.

Lupishko, D. F., and F. P. Velichko 1987. Sense of rotation for asteroids 21, 63, 216, and 349. *Kinem. Phys. Celest. Bodies* **3**, 57-65.

Lupishko, D. F., F. P. Velichko, I. N. Belskaya, and V. G. Shevchenko 1987. Pole coordinates and phase dependence of the light of the asteroid 21 Lutetia. *Kinem. Phys. Celest. Bodies* **3**, 36-38.

Magnusson, P. 1995. Asteroid spin vector determinations. Available at <ftp://ftp.astro.uu.se/pub/Asteroids/SpinVectors/>.

Michałowski, T. 1992. Spin vectors of asteroids 21 Lutetia, 196 Philomela, 250 Bettina, 337 Devosa and 804 Hispania. In *Asteroids, Comets, Meteors 1991* (A. W. Harris and E. Bowell, Eds.), pp. 417-419. Lunar and Planetary Institute, Houston.

Michałowski, T. 1993. Poles, shapes, senses of rotation, and sidereal periods of asteroids. *Icarus* **106**, 563-572.

Michałowski, T. 1996. Pole and shape determination for 12 asteroids. *Icarus* **123**, 456-462.

Michałowski, T., F. P. Velichko, M. Di Martino, Yu. N. Krugly, V. G. Kalashnikov, V. G. Shevchenko, P. V. Birch, W. D. Sears, P. Denchev, and T. Kwiatkowski 1995. Models of four asteroids: 17 Thetis, 52 Europa, 532 Herculina, and 704 Interamnia. *Icarus* **118**, 292-301.

Millis, R. L., L. H. Wasserman, O. G. Franz, E. Bowell, R. A. Nye, D. T. Thompson, N. M. White, W. B. Hubbard, R. E. Eplee, Jr., L. A. Lebofsky, R. L. Marcialis, R. J. Greenberg, D. M. Hunten, H. J. Reitsema, Q. Bochen, D. W. Dunham, P. D. Maley, A. R. Klemola, and D. K. Yeomans 1989. Observations of the 8 December 1987 occultation of AG +40°0783 by 324 Bamberga. *Astron. J.* **98**, 1094-1099.

Mitchell, D. L., S. J. Ostro, K. D. Rosema, R. S. Hudson, D. B. Campbell, J. F. Chandler, and I. I. Shapiro 1995. Radar observations of asteroids 7 Iris, 9 Metis, 12 Victoria, 216 Kleopatra, and 654 Zelinda. *Icarus* **118**, 105-131.

Mitchell, D. L., S. J. Ostro, R. S. Hudson, K. D. Rosema, D. B. Campbell, R. Vélez, J. F. Chandler, I. I. Shapiro, J. D. Giorgini, and D. K. Yeomans 1996. Radar observations of asteroids 1 Ceres, 2 Pallas, and 4 Vesta. *Icarus* **124**, 113-133.

Morrison, D. 1974. Radiometric diameters and albedos of 40 asteroids. *Astrophys. J.* **194**, 203-212.

Ostro, S. J. 1987. Physical properties of asteroids from radar observations. In *Evolution of the Small Bodies of the Solar System* (M. Fulchignoni and L. Kresák, Eds.), pp. 131-146. Elsevier Science, Amsterdam.

Ostro, S. J. 1993. Planetary radar astronomy. *Rev. Mod. Phys.* **65**, 1235-1279.

Ostro, S. J., D. B. Campbell, and I. I. Shapiro 1983. Radar observations of asteroid 1685 Toro. *Astron. J.* **88**, 565-576.

- Ostro, S. J., D. B. Campbell, and I. I. Shapiro 1985. Mainbelt asteroids: Dual-polarization radar observations. *Science* **229**, 442-446.
- Ostro, S. J., D. B. Campbell, J. F. Chandler, I. I. Shapiro, A. A. Hine, R. Vélez, R. F. Jurgens, K. D. Rosema, R. Winkler, and D. K. Yeomans 1991a. Asteroid radar astrometry. *Astron. J.* **102**, 1490-1502.
- Ostro, S. J., D. B. Campbell, J. F. Chandler, A. A. Hine, R. S. Hudson, K. D. Rosema, and I. I. Shapiro 1991b. Asteroid 1986 DA: Radar evidence for a metallic composition. *Science* **252**, 1399-1404.
- Ostro, S. J., D. B. Campbell, R. A. Simpson, R. S. Hudson, J. F. Chandler, K. D. Rosema, I. I. Shapiro, E. M. Standish, R. Winkler, D. K. Yeomans, R. Vélez, and R. M. Goldstein 1992. Europa, Ganymede, and Callisto: New radar results from Arecibo and Goldstone. *J. Geophys. Res.* **97**, 18227-18244.
- Rivkin, A. S., E. S. Howell, D. T. Britt, L. A. Lebofsky, M. C. Nolan, and D. D. Branston 1995. Three-micron spectrometric survey of M- and E-class asteroids. *Icarus* **117**, 90-100.
- Rivkin, A. S., L. A. Lebofsky, D. T. Britt, and E. S. Howell 1997. Three-micron survey of E- and M-class asteroids: Final results. *Bull. Amer. Astron. Soc.* **29**, 972-973. [Abstract]
- Scaltriti, F., V. Zappalà, and H. J. Schober 1979. The rotations of 128 Nemesis and 393 Lampetia: The longest known periods to date. *Icarus* **37**, 133-141.
- Schober, H. J., A. Erikson, G. Hahn, C.-I. Lagerkvist, R. Albrecht, W. Ormig, A. Schroll, and M. Stadler 1994. Physical studies of asteroids. XXVIII. Lightcurves and photoelectric photometry of asteroids 2, 14, 51, 105, 181, 238, 258, 369, 377, 416, 487, 626, 679, 1048 and 2183. *Astron. Astrophys. Suppl. Ser.* **105**, 281-300.
- Snedecor G. W., and W. G. Cochran 1980. *Statistical Methods*. 7th ed, The Iowa Univ. Press, Ames, Iowa.
- Taylor, R. C., T. Gehrels, and R. C. Capen 1976. Minor planets and related objects. XXI. Photometry of eight asteroids. *Astron. J.* **81**, 778-786.
- Tedesco, E. F. 1997. *The IRAS Minor Planet Survey, Version 3.0*. Available at the Planetary Data System Small Bodies Node, http://pdssbn.astro.umd.edu/sbnhtml/asteroids/physical_param.html.
- Tholen, D. J. 1989. Asteroid taxonomic classifications. In *Asteroids II* (R. P. Binzel, T. Gehrels, and M. S. Matthews, Eds.), pp. 1139-1150. Univ. of Arizona Press, Tucson.
- Tiuri, M. E. 1964. Radio astronomy receivers. *IEEE Trans. Antennas Propag.* **AP-12**, 930-938.
- Weidenschilling, S. J., C. R. Chapman, D. R. Davis, R. Greenberg, D. H. Levy, R. P. Binzel, S. M. Vail, M. Magee, and D. Spaute 1990. Photometric geodesy of main-belt asteroids. III. Additional lightcurves. *Icarus* **86**, 402-447.
- Yeomans, D. K., and 12 colleagues 1997. Estimating the mass of asteroid 253 Mathilde from tracking data during the NEAR flyby. *Science* **278**, 2106-2109.

Zappalà, V., M. Di Martino, P. Farinella, and P. Paolicchi 1984. An analytical method for the determination of the rotational direction of asteroids. In *Asteroids, Comets, Meteors* (C.-I. Lagerkvist and H. Rickman, Eds.), pp. 73-76. Uppsala University.

Zar, J. H. 1996. *Biostatistical Analysis*, 3rd ed., Prentice-Hall, Upper Saddle River, NJ.

Zeigler, K. W., and R. C. Wampole 1988. Photoelectric photometry of asteroids 84 Klio and 678 Fredeguendis. *Minor Planet Bull.* **15**, 15-16.

FIGURE CAPTIONS

FIG. 1. Weighted sums of OC (solid lines) and SC (dashed lines) echo spectra for all radar experiments. Echo power, in units of standard deviations of the noise, is plotted versus Doppler frequency (Hz) relative to that of hypothetical echoes from the target's center of mass. The vertical bar at the origin indicates ± 1 standard deviation of the OC noise. Each label gives the target name, the observation year (with Goldstone experiments denoted by G), and the frequency resolution of the displayed data. Rotation phase coverage is depicted in the upper right portion of each plot for which these data are available in computer-readable format. Each radial line segment denotes the phase (relative to an arbitrary epoch) of an independent spectrum formed by summing a several-minute data "group" (see Section 2); the length of the segment is proportional to the OC noise standard deviation of the corresponding spectrum.

FIG. 2. Weighted sums of 1995 OC echo spectra of Melpomene within three adjacent rotation phase intervals. The four rows display these sums for three different observing dates and for the combined dates. All twelve plots are on the scale indicated at lower left.

FIG. 3. Comparison of radar and lightcurve constraints on Melpomene's pole direction shown in a rectangular projection of ecliptic coordinates. The target's position during each radar experiment is shown by a plus symbol, and the pole constraints for each experiment taken separately are shown by a pair of circles, one centered on the target's position and one on the antipodal position. These circles are defined (Eq. 10) by the ratio of measured bandwidth B to predicted maximum-breadth bandwidth $B_{\max}(\delta_{\text{rad}}=0)$. Predicted bandwidths are 404 ± 52 Hz (1985) and 1450 ± 190 Hz (1995 G). Lower bounds on B are 270 Hz (1985) and 810 Hz (1995 G); these limits constrain the pole to lie outside each of the four circles. The two optical pole solutions of Hoffmann and Geyer (1990), and the quoted uncertainties, are plotted as open circles with error bars.

FIG. 4. Lutetia pole constraints; see Fig. 3 caption. Radar data constrain the pole to lie within the two annuli, which are defined (Eq. 10) by the ratio of measured bandwidth $B = 58 \pm 10$ Hz to predicted maximum-breadth bandwidth $B_{\max}(\delta_{\text{rad}}=0) = 442 \pm 75$ Hz. See text for further discussion. Optical pole solutions and quoted uncertainties (Table III) are plotted as open symbols with error bars: \circ = Lupishko and Velichko (1987), Lupishko *et al.* (1987); \triangle = Michałowski (1992); \times = Dotto *et al.* (1992); \triangleleft = Michałowski (1993); ∇ = De Angelis (1995); \square = Lagerkvist *et al.* (1995); \triangleright = Michałowski (1996).

FIG. 5. Weighted sums of dual-circular and dual-linear polarization echo spectra of Daphne. Solid lines denote OC and SL spectra, while dashed lines show SC and OL data. The vertical bar at the origin indicates ± 1 standard deviation of the OC or SL noise.

FIG. 6. Klotho pole constraints; see Fig. 3 caption. Predicted maximum-breadth bandwidths $B_{\max}(\delta_{\text{rad}}=0)$ are 77 ± 14 Hz (1981) and 277 ± 50 Hz (1993-4 G). Measured bandwidths are $B \geq 35$ Hz (1981) and $B = 310 \pm 20$ Hz (1993-4 G); these results constrain the pole to lie outside each of the four circles. No optical pole determinations have been published for this asteroid.

FIG. 7. Weighted sum of OC echo spectra of Artemis, folded about zero frequency. The vertical bar at the origin indicates ± 1 standard deviation of the noise.

FIG. 8. Weighted sum of echo spectra of Artemis for each of the two observing dates. The vertical bar at the origin indicates ± 1 standard deviation of the OC noise.

FIG. 9. Weighted sums of echo spectra of Lampetia for each of the five observing dates. All plots are on the scale indicated at lower left. The vertical bar at the origin indicates ± 1 standard deviation of the OC or SL noise. The central plot in the top half of the figure depicts rotation phase coverage for an assumed period of 38.7 hr; see Fig. 1 caption. Arrows connect each of the five single-date sums with the corresponding rotation phase interval. The bottom half of the figure is the same as the top, except that a 19.35-hr period is assumed.

FIG. 10. Weighted sums of dual-circular and dual-linear polarization echo spectra of Lampetia; see Fig. 5 caption.

FIG. 11. Weighted sums of dual-circular and dual-linear polarization echo spectra of Lampetia for 1986 July 16 and 20, respectively, for the rotation phase range 0° - 12° (assuming a 19.35-hr period). The vertical bar at the origin indicates ± 1 standard deviation of the OC or SL noise.

FIG. 12. OC albedo $\hat{\sigma}_{OC}$ and polarization ratio μ_C from Table V, plotted vs. radiometric diameter D_{IR} and visual albedo p_V . Plotting symbols indicate taxonomic class; see legend. Uncertainties in $\hat{\sigma}_{OC}$ estimates are several tens of percent.

FIG. 13. Polarization ratio μ_C plotted vs. OC albedo $\hat{\sigma}_{OC}$ (Table V). Plotting symbols indicate taxonomic class; see legend.

FIG. 14. Histograms of the OC albedo and polarization ratio distributions for the BFGP, C, S, and M-class samples. Each bin is 0.05 wide and includes the lower but not the upper endpoint. Each cell is labeled by the corresponding asteroid number.

FIG. 15. Histograms of the OC albedo and polarization ratio distributions for all MBA radar targets. Each bin is 0.05 wide and includes the lower but not the upper endpoint. Contributions of the various taxonomic classes are indicated.

Fig. 1

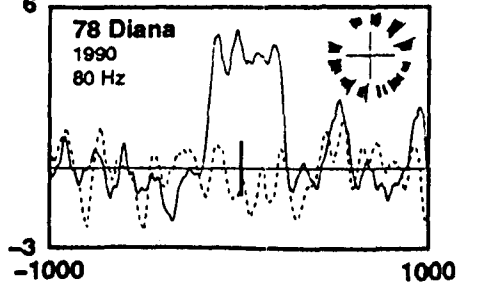
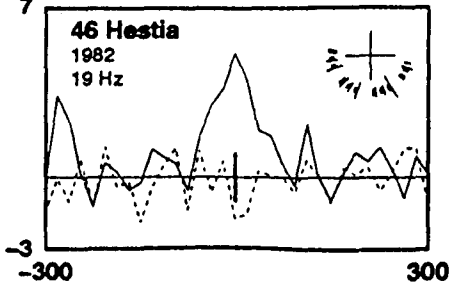
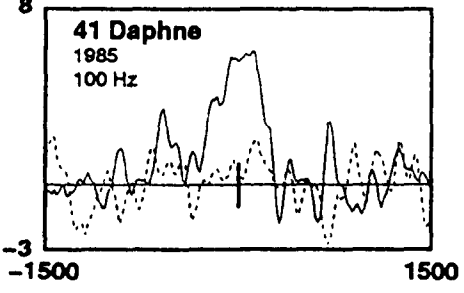
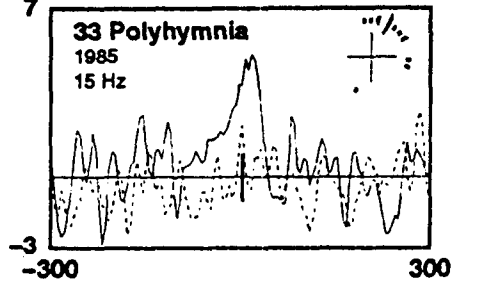
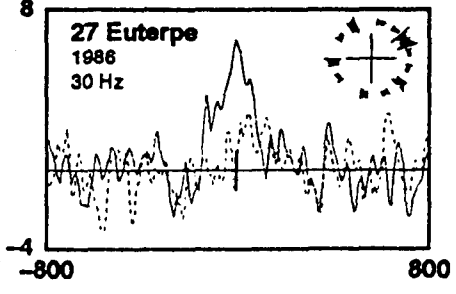
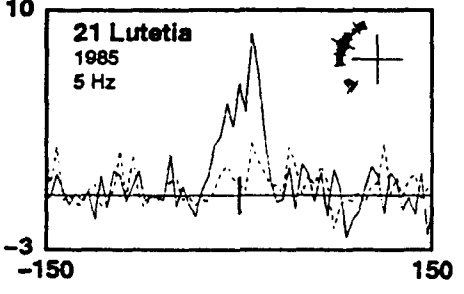
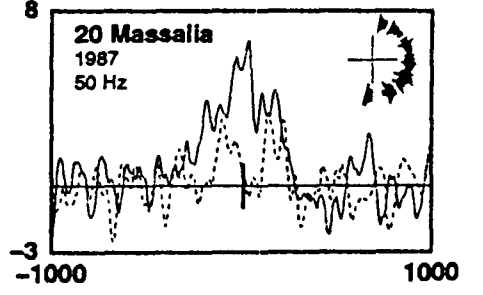
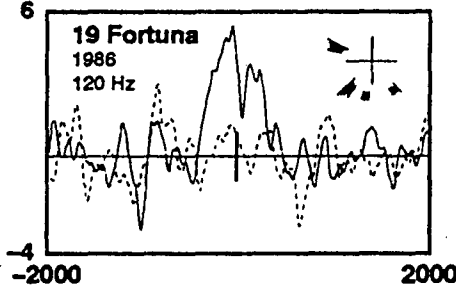
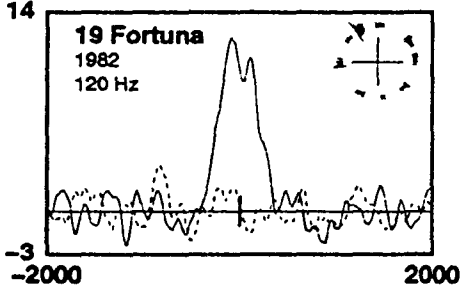
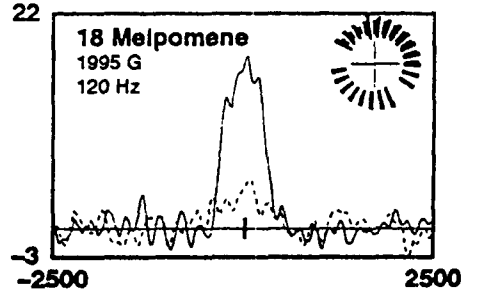
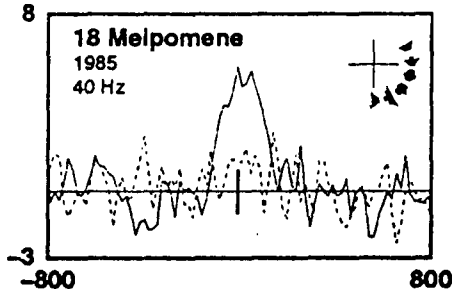
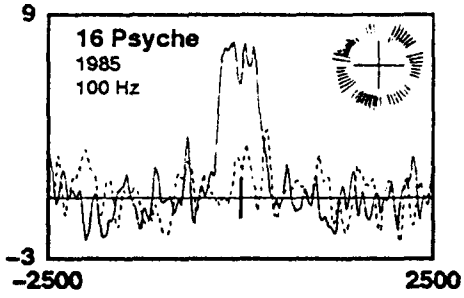
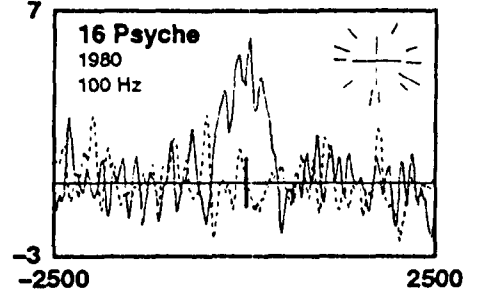
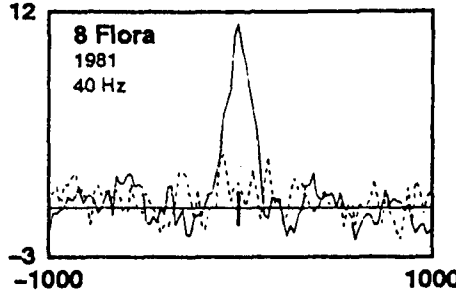
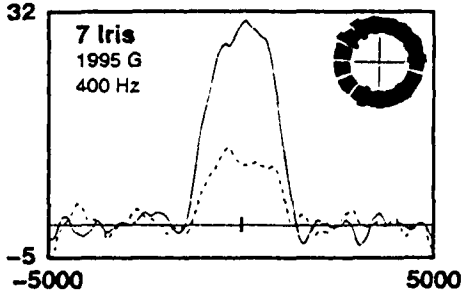
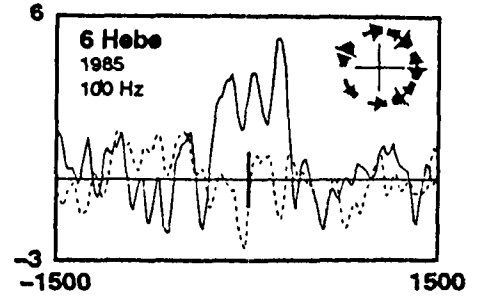
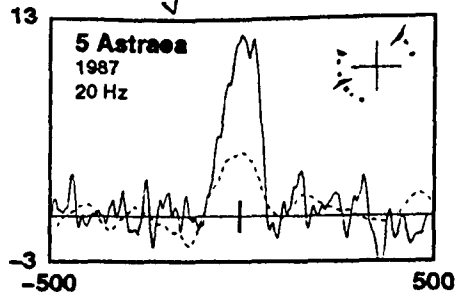
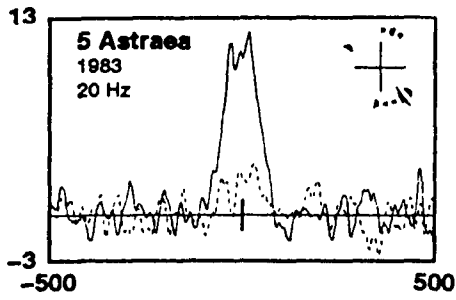


Fig. 1 (Cont'd)

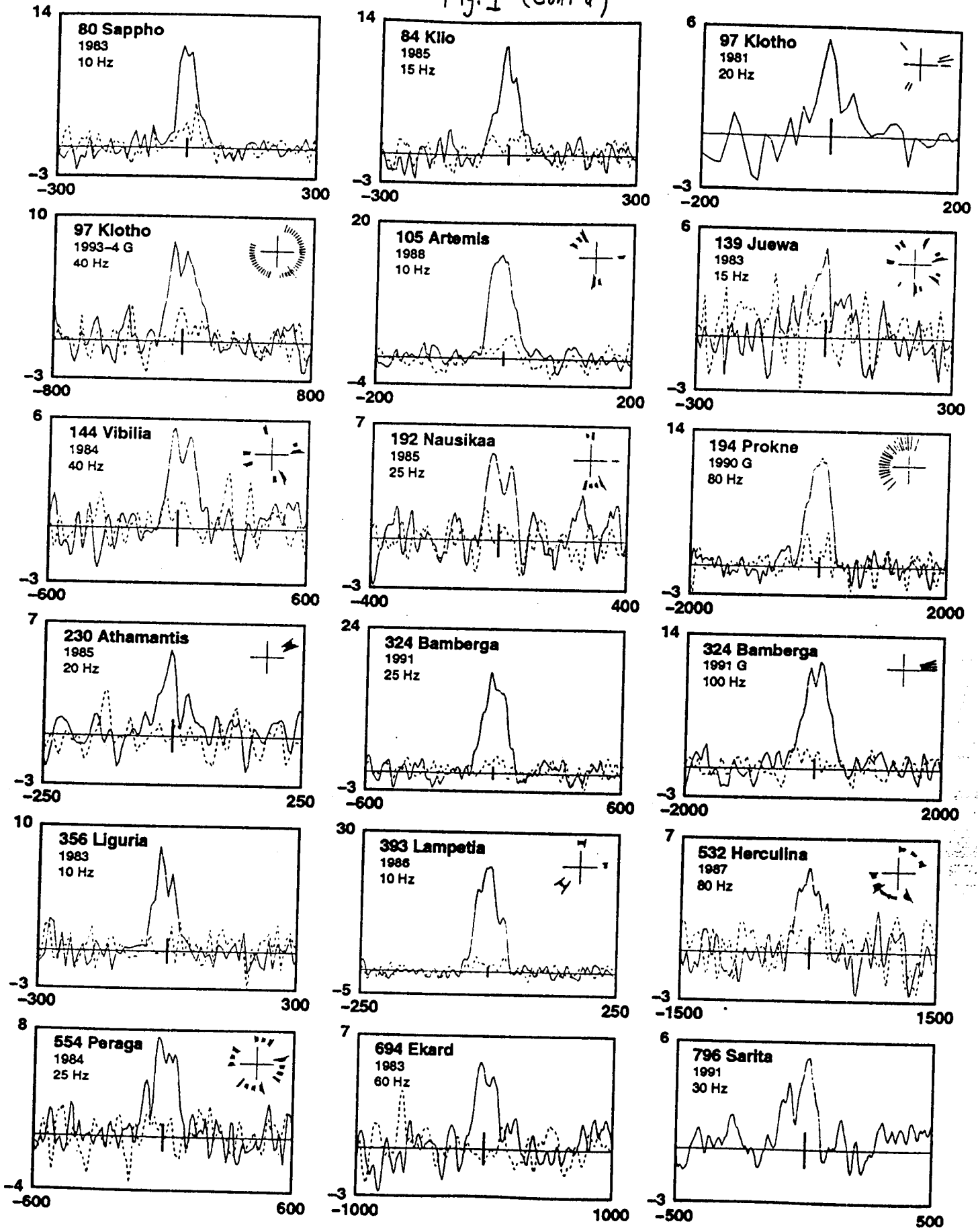


Fig. 2

18 Melpomene

1995 G

Resolution = 200 Hz

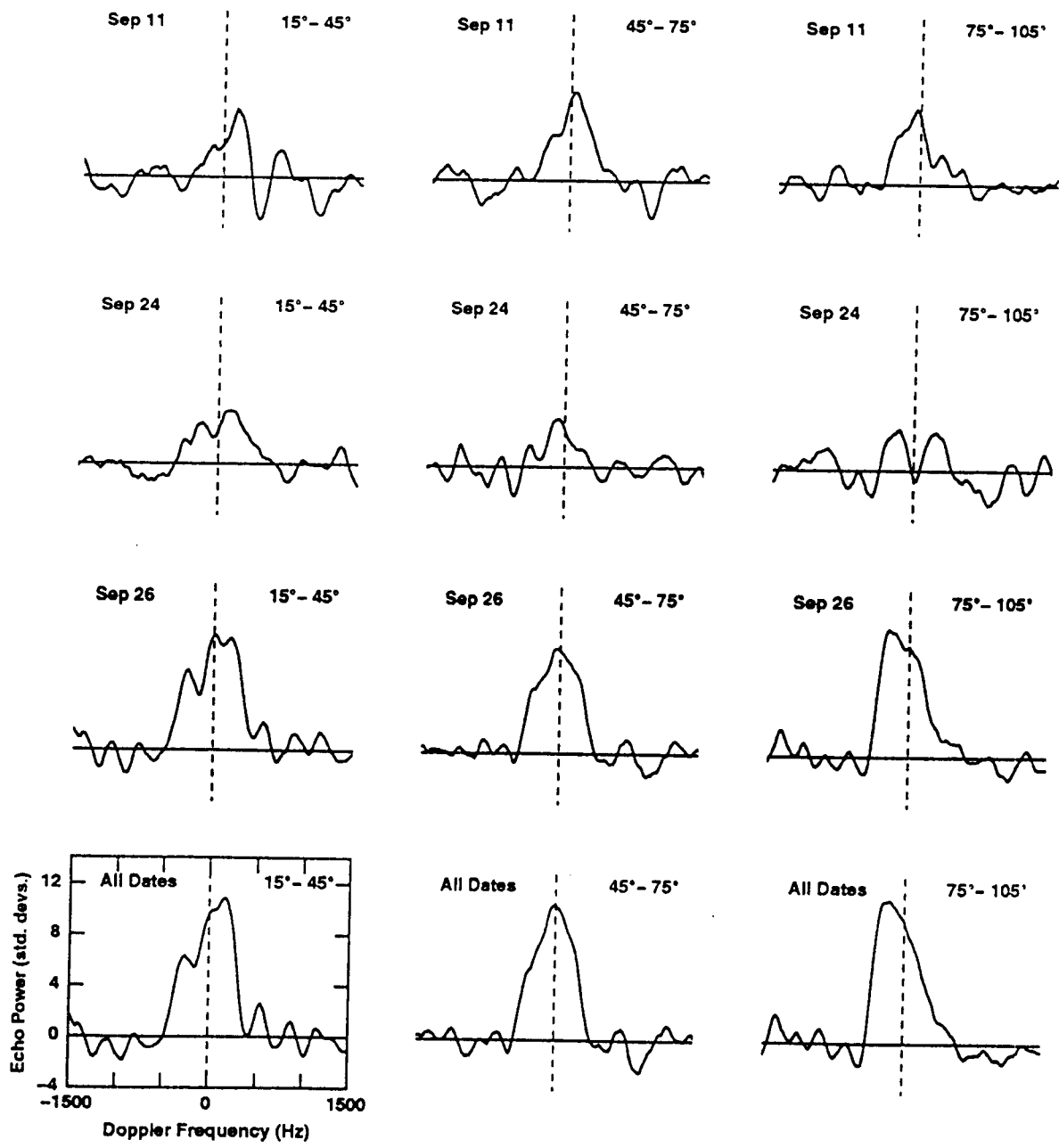


Fig. 3

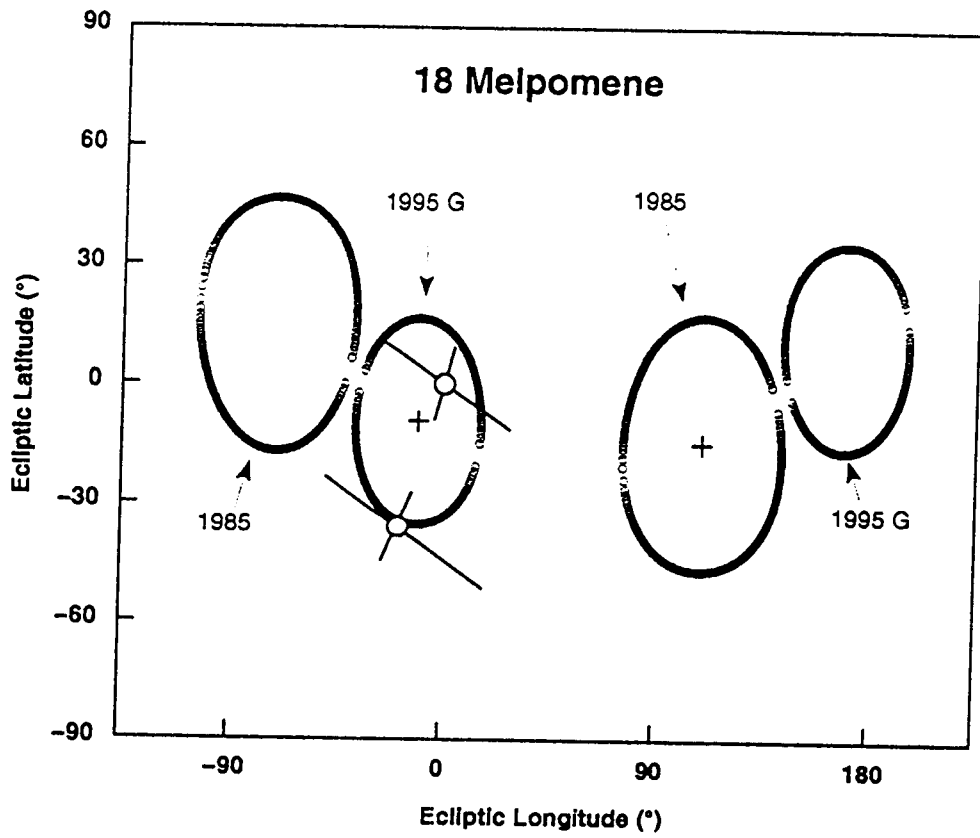


Fig. 4

21 Lutetia

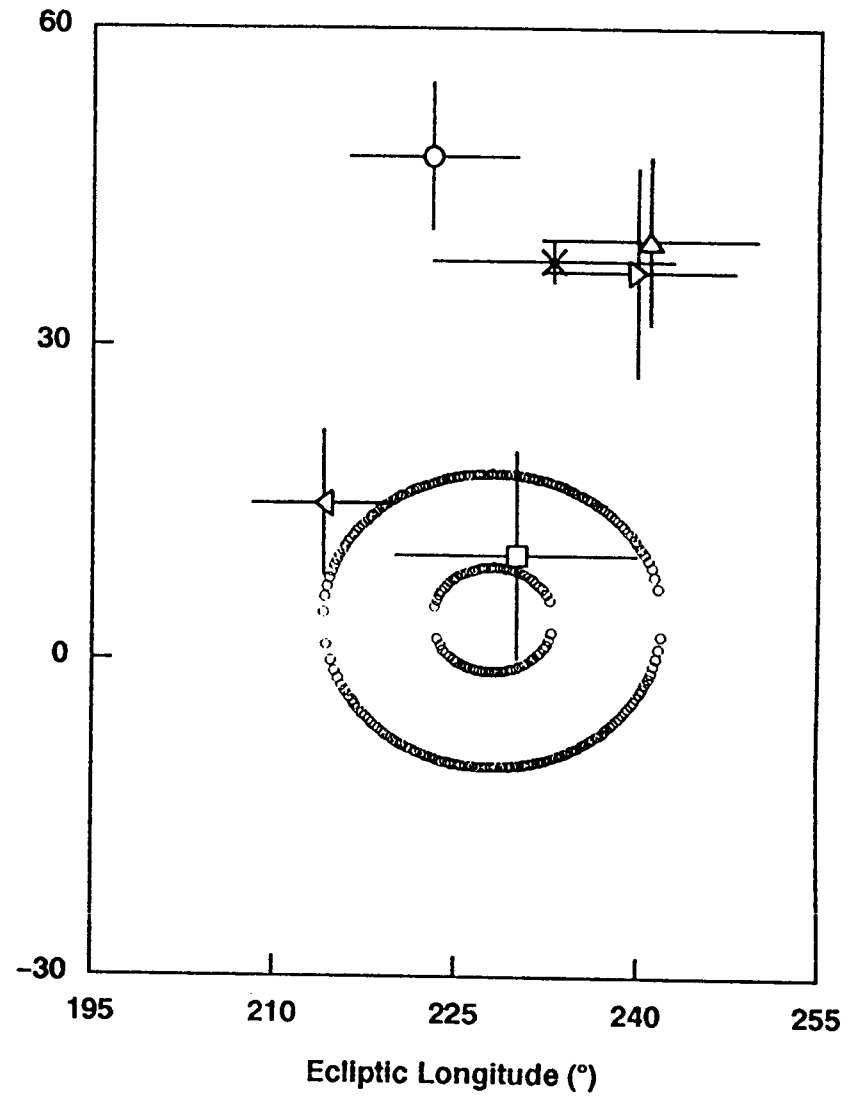
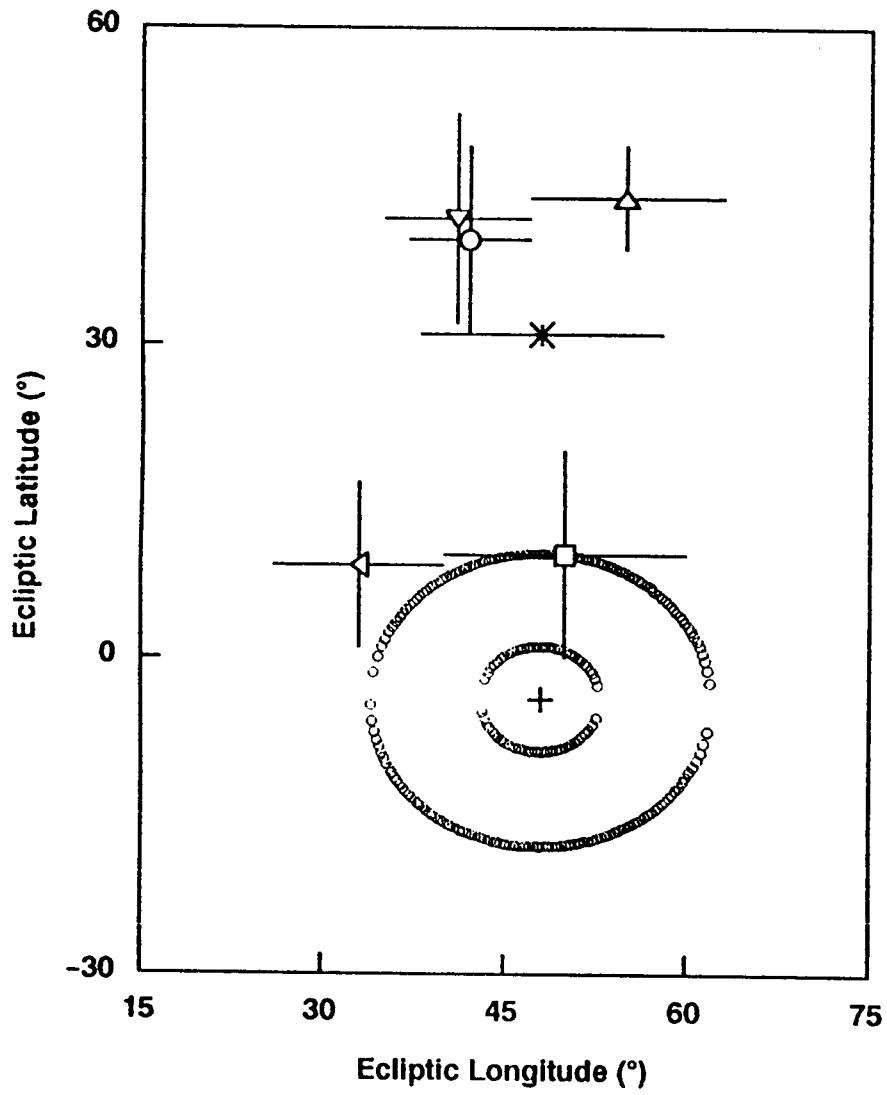


Fig. 5

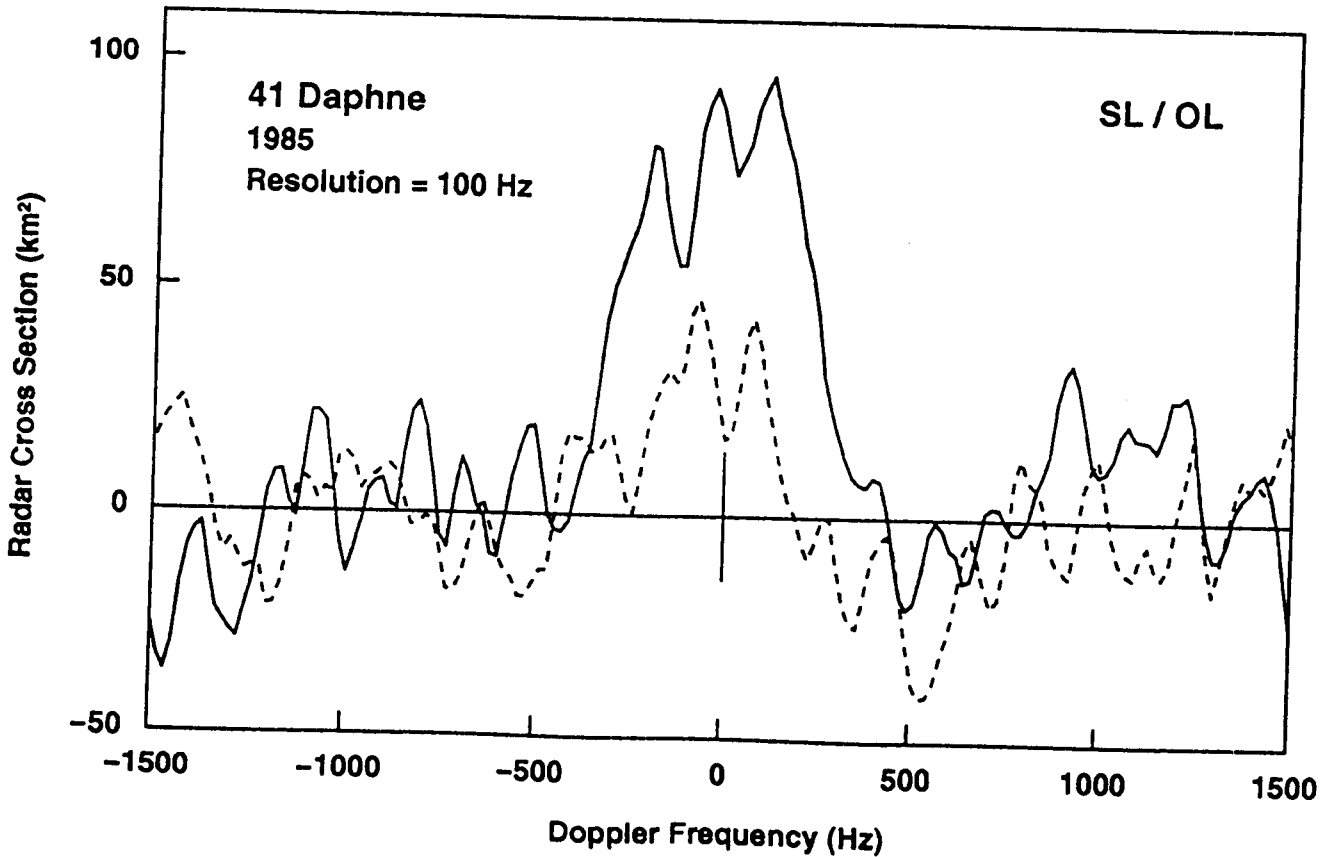
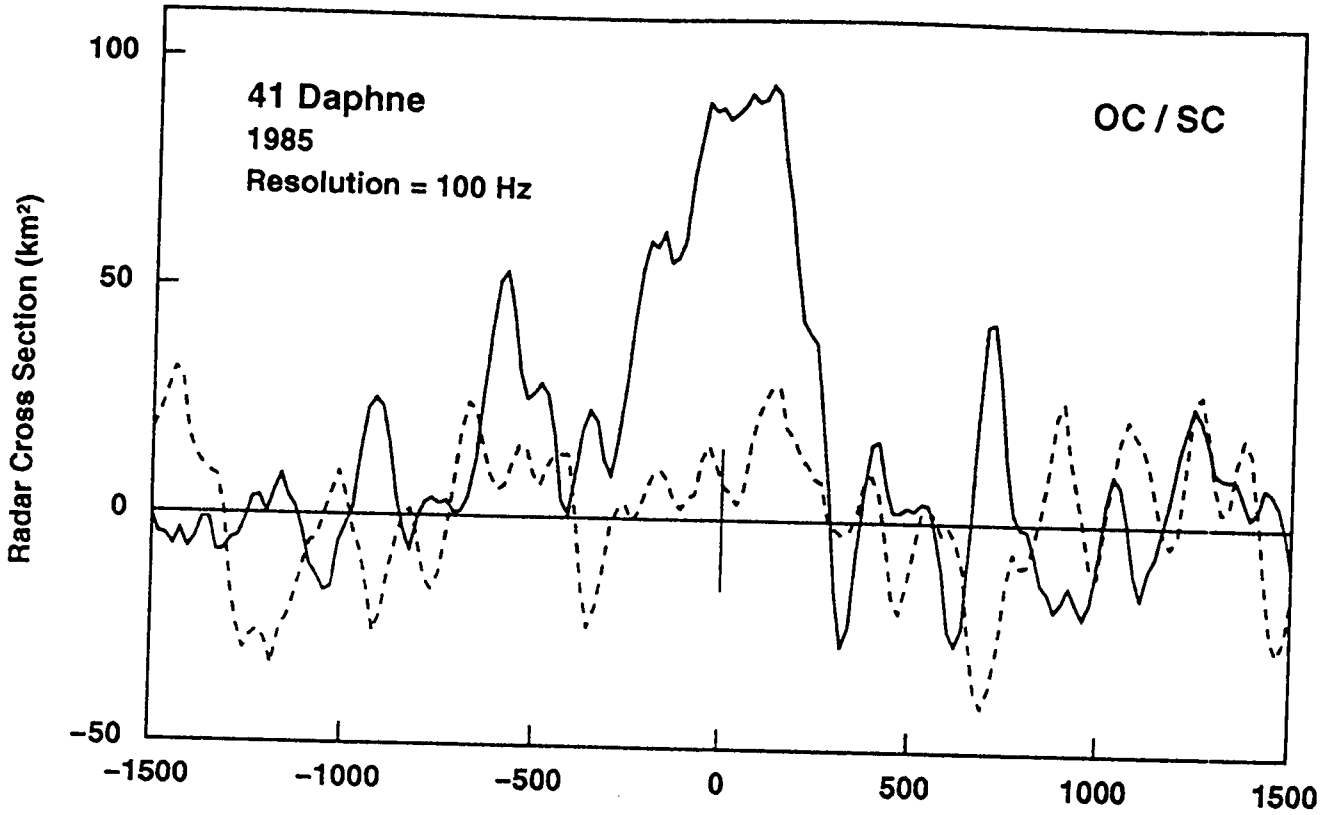


Fig. 6

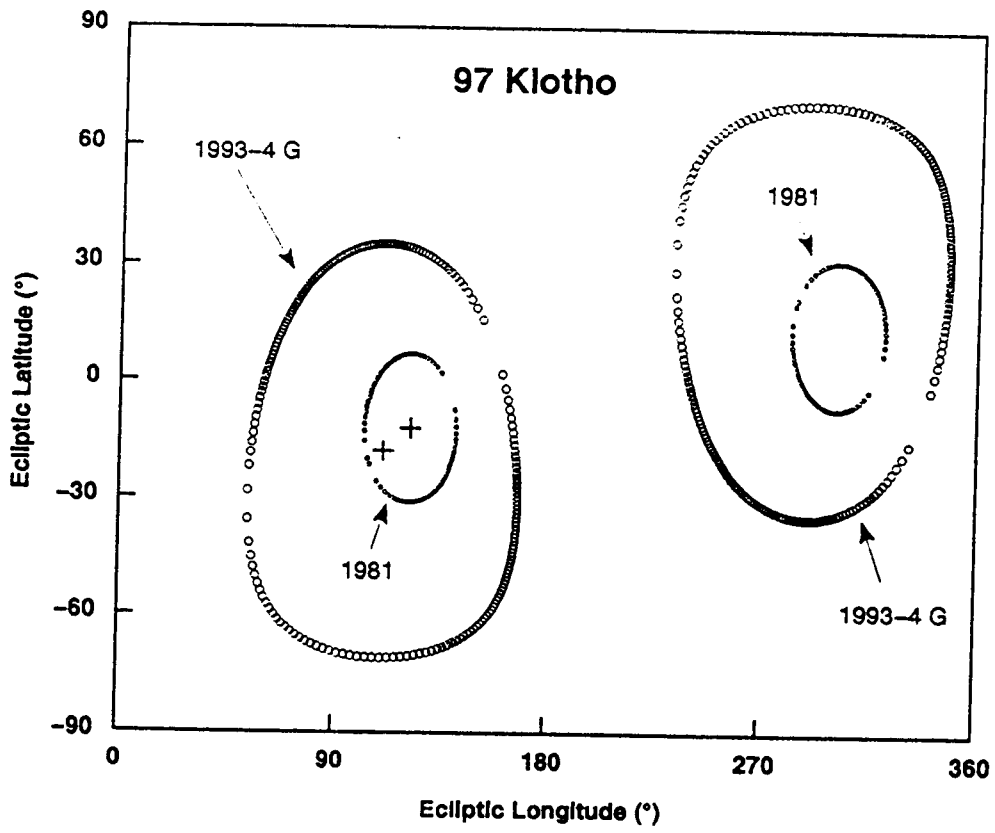


Fig. 7

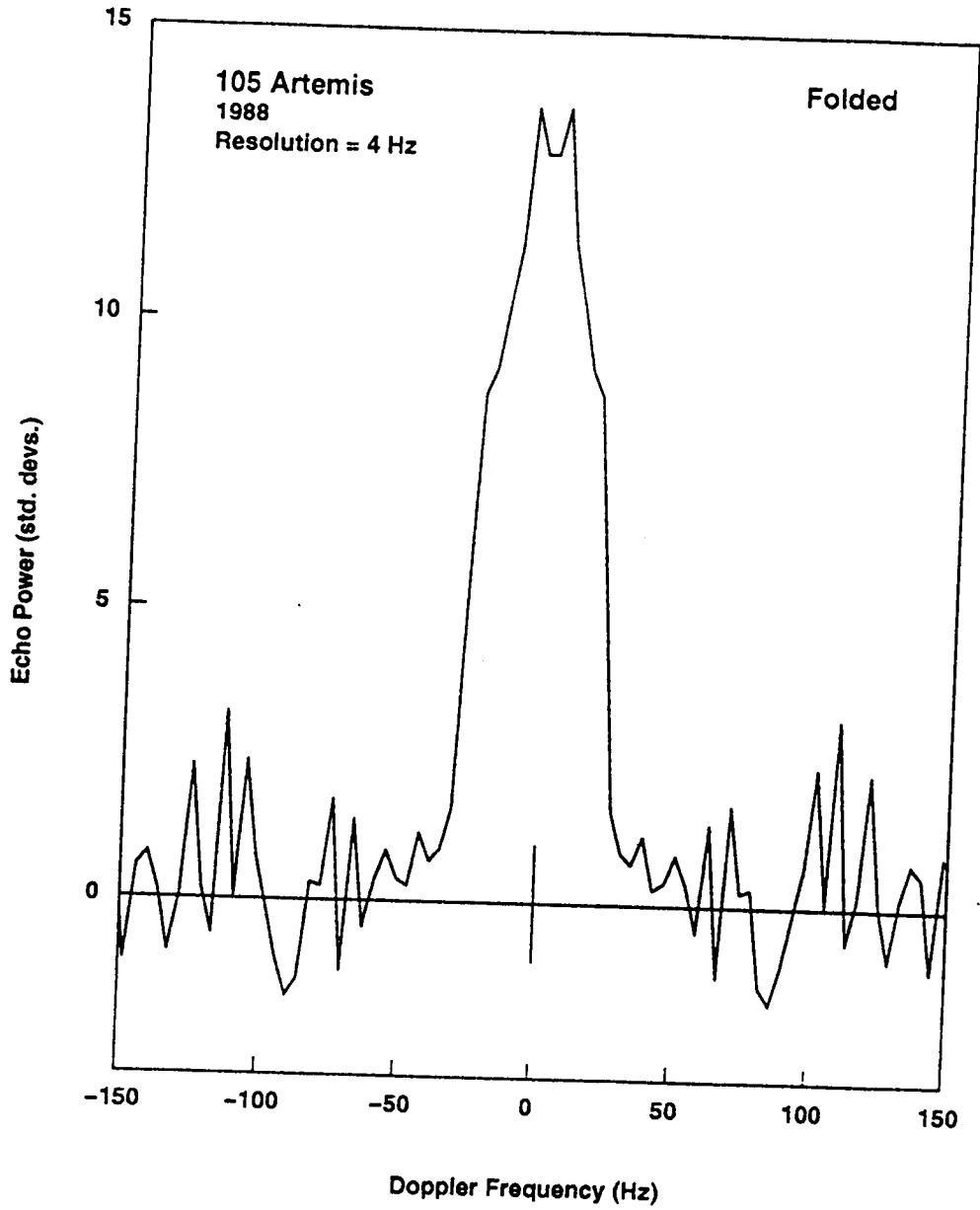


Fig. 8

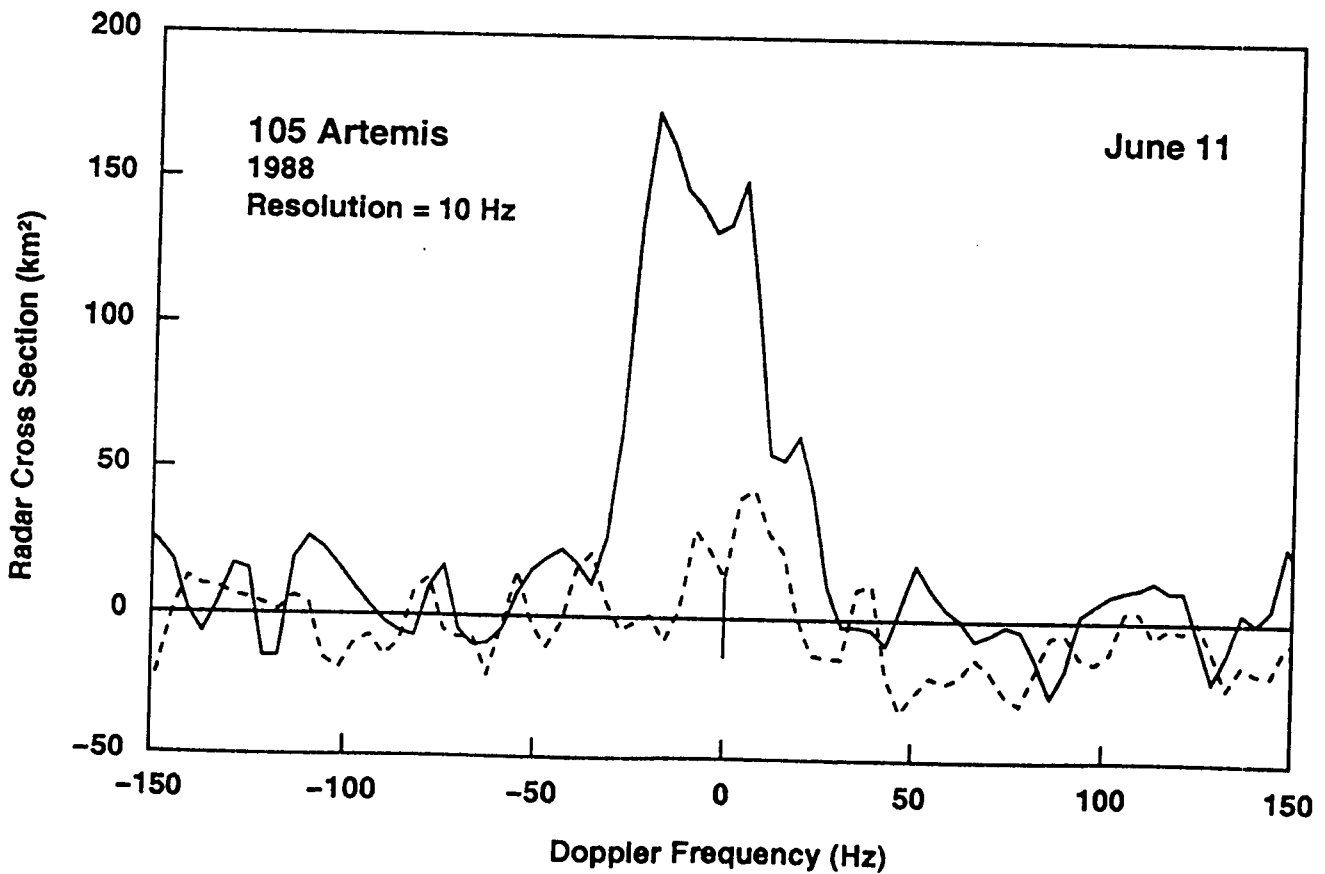
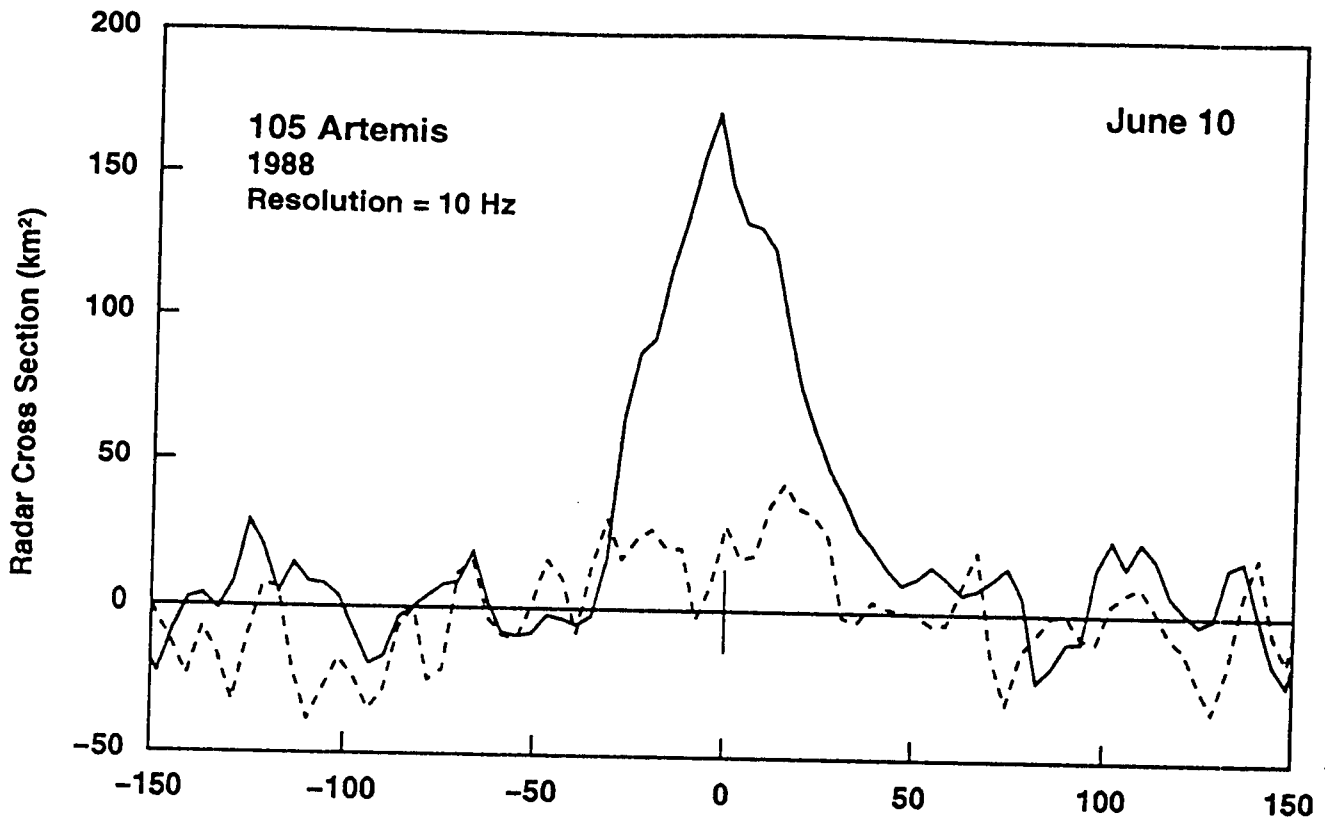


Fig. 9

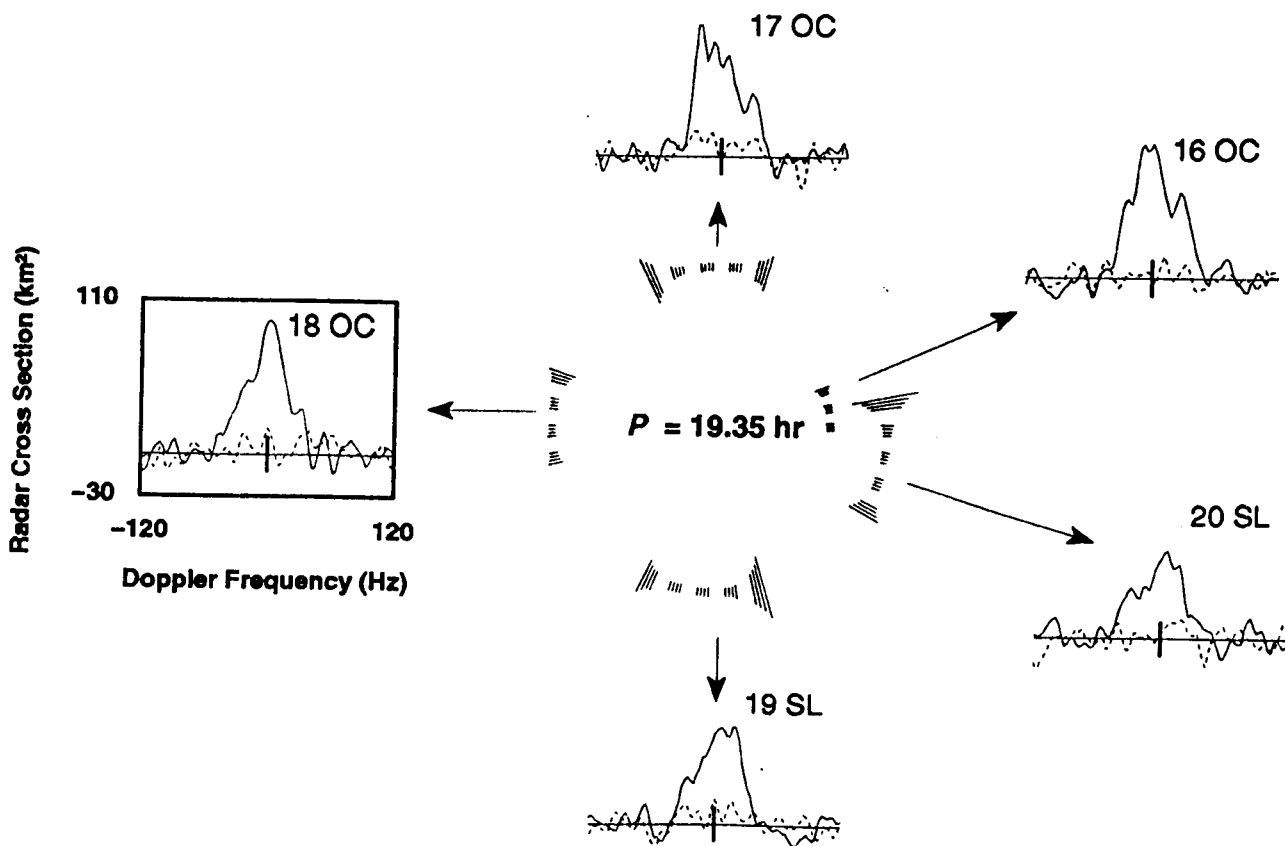
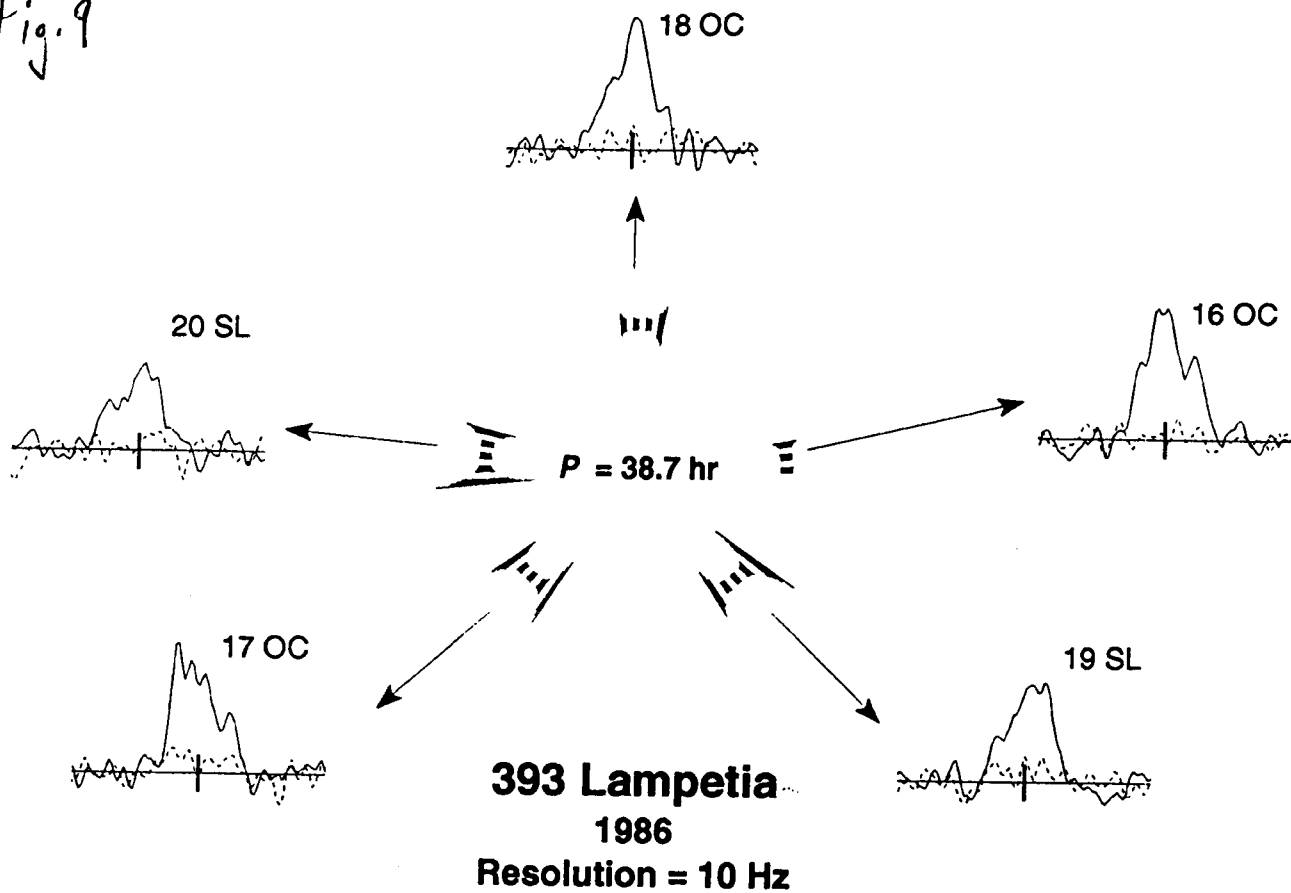


Fig. 10

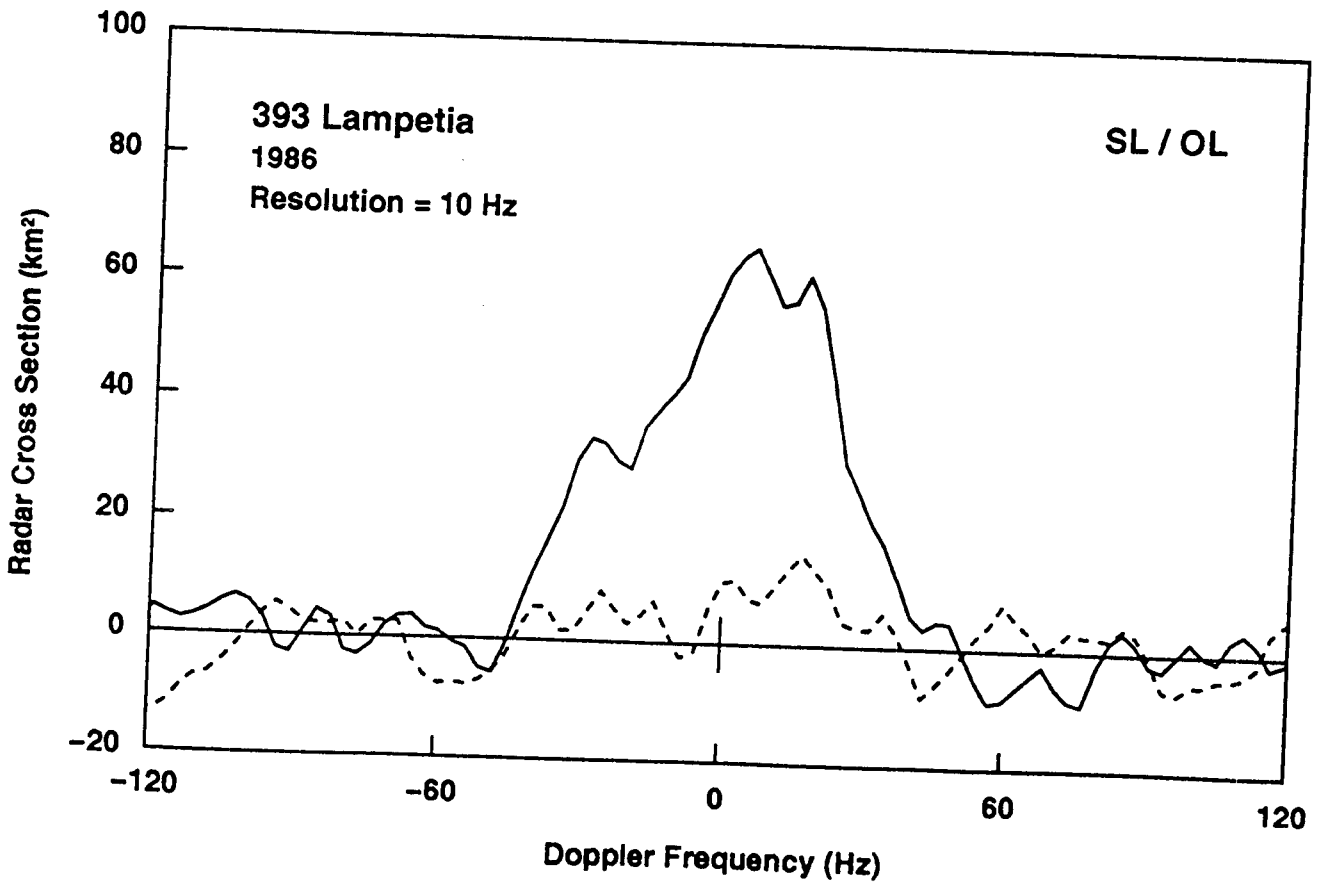
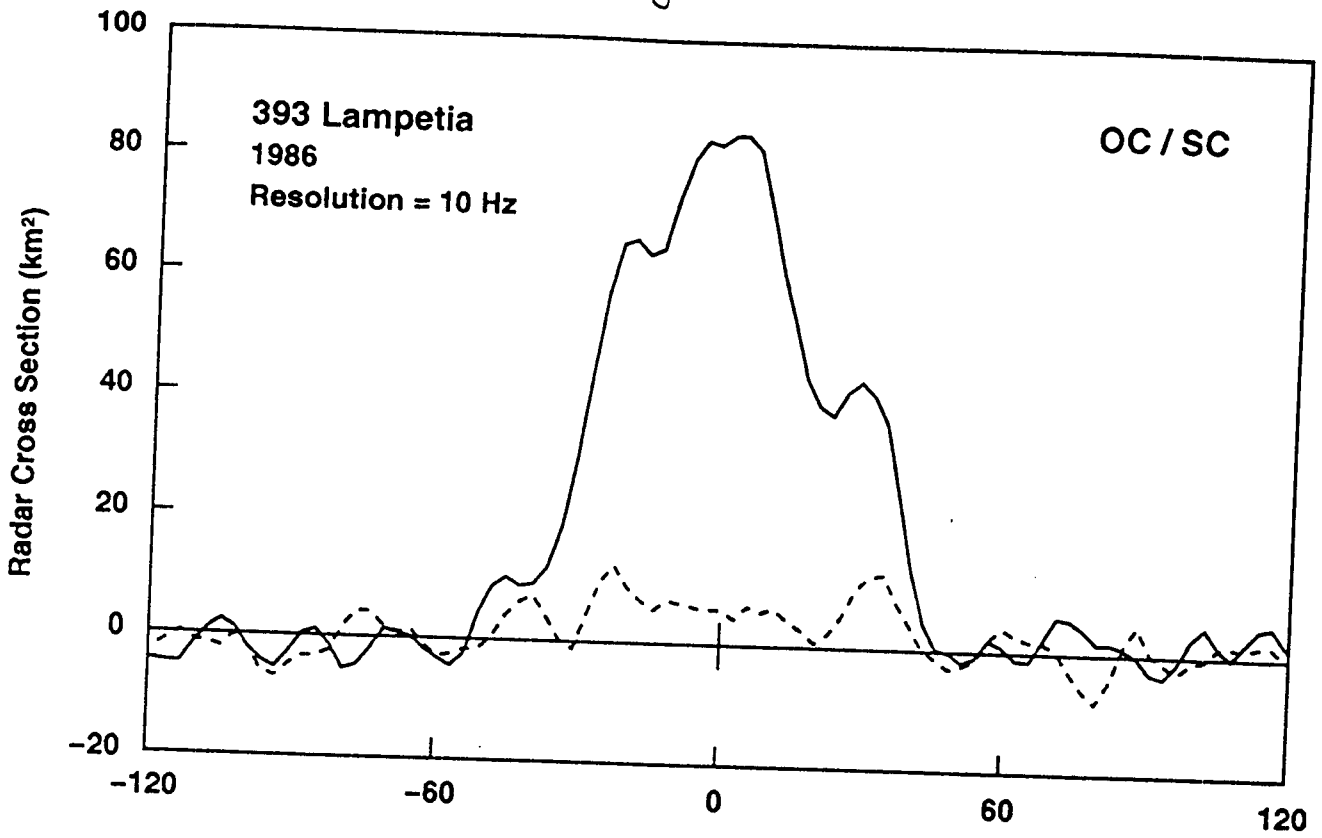


Fig. 11

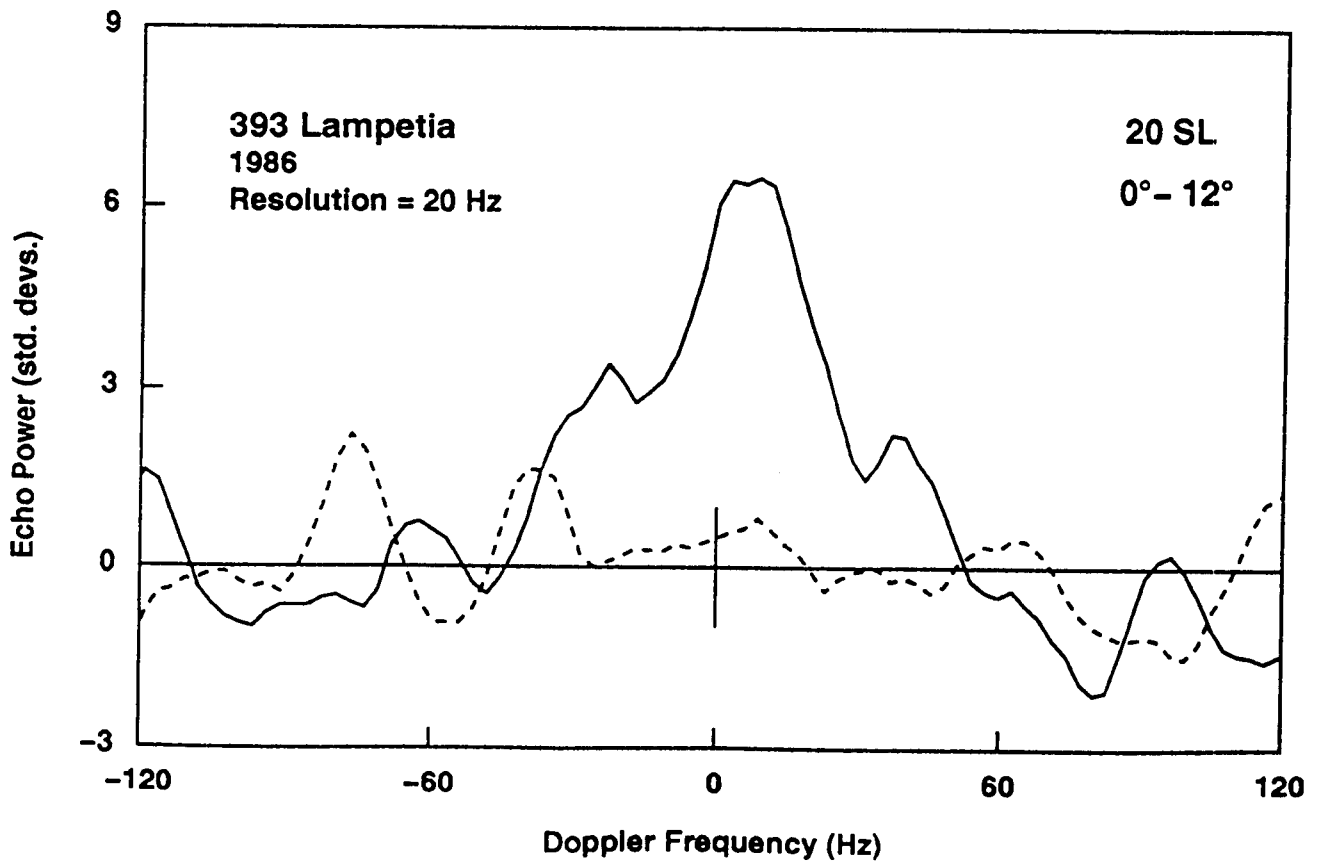
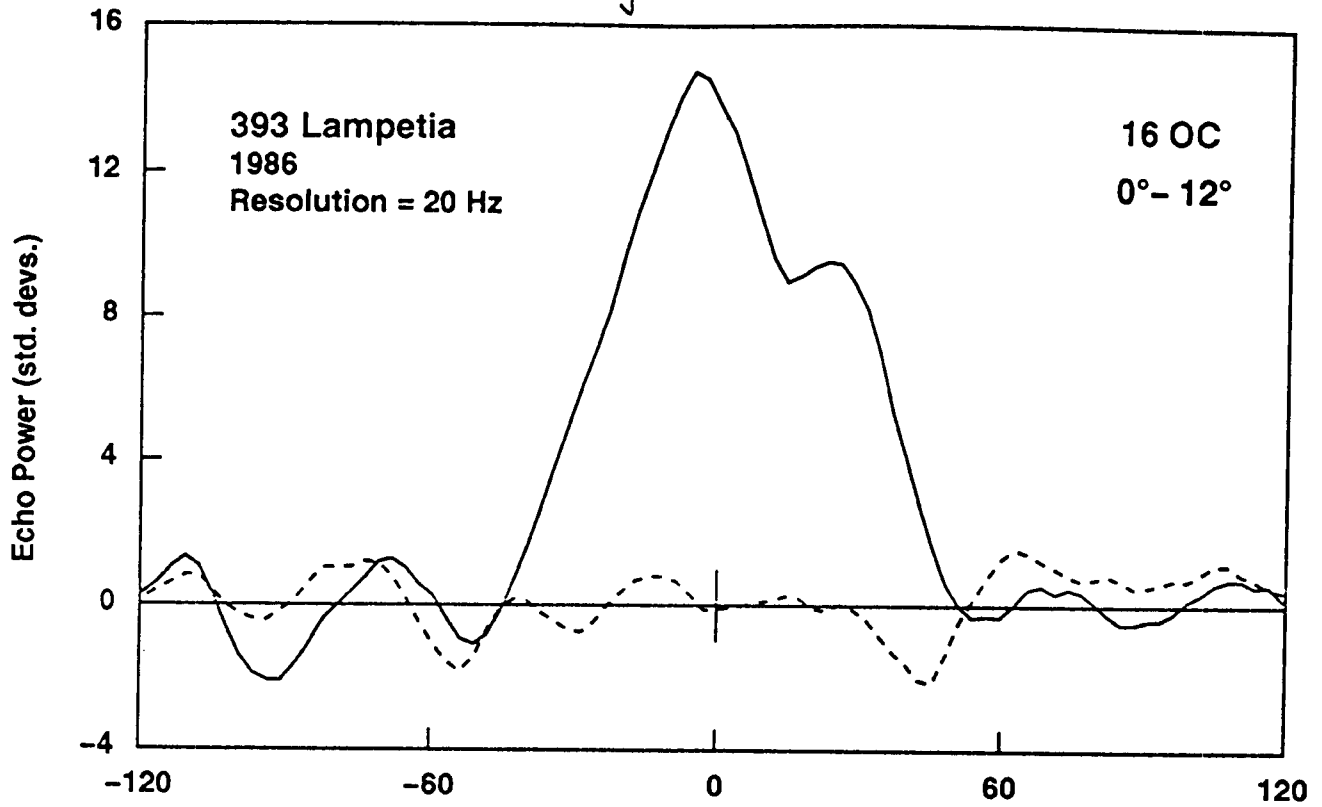


Fig. 12

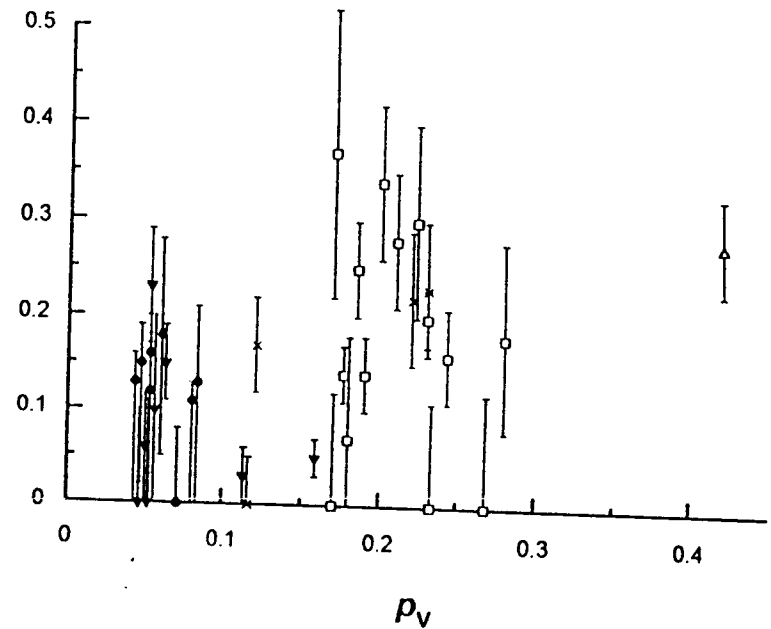
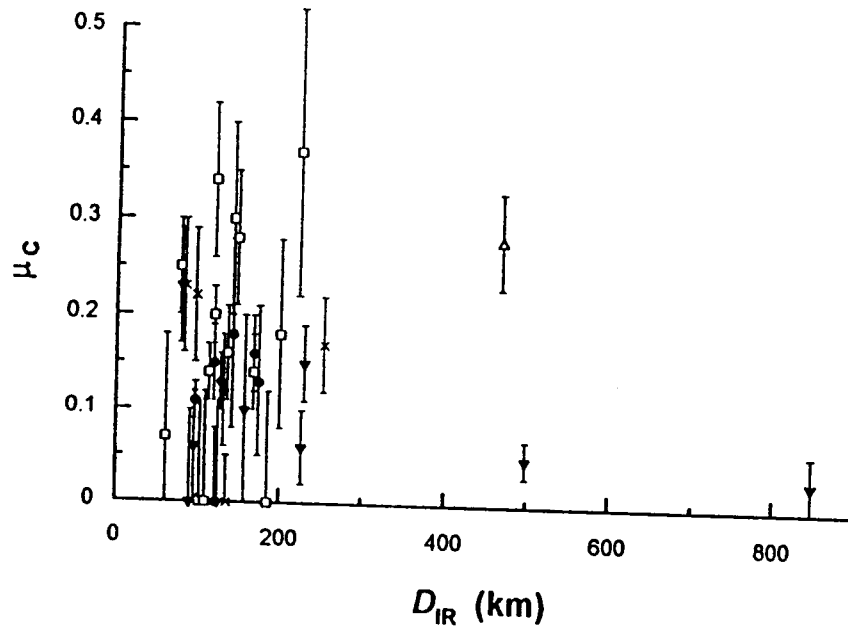
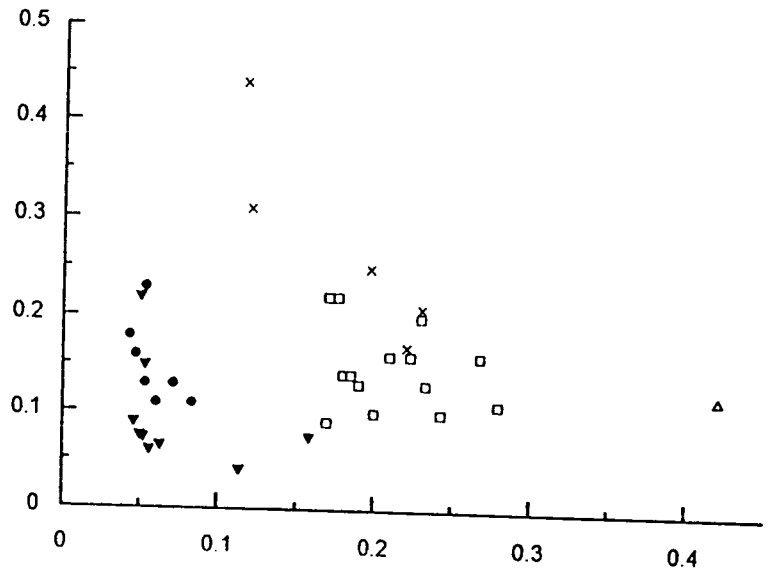
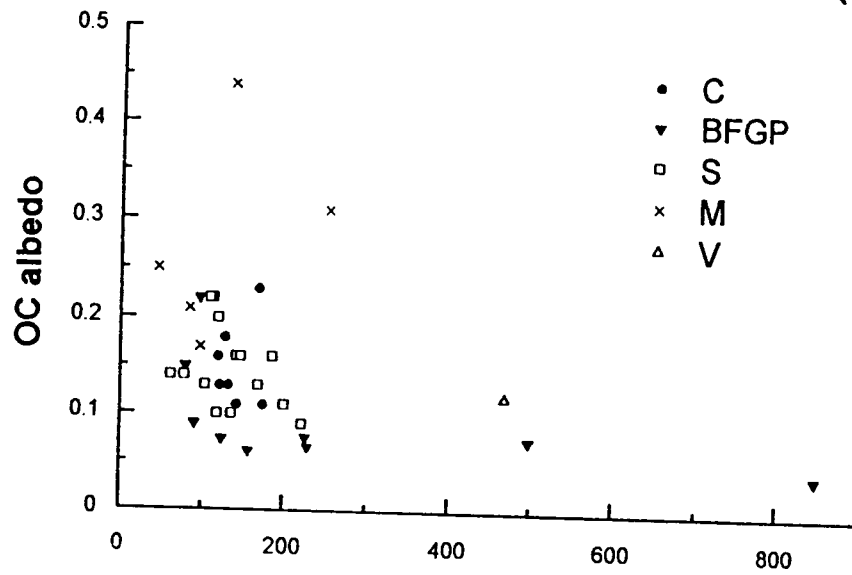


Fig. 13

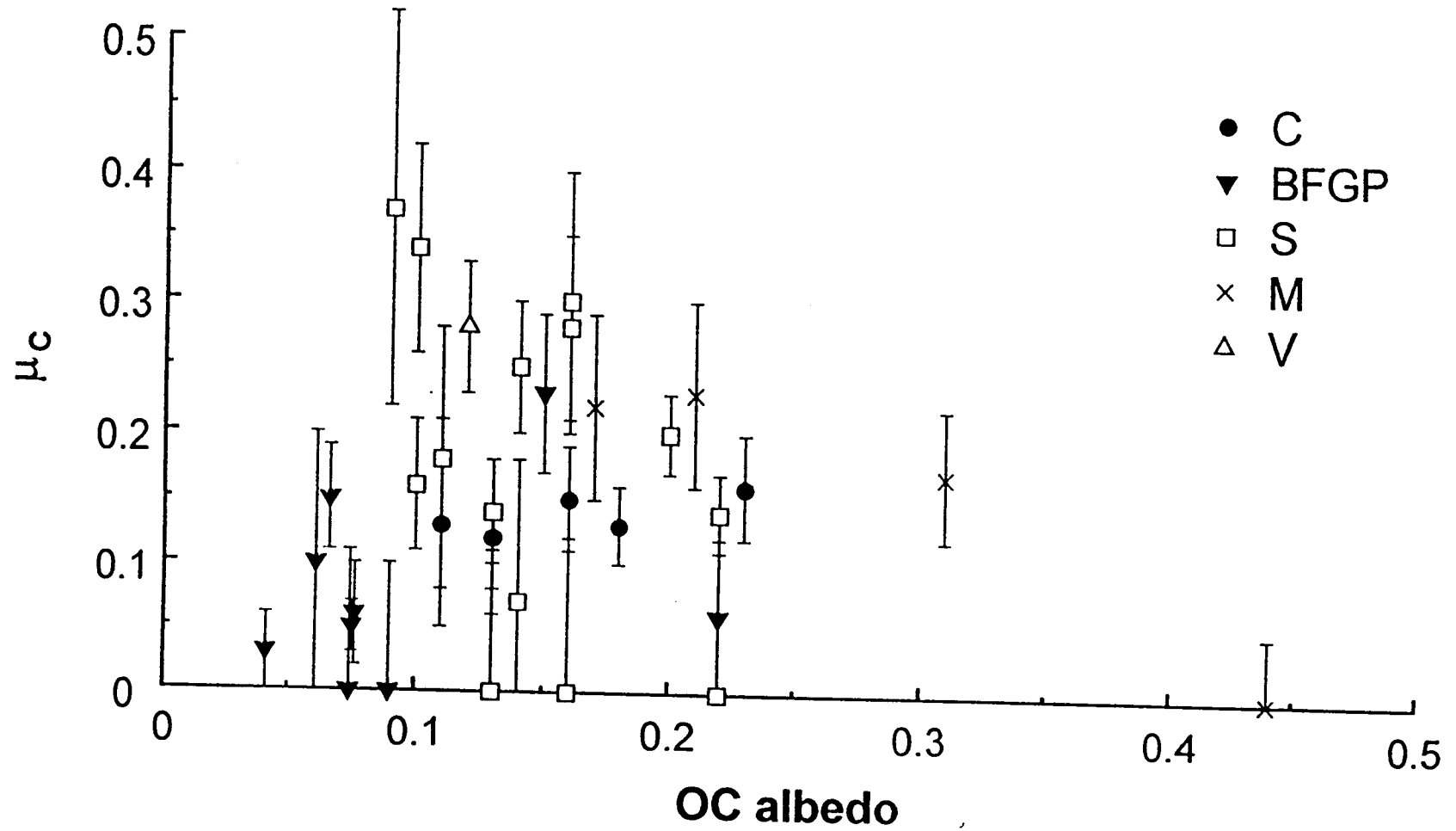
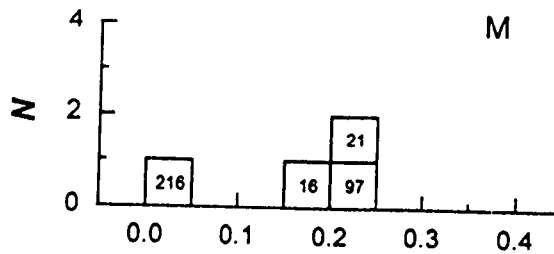
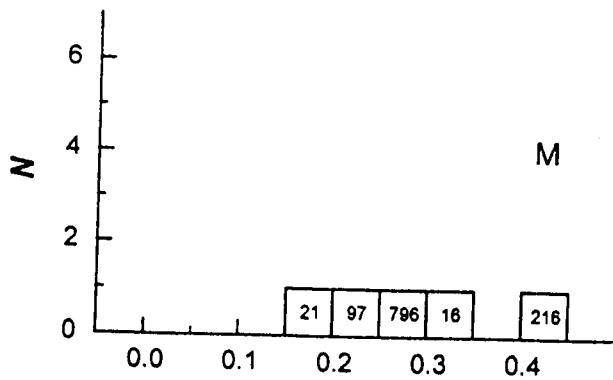
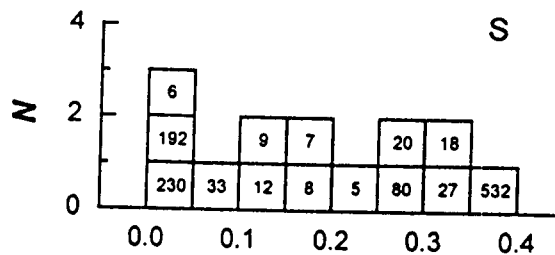
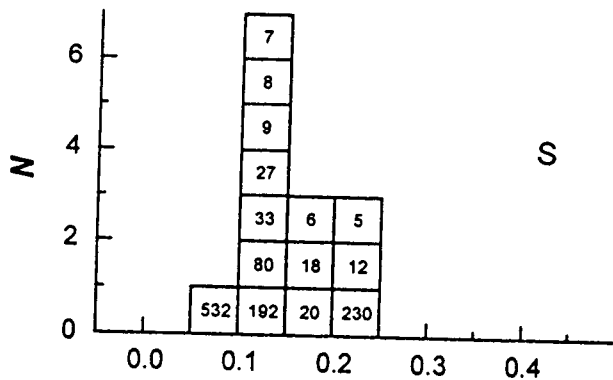
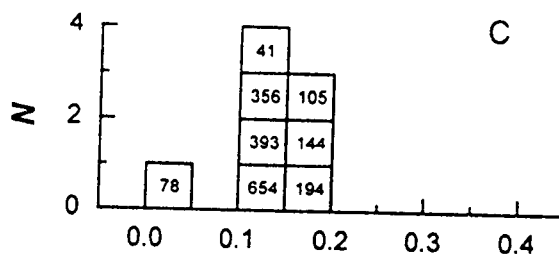
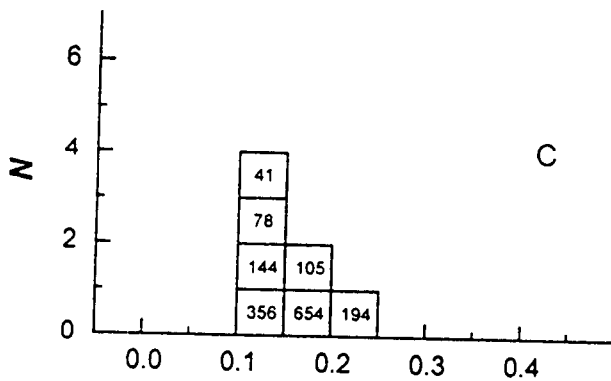
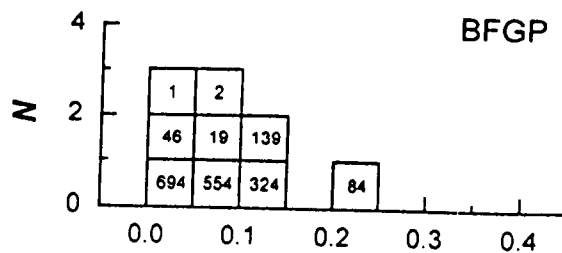
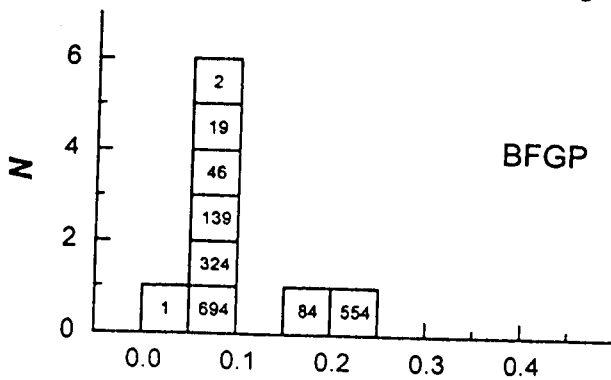


Fig. 14



OC albedo

μ_c

Fig. 15

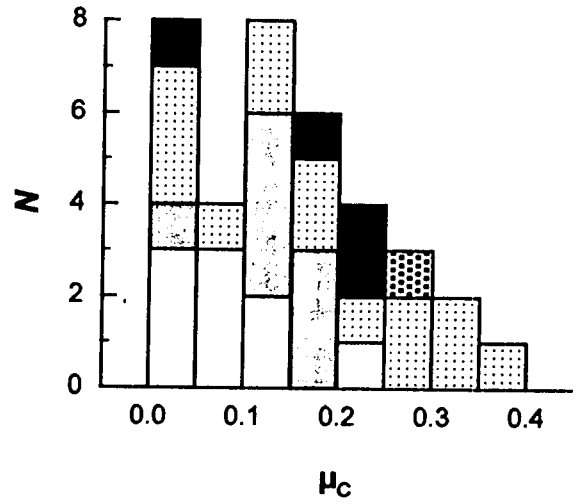
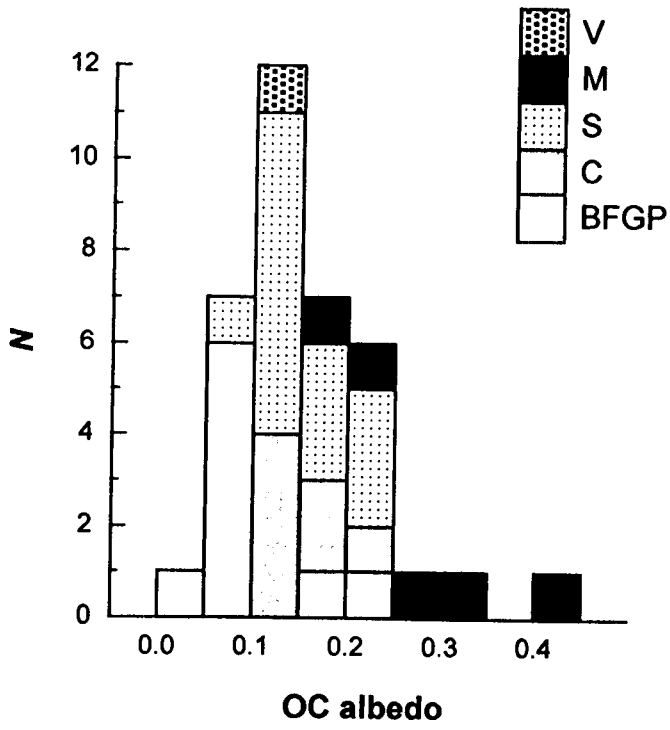


TABLE I
Observations^a

Target	Observing Dates (UT)	Obs.	Pol.	Runs	RA (hr)	Dec (°)	Dist (AU)	Δf (Hz)
5 Astraea	1983 Feb 25, Mar 1-4	A	OC/SC	10	10.8 (0.09)	11 (1.0)	1.13 (0.004)	3
	1987 Feb 5-7	A	OC/SC	10	8.8 (0.03)	16 (0.3)	1.10 (0.002)	3
6 Hebe	1985 Jan 18-23	A	OC/SC	17	6.0 (0.05)	9 (0.9)	1.39 (0.041)	19
7 Iris	1995 Nov 23-25 30, Dec 1-2	G	OC/SC	80	4.4 (0.15)	25 (1.2)	0.87 (0.006)	39
8 Flora	1981 Dec 4-5 7-11	A	OC/SC	19	6.1 (0.12)	18 (0.4)	0.98 (0.010)	20
16 Psyche	1980 Nov 16-23	A	OC/SC	11 ^b	5.2 (0.09)	18 (0.2)	1.70 (0.023)	20
	1985 Dec 7-11	A	OC/SC	10	4.8 (0.06)	18 (0.1)	1.69 (0.009)	19
18 Melpomene	1985 Dec 7-11	A	OC/SC	14	7.3 (0.05)	7 (0.1)	1.20 (0.015)	19
	1995 Sep 11 17 24 26	G	OC/SC	39	23.6 (0.15)	-13 (3.5)	0.83 (0.003)	20
19 Fortuna	1982 Sep 29 -- Oct 3, Oct 5	A	OC/SC	12	1.4 (0.08)	10 (0.6)	1.08 (0.018)	19
	1986 Nov 23-24	A	OC/SC	4	3.7 (0.02)	18 (0.1)	1.10 (0.002)	10
20 Massalia	1987 Dec 2-7	A	OC/SC	21	4.5 (0.09)	21 (0.2)	1.12 (0.001)	5
21 Lutetia	1985 Oct 3-7	A	OC/SC	9	3.1 (0.03)	13 (0.1)	1.32 (0.021)	5
27 Euterpe	1986 Nov 20-24	A	OC/SC	13	2.4 (0.05)	12 (0.2)	1.08 (0.012)	10
33 Polyhymnia	1985 Oct 2 4-6	A	OC/SC	10	1.7 (0.05)	11 (0.2)	0.99 (0.003)	5
41 Daphne	1985 Apr 26-28	A	OC/SC	9	13.1 (0.01)	7 (0.4)	1.10 (0.007)	19
	1985 Apr 25 29-30	A	SL/OL	9	13.1 (0.03)	8 (0.9)	1.11 (0.018)	19
46 Hestia	1982 Nov 12-15	A	OC/SC	12	3.7 (0.05)	16 (0.2)	1.26 (0.002)	19
78 Diana	1990 Jan 11-16	A	OC/SC	16	8.4 (0.09)	29 (0.1)	1.12 (0.010)	5
80 Sappho	1983 Oct 26-31	A	OC/SC	16	2.2 (0.07)	15 (1.0)	0.91 (0.008)	10
84 Klio	1985 Oct 4-7	A	OC/SC	8	0.7 (0.05)	21 (0.0)	0.88 (0.003)	5
97 Klotho	1981 Jan 29 -- Feb 1	A	OC	6	8.1 (0.04)	8 (0.5)	1.23 (0.012)	10
	1993 Dec 30, 1994 Jan 3 7 9-10	G	OC/SC	54	7.3 (0.16)	4 (1.2)	1.12 (0.006)	20
105 Artemis	1988 Jun 10-11	A	OC/SC	6	16.8 (0.01)	16 (0.1)	1.07 (0.003)	4
139 Juewa	1983 Feb 26--Mar 4	A	OC/SC	11	9.8 (0.10)	24 (0.2)	1.37 (0.018)	7
144 Vibia	1984 Oct 25-30	A	OC/SC	7	2.9 (0.07)	11 (0.1)	1.11 (0.003)	10
192 Nausikaa	1985 Oct 2 4-5	A	OC/SC	7	23.7 (0.04)	4 (0.0)	0.83 (0.006)	5
194 Prokne	1990 Jul 30, Aug 1 3	G	OC/SC	25	20.6 (0.05)	1 (1.0)	1.02 (0.007)	20
230 Athamantis	1985 Oct 2 4 6-7	A	OC/SC	6	22.6 (0.04)	7 (0.8)	1.34 (0.027)	5
324 Bambergia	1991 Sep 5-6, Oct 11-13	A	OC/SC	7	22.9 (0.47)	4 (3.2)	0.81 (0.066)	5
	1991 Sep 14	G	OC/SC	4	23.0 (0.00)	4 (0.0)	0.80 (0.000)	39
356 Liguria	1983 Oct 26-31	A	OC/SC	8	1.4 (0.08)	18 (0.1)	1.23 (0.002)	10
393 Lampetia	1986 Jul 16-18	A	OC/SC	12	19.8 (0.02)	11 (0.1)	0.92 (0.002)	3
	1986 Jul 19-20	A	SL/OL	10	19.8 (0.01)	11 (0.0)	0.91 (0.001)	3
532 Herculina	1987 Apr 4 6-8	A	OC/SC	10	13.1 (0.05)	23 (0.3)	1.37 (0.008)	19
554 Peraga	1984 Oct 25-30	A	OC/SC	16	0.8 (0.06)	11 (0.5)	1.11 (0.015)	10
694 Ekard	1983 Oct 26-31	A	OC/SC	16	0.1 (0.01)	17 (1.5)	1.00 (0.032)	10
796 Sarita	1991 Oct 11-13	A	OC	11	3.0 (0.03)	16 (0.4)	0.91 (0.005)	5

^a Transmitter frequency is 2380 MHz for Arecibo (A) and 8510 MHz for Goldstone (G) (except for Prokne, for which it is 8495 MHz). For each experiment we give received polarization(s); the number of transmit-receive cycles, or runs; right ascension, declination, and distance from Earth for epochs near the weighted midpoint of observation (with the range of values spanned in parentheses); and the raw frequency resolution Δf .

^b The 1980 Psyche experiment included 11 runs in which only OC echoes were received, and 5 runs in which only SC echoes were received.

TABLE II
Prior Information

Target	Class ^a	D_{IR}^b	Pole direction ^c				δ_{IR}^d	P^e	Ellipsoid diameters ^f	Obs'n. Year ^g	δ_{rad}^h	$\langle A_{proj} \rangle^i$	D_{eff}^j	$B_{max}(\delta_{rad}=0)^k$
			λ	ref.	β	ref.								
5 Astraea	S	119 ± 12 (6.5)	123 ± 10 (1)	+51 ± 10 (1)	-31 ± 10	16.801	143 x 115 x 100 ± 12%	1983	-34 ± 10	11400 ± 2600	120 ± 14	236 ± 27		
									1987	-37 ± 10	11400 ± 2600	120 ± 14	"	
6 Hebe	S	185 ± 10 (2.9)	358 ± 10 (1)	+40 ± 20 (2)	-10 ± 10	7.274	213 x 187 x 170 ± 8%	1985	+10 ± 10	26900 ± 3000	185 ± 10	811 ± 61		
7 Iris	S	200 ± 20 (10.0)	15 ± 5 (3)	+25 ± 15 (3)	+19 ± 8	7.139	260 x 220 x 155 ± 15%	1995	-34 ± 8	34900 ± 7400	211 ± 22	3610 ± 550		
8 Flora	S	136 ± 7 (2.3)	140 ± 10 (2)	+30 ± 20 (2)	-10 ± 10	12.8	156 x 142 x 124 ± 10%	1981	-30 ± 15	14900 ± 1900	138 ± 9	338 ± 36		
16 Psyche	M	253 ± 25 (4.0)	35 ± 21 (1)	-21 ± 10 (1)	+69 ± 10	4.196	294 x 226 x 174 ± 11%	1980	-45 ± 10	44300 ± 9400	237 ± 25	1940 ± 210		
								1985	-50 ± 10	45800 ± 9700	241 ± 26	"		
18 Melpomene	S	141 ± 14 (2.8)	0 ± 30 (4)	0 ± 15 (4)	+56 ± 20	11.57	169 x 121 x 121 ± 13%	1985	+19 ± 30	14000 ± 4700	134 ± 22	404 ± 52		
								1995 G	-78 ± 25	15700 ± 3200	141 ± 14	1450 ± 190		
19 Fortuna	G	226 ± 34 (---)	79 ± 10 (1)	+51 ± 10 (1)	---	7.443	255 x 206 x 206 ± 18%	1982	-21 ± 10	38900 ± 14200	223 ± 41	951 ± 175		
								1986	-35 ± 10	38900 ± 14200	223 ± 41	"		
20 Massalia	S	146 ± 15 (9.3)	28 ± 10 (1)	+74 ± 10 (1)	-16 ± 10	8.098	166 x 138 x 138 ± 17%	1987	-11 ± 10	16600 ± 3800	145 ± 17	567 ± 95		
21 Lutetia	M	96 ± 10 (4.1)	228 ± 14 (5)	+29 ± 19 (5)	+7 ± 11	8.16	123 x 94 x 82 ± 14%	1985	+65 ± 19	8700 ± 2200	105 ± 13	416 ± 56		
27 Euterpe	S	118 ± 18 (---)	---	---	---	8.5	127 x 110 x 85 ± 20%	1986	---	10900 ± 3900	118 ± 21	414 ± 87		
33 Polyhymnia	S	62 ± 9 (---)	---	---	---	18.60	68 x 59 x 59 ± 19%	1985	---	3000 ± 1100	62 ± 11	101 ± 19		
41 Daphne	C	174 ± 17 (11.7)	342 ± 10 (1)	-34 ± 10 (1)	+5 ± 10	5.988	221 x 170 x 155 ± 13%	1985	+55 ± 10	27400 ± 6300	187 ± 21	1020 ± 130		
46 Hestia	P	124 ± 6 (3.6)	---	---	---	21.7	133 x 121 x 121 ± 11%	1982	---	12100 ± 1800	124 ± 9	170 ± 19		
78 Diana	C	121 ± 6 (2.7)	33 ± 20 (6)	+13 ± 20 (6)	+8 ± 20	7.23	131 x 116 x 116 ± 17%	1990	-4 ± 20	11400 ± 1200	120 ± 6	504 ± 87		
80 Sappho	S	78 ± 10 (1.7)	46 ± 15 (7)	+10 ± 15 (7)	-75 ± 15	14.03	93 x 68 x 36 ± 15%	1983	-76 ± 15	4900 ± 1300	79 ± 10	183 ± 28		
84 Klio	G	79 ± 8 (1.6)	---	---	---	---	79 x 79 x 79 ± 27%	1985	---	4900 ± 1600	79 ± 13	see text		
97 Klotho	M	83 ± 8 (4.5)	---	---	---	35.0	98 x 75 x 75 ± 18%	1981	---	5400 ± 1300	83 ± 10	77 ± 14		
								1993-4 G	---	5400 ± 1100	83 ± 8	277 ± 50		
105 Artemis	C	119 ± 12 (2.8)	---	---	---	17.	135 x 112 x 112 ± 18%	1988	---	11100 ± 3200	119 ± 17	219 ± 55		
139 Juewa	CP	157 ± 16 (2.8)	117 ± 25 (8)	+50 ± 25 (8)	-36 ± 25	20.9 or 41.8	202 x 158 x 99 ± 20%	1983	-46 ± 25	21200 ± 5800	164 ± 22	268 ± 53 or 134 ± 27		
144 Vibia	C	142 ± 7 (2.9)	---	---	---	13.81	153 x 136 x 136 ± 13%	1984	---	15800 ± 2800	142 ± 13	307 ± 40		
192 Nausikaa	S	103 ± 10 (1.9)	320 ± 20 (2)	+45 ± 15 (2)	+46 ± 15	13.62	131 x 97 x 65 ± 14%	1985	-29 ± 15	7100 ± 1900	95 ± 13	267 ± 38		

Table II (Continued)

Target	Class ^a	D_{IR}^h	Pole direction ^c				δ_{IR}^d	P^e	Ellipsoid diameters ^f	Obs'n. Year ^g	δ_{rad}^h	$\langle A_{proj} \rangle^i$	D_{eff}^j	$B_{max}(\delta_{rad}=0)^k$
			λ	ref.	β	ref.								
194 Prokne	C	168 ± 17 (4.1)		---			---	15.67	199 x 153 x 153 ± 20%	1990 G	---	22300 ± 5400	169 ± 20	1260 ± 250
230 Athamantis	S	109 ± 11 (2.0)		---			---	24.0	117 x 105 x 105 ± 17%	1985	---	9300 ± 2400	109 ± 14	135 ± 23
324 Bamberga	CP	229 ± 11 (7.4)		---			+13 ± 30 ^l	29.41	239 x 227 x 227 ± 7%	1991 1991 G	0 ± 30 ^l "	41300 ± 4500 "	229 ± 12 "	225 ± 15 804 ± 55
356 Liguria	C	131 ± 13 (2.6)		---			---	31.82	148 x 124 x 124 ± 17%	1983	---	13500 ± 3000	131 ± 15	129 ± 22
393 Lampetia	C	97 ± 31 (31.4)		---			---	38.7 or 19.35	97 x 97 x 97 ± 32%	1986	---	7400 ± 4800	97 ± 31	89 ± 7 or 139 ± 44
532 Herculina	S	222 ± 22 (7.6)	290 ± 10 (9)		+30 ± 15 (9)		-60 ± 20	9.405	244 x 204 x 185 ± 14%	1987	-3 ± 10	33700 ± 8000	207 ± 25	720 ± 97
554 Peraga	FC	96 ± 10 (4.1)		---			---	13.63	108 x 90 x 90 ± 18%	1984	---	7200 ± 1900	96 ± 13	220 ± 40
694 Ekard	CP:	91 ± 12 (4.0)	96 ± 10 (1)		+31 ± 10 (1)		-4 ± 10	5.922	135 x 97 x 69 ± 17%	1983	-9 ± 10	6500 ± 1800	91 ± 13	633 ± 105
796 Sarita	XD ^m	45 ± 5 (1.5)		---			---	7.75	53 x 41 x 41 ± 20%	1991	---	1590 ± 420	45 ± 6	188 ± 37

^a Taxonomic classification (Tholen 1989) based on visual and infrared data.

^b Radiometric diameter (in km), based on IRAS data (Tedesco 1997) when available, or else taken from the TRIAD compilation (Bowell *et al.* 1979). These diameters assume a spherical asteroid that obeys the Standard Thermal Model (Lebofsky and Spencer 1989). Formal uncertainties derived by Tedesco on this assumption are given in parentheses. Departures from sphericity may bias diameter estimates to an extent that depends on the asteroid's shape and its orientation at the time of the infrared observations (Brown 1985). Our adopted uncertainties have been increased accordingly.

^c Ecliptic coordinates (in degrees) of the spin vector. Most of our targets have ambiguous pole solutions; we have listed only one possible pole direction per target, as others predict similar viewing geometries for IRAS and radar observations. References listed in parentheses: (1) consensus ("synthesis") value from Magnusson (1995), with 10° error assumed; (2) Magnusson (1995) lists several published pole solutions but no consensus value, so we have formulated an estimate whose one-sigma uncertainty range encompasses the individual published estimates; (3) Mitchell *et al.* (1995); (4) Hoffmann and Geyer (1990); (5) same as (2), but with solution from Michałowski (1996) considered in addition to earlier estimates compiled by Magnusson (1995); (6) Harris and Young (1989); (7) Michałowski (1993), but with error increased from 6° to 15°; (8) Michałowski (1993), but with error increased from roughly 13° to 25°; (9) same as (2), but with solutions from Michałowski *et al.* (1995) and Michałowski (1996) considered in addition to earlier estimates compiled by Magnusson (1995).

^d Sub-IRAS latitude (in degrees) over the duration of IRAS observations, based on photometric pole estimates (Magnusson 1995).

^e Sidereal rotation period (in hours), taken from Lagerkvist *et al.* (1996) and references therein.

^f Adopted axis dimensions (in km) based on a combination of radiometric, lightcurve, and occultation data (see text). The stated percentage uncertainty refers to the largest diameter $2a$.

^g Year of radar observation. Goldstone observations are identified by a G.

^h Sub-radar latitude (in degrees) over the duration of radar observations, based on photometric pole estimates (Magnusson 1995).

ⁱ Mean projected area (in km²) of the reference ellipsoid as viewed by the radar. This is an unweighted mean over all rotation phases. The stated uncertainty incorporates uncertainties in the axis lengths, differences between IRAS and radar viewing geometries, and the rotational phase coverage for the IRAS and radar data.

^j Effective diameter (in km) of the target. By definition, the mean projected area of the reference ellipsoid as viewed by the radar is equal to $\pi D_{eff}^2 / 4$. Uncertainties propagate from those stated for $\langle A_{proj} \rangle$.

^k Maximum-breadth echo bandwidth (in Hz) predicted by the reference ellipsoid for a spectral sum obtained with an equatorial view and complete rotational phase coverage. Uncertainties propagate from those stated for diameter $2a$; for Flora, Euterpe, and Artemis, significant uncertainties in P have also been factored in.

^l Sub-IRAS and sub-radar latitudes stated for Bamberga are based on the analysis of monostatic and bistatic radar data by de Pater *et al.* (1994).

^m Sarita is probably an M-class object; see text.

TABLE III
Published Pole Determinations for Lutetia ^a

Reference	λ_1	β_1	λ_2	β_2	a/b	b/c
Lupishko and Velichko (1987)						
Lupishko <i>et al.</i> (1987)	42 ± 5	$+40 \pm 9$	223 ± 7	$+48 \pm 7$	1.25	1.09
Michałowski (1992)	55 ± 8	$+44 \pm 5$	241 ± 9	$+40 \pm 8$	1.30 ± 0.06	1.7 ± 0.5^b
Dotto <i>et al.</i> (1992) ^c	48 ± 10	$+31 \pm 1$	233 ± 10	$+38 \pm 2$	1.29 ± 0.02	1.25 ± 0.06
Michałowski (1993)	33 ± 7	$+9 \pm 8$	214 ± 6	$+15 \pm 7$	1.25 ± 0.01	2.7 ± 1.0
De Angelis (1995)	41 ± 6	$+42 \pm 10$		---	1.41 ± 0.01	1.08 ± 0.10
Lagerkvist <i>et al.</i> (1995)	50 ± 10	$+10 \pm 10$	230 ± 10	$+10 \pm 10$	1.22 ± 0.05	1.4 ± 0.4
Michałowski (1996)		---	240 ± 8	$+37 \pm 10$	1.26 ± 0.02	1.15 ± 0.03

^a Ecliptic coordinates (in degrees) of the pole, and associated model axis ratios, for published solutions based on optical photometry.

^b Listed estimate of b/c is a mean of two discrepant estimates, 2.01 ± 0.28 and 1.36 ± 0.30 , published for pole solutions 1 and 2, respectively.

^c Dotto *et al.* (1992) do not determine the sense of rotation; we have omitted the two retrograde pole directions from the table.

TABLE IV
Radar Properties by Experiment

Target	Obs'n. Year ^a	OC SNR ^b	B_{eq} (Hz) ^c	B (Hz) ^d	μ_c ^e	σ_{oc} (km ²) ^f	D_{eff} (km) ^g	$\hat{\sigma}_{oc}$ ^h
5 Astraea	1983	23	120 ± 10	180 ± 20	0.20 ± 0.04	2400 ± 600	120 ± 14	0.21 ± 0.08
	1987	24	120 ± 10	175 ± 20	0.20 ± 0.04	2190 ± 550	120 ± 14	0.19 ± 0.07
6 Hebe	1985	8	600 ± 50	---	0.00 ± 0.12	4300 ± 1200	185 ± 10	0.16 ± 0.05
7 Iris	1995 G	60	2350 ± 100	2840 ± 100	0.33 ± 0.04	4700 ± 1200	211 ± 22	0.13 ± 0.04
8 Flora	1981	18	220 ± 20	400 ± 30	0.16 ± 0.05	1500 ± 380	138 ± 9	0.10 ± 0.03
16 Psyche	1980	10	≥ 520	840 ± 40	0.14 ± 0.10	14000 ± 3700	237 ± 25	0.32 ± 0.12
	1985	16	600 ± 50	875 ± 100	0.18 ± 0.06	14300 ± 3700	241 ± 26	0.31 ± 0.11
18 Melpomene	1985	10	240 ± 20	≥ 270	0.30 ± 0.09	2000 ± 530	134 ± 22	0.14 ± 0.07
	1995 G	33	680 ± 50	≥ 810	0.30 ± 0.15	2810 ± 710	141 ± 14	0.18 ± 0.06
19 Fortuna	1982	20	550 ± 30	700 ± 50	0.04 ± 0.04	3200 ± 820	223 ± 41	0.082 ± 0.042
	1986	8	≥ 330	---	0.12 ± 0.08	2710 ± 710	223 ± 41	0.070 ± 0.036
20 Massalia	1987	11	290 ± 20	≥ 380	0.28 ± 0.07	2580 ± 670	145 ± 17	0.16 ± 0.06
21 Lutetia	1985	15	41 ± 10	58 ± 10	0.22 ± 0.07	1800 ± 460	116 ± 17	0.17 ± 0.07
27 Euterpe	1986	11	195 ± 10	≥ 260	0.34 ± 0.08	1110 ± 290	118 ± 21	0.10 ± 0.05
33 Polyhymnia	1985	8	≥ 55	≥ 70	0.07 ± 0.11	410 ± 110	62 ± 11	0.14 ± 0.07
41 Daphne	1985	11	≥ 480	≥ 540	0.13 ± 0.08	2900 ± 770	187 ± 21	0.11 ± 0.04
46 Hestia	1982	9	≥ 90	---	0.00 ± 0.11	900 ± 250	124 ± 9	0.074 ± 0.024
78 Diana	1990	9	345 ± 30	465 ± 30	0.00 ± 0.08	1440 ± 380	120 ± 6	0.13 ± 0.04
80 Sappho	1983	18	77 ± 10	170 ± 40	0.25 ± 0.05	650 ± 160	79 ± 10	0.14 ± 0.05
84 Klio	1985	17	80 ± 10	≥ 105	0.23 ± 0.06	760 ± 190	79 ± 13	0.15 ± 0.07
97 Klotho	1981	6	45 ± 10	---	---	1100 ± 320	83 ± 10	0.20 ± 0.08
	1993-4 G	14	245 ± 20	310 ± 20	0.23 ± 0.07	1200 ± 310	83 ± 8	0.22 ± 0.08
105 Artemis	1988	28	58 ± 5	≥ 70	0.15 ± 0.04	1800 ± 440	119 ± 17	0.16 ± 0.07
139 Juewa	1983	8	≥ 70	---	0.10 ± 0.10	1300 ± 350	164 ± 22	0.061 ± 0.025
144 Vibilia	1984	9	≥ 130	---	0.18 ± 0.10	1800 ± 500	142 ± 13	0.11 ± 0.04
192 Nausikaa	1985	8	90 ± 10	≥ 115	0.00 ± 0.11	890 ± 240	95 ± 13	0.13 ± 0.05
194 Prokne	1990 G	23	530 ± 15	750 ± 50	0.16 ± 0.04	5200 ± 1300	169 ± 20	0.23 ± 0.09
230 Athamantis	1985	6	≥ 45	---	0.00 ± 0.12	2080 ± 570	109 ± 14	0.22 ± 0.09
324 Bamberg	1991	30	155 ± 10	≥ 195	0.14 ± 0.03	2880 ± 860	229 ± 12	0.070 ± 0.021
	1991 G	20	630 ± 40	≥ 720	0.18 ± 0.05	3030 ± 910	"	0.074 ± 0.022
356 Liguria	1983	14	72 ± 10	≥ 115	0.12 ± 0.06	1800 ± 460	131 ± 15	0.13 ± 0.05

Table IV (Continued)

Target	Obs'n. Year ^a	OC SNR ^b	B_{eq} (Hz) ^c	B (Hz) ^d	μ_c ^e	σ_{oc} (km ²) ^f	D_{eff} (km) ^g	$\hat{\sigma}_{oc}$ ^h
393 Lampetia	1986	44	70 ± 5	100 ± 10	0.11 ± 0.02	1550 ± 390	125 ± 12 ⁱ or 97 ± 31	0.13 ± 0.04 ⁱ or 0.21 ^{+0.40} -0.09
532 Herculina	1987	8	330 ± 40	≥ 450	0.37 ± 0.15	3000 ± 1500	207 ± 25	0.09 ± 0.05
554 Peraga	1984	14	150 ± 20	≥ 190	0.06 ± 0.06	1600 ± 400	96 ± 13	0.22 ± 0.09
694 Ekard	1983	8	200 ± 40	≥ 250	0.00 ± 0.10	610 ± 160	91 ± 13	0.09 ± 0.04
796 Sarita	1991	8	150 ± 20	----	----	390 ± 100	45 ± 6	0.25 ± 0.10

^a Year of radar observation. Goldstone observations are identified by a G.

^b The OC SNR is the signal-to-noise ratio for an optimally filtered, weighted sum of all echo spectra.

^c By definition (Tiuri 1964), equivalent bandwidth $B_{eq} = \Delta f [(\sum S_i)^2 / \sum S_i^2]$, where S_i are the OC spectral elements and Δf is the "raw" frequency resolution. Stated values of B_{eq} are computed using unfolded spectra. Wishing to smooth in frequency just enough to minimize the influence of random baseline noise on our estimate, we compute B_{eq} for several frequency resolutions. These values sometimes exhibit large fluctuations at fine resolutions, but they become more stable, and increase slowly and steadily at coarser resolutions. In such cases, stated values of B_{eq} refer to an optimal resolution at the boundary between these two regimes; otherwise we use the raw resolution as the optimal resolution. Uncertainties are subjectively determined by inspecting the fluctuations in B_{eq} near the optimal resolution.

^d B is the zero-crossing bandwidth of the weighted sum of all OC spectra, folded about zero Doppler and smoothed in frequency. The optimal degree of smoothing is determined as described above for B_{eq} ; coarser effective resolution is usually required for estimating B than for estimating B_{eq} . Uncertainties are subjectively determined by inspecting the fluctuations in B near the optimal resolution.

^e μ_c is the circular polarization ratio, SC/OC. Uncertainties quoted for μ_c are obtained by first determining, for both the SC and the OC spectrum, the standard deviation of the receiver noise in the OC equivalent bandwidth (B_{eq}). The larger of these two values is used as the standard deviation for both the numerator and the denominator of the polarization ratio, and the error on μ_c is computed accordingly (Ostro *et al.* 1983).

^f σ_{oc} is the OC radar cross section. Assigned uncertainties are the root sum square of systematic calibration errors, estimated as 25% of the cross-section values, and the standard deviation of the receiver noise in the equivalent bandwidth (B_{eq}).

^g D_{eff} is the effective diameter of the target. By definition, the mean projected area of the reference ellipsoid as viewed by the radar is equal to $\pi D_{eff}^2 / 4$. The stated uncertainty incorporates uncertainties in the axis lengths, differences between IRAS and radar viewing geometries, and rotational phase coverage for the IRAS and radar data.

^h The radar albedo, $\hat{\sigma}_{oc}$, is equal to $\sigma_{oc} / (\pi D_{eff}^2 / 4)$. Uncertainties propagate from those given for σ_{oc} and D_{eff} (Ostro *et al.* 1983).

ⁱ For Lampetia, the top values of D_{eff} and $\hat{\sigma}_{oc}$ refer to a period of 38.7 hr; the bottom values refer to $P = 19.35$ hr. See text for discussion.

TABLE V
Average Radar Properties ^a

<i>Ordered by ID Number</i>				<i>Ordered by Descending Polarization Ratio</i>			
Target	Class	$\langle \mu_c \rangle$	$\langle \hat{\sigma}_{cc} \rangle$	Target	Class	$\langle \mu_c \rangle$	$\langle \hat{\sigma}_{cc} \rangle$
1 Ceres ^b	G	0.03 ± 0.03	0.041 ± 0.005	532 Herculina	S	0.37 ± 0.15	0.09 ± 0.05
2 Pallas ^b	B	0.05 ± 0.02	0.075 ± 0.011	27 Euterpe	S	0.34 ± 0.08	0.10 ± 0.05
4 Vesta ^b	V	0.28 ± 0.05	0.12 ± 0.04	18 Melpomene	S	0.30 ± 0.10	0.16 ± 0.05
5 Astraea	S	0.20 ± 0.03	0.20 ± 0.05	4 Vesta	V	0.28 ± 0.05	0.12 ± 0.04
6 Hebe	S	0.00 ± 0.12	0.16 ± 0.05	20 Massalia	S	0.28 ± 0.07	0.16 ± 0.06
7 Iris ^c	S	0.18 ± 0.10	0.11 ± 0.03	80 Sappho	S	0.25 ± 0.05	0.14 ± 0.05
8 Flora	S	0.16 ± 0.05	0.10 ± 0.03	84 Klio	G	0.23 ± 0.06	0.15 ± 0.07
9 Metis ^b	S	0.14 ± 0.04	0.13 ± 0.03	97 Klotho	M	0.23 ± 0.07	0.21 ± 0.06
12 Victoria ^b	S	0.14 ± 0.03	0.22 ± 0.05	21 Lutetia	M	0.22 ± 0.07	0.17 ± 0.07
16 Psyche	M	0.17 ± 0.05	0.31 ± 0.08	5 Astraea	S	0.20 ± 0.03	0.20 ± 0.05
18 Melpomene	S	0.30 ± 0.10	0.16 ± 0.05	7 Iris	S	0.18 ± 0.10	0.11 ± 0.03
19 Fortuna	G	0.06 ± 0.04	0.076 ± 0.027	144 Vibia	C	0.18 ± 0.10	0.11 ± 0.04
20 Massalia	S	0.28 ± 0.07	0.16 ± 0.06	16 Psyche	M	0.17 ± 0.05	0.31 ± 0.08
21 Lutetia	M	0.22 ± 0.07	0.17 ± 0.07	8 Flora	S	0.16 ± 0.05	0.10 ± 0.03
27 Euterpe	S	0.34 ± 0.08	0.10 ± 0.05	194 Prokne	C	0.16 ± 0.04	0.23 ± 0.09
33 Polyhymnia	S	0.07 ± 0.11	0.14 ± 0.07	105 Artemis	C	0.15 ± 0.04	0.16 ± 0.07
41 Daphne	C	0.13 ± 0.08	0.11 ± 0.04	324 Bambergia	CP	0.15 ± 0.04	0.066 ± 0.008
46 Hestia	P	0.00 ± 0.11	0.074 ± 0.024	9 Metis	S	0.14 ± 0.04	0.13 ± 0.03
78 Diana	C	0.00 ± 0.08	0.13 ± 0.04	12 Victoria	S	0.14 ± 0.03	0.22 ± 0.05
80 Sappho	S	0.25 ± 0.05	0.14 ± 0.05	41 Daphne	C	0.13 ± 0.08	0.11 ± 0.04
84 Klio	G	0.23 ± 0.06	0.15 ± 0.07	654 Zelinda	C	0.13 ± 0.03	0.18 ± 0.06
97 Klotho	M	0.23 ± 0.07	0.21 ± 0.06	356 Liguria	C	0.12 ± 0.06	0.13 ± 0.05
105 Artemis	C	0.15 ± 0.04	0.16 ± 0.07	393 Lampetia	C	0.11 ± 0.02	see text
139 Juewa	CP	0.10 ± 0.10	0.061 ± 0.025	139 Juewa	CP	0.10 ± 0.10	0.061 ± 0.025
144 Vibia	C	0.18 ± 0.10	0.11 ± 0.04	33 Polyhymnia	S	0.07 ± 0.11	0.14 ± 0.07
192 Nausikaa	S	0.00 ± 0.11	0.13 ± 0.05	19 Fortuna	G	0.06 ± 0.04	0.076 ± 0.027
194 Prokne	C	0.16 ± 0.04	0.23 ± 0.09	554 Peraga	FC	0.06 ± 0.06	0.22 ± 0.09
216 Kleopatra ^b	M	0.00 ± 0.05	0.44 ± 0.15	2 Pallas	B	0.05 ± 0.02	0.075 ± 0.011
230 Athamantis	S	0.00 ± 0.12	0.22 ± 0.09	1 Ceres	G	0.03 ± 0.03	0.041 ± 0.005
324 Bambergia	CP	0.15 ± 0.04	0.066 ± 0.008 ^d	6 Hebe	S	0.00 ± 0.12	0.16 ± 0.05
356 Liguria	C	0.12 ± 0.06	0.13 ± 0.05	46 Hestia	P	0.00 ± 0.11	0.074 ± 0.024
393 Lampetia	C	0.11 ± 0.02	see text	78 Diana	C	0.00 ± 0.08	0.13 ± 0.04
532 Herculina	S	0.37 ± 0.15	0.09 ± 0.05	192 Nausikaa	S	0.00 ± 0.11	0.13 ± 0.05
554 Peraga	FC	0.06 ± 0.06	0.22 ± 0.09	216 Kleopatra	M	0.00 ± 0.05	0.44 ± 0.15
654 Zelinda ^b	C	0.13 ± 0.03	0.18 ± 0.06	230 Athamantis	S	0.00 ± 0.12	0.22 ± 0.09
694 Ekard	CP:	0.00 ± 0.10	0.09 ± 0.04	694 Ekard	CP:	0.00 ± 0.10	0.09 ± 0.04
796 Sarita	XD	---	0.25 ± 0.10	796 Sarita	XD	---	0.25 ± 0.10

^a Weighted average disk-integrated radar properties from all existing data.

^b Stated radar properties for Ceres, Pallas, and Vesta are taken from Mitchell *et al.* (1996); those for Metis, Victoria, Kleopatra, and Zelinda are from Mitchell *et al.* (1995).

^c Stated radar properties for Iris were obtained by combining new data reported here with results derived from earlier experiments by Mitchell *et al.* (1995).

^d Radar albedo stated for Bambergia incorporates both monostatic and bistatic results from de Pater *et al.* (1994), but has been increased by 10% due to a downward revision of the IRAS diameter estimate (Tedesco 1997).

Table V (Continued)

Ordered by Descending OC Albedo

Target	Class	$\langle\mu_c\rangle$	$\langle\delta_{oc}\rangle$
216 Kleopatra	M	0.00 ± 0.05	0.44 ± 0.15
16 Psyche	M	0.17 ± 0.05	0.31 ± 0.08
796 Sarita	XD	---	0.25 ± 0.10
194 Prokne	C	0.16 ± 0.04	0.23 ± 0.09
12 Victoria	S	0.14 ± 0.03	0.22 ± 0.05
230 Athamantis	S	0.00 ± 0.12	0.22 ± 0.09
554 Peraga	FC	0.06 ± 0.06	0.22 ± 0.09
97 Klotho	M	0.23 ± 0.07	0.21 ± 0.06
5 Astraea	S	0.20 ± 0.03	0.20 ± 0.05
654 Zelinda	C	0.13 ± 0.03	0.18 ± 0.06
21 Lutetia	M	0.22 ± 0.07	0.17 ± 0.07
6 Hebe	S	0.00 ± 0.12	0.16 ± 0.05
18 Melpomene	S	0.30 ± 0.10	0.16 ± 0.05
20 Massalia	S	0.28 ± 0.07	0.16 ± 0.06
105 Artemis	C	0.15 ± 0.04	0.16 ± 0.07
84 Klio	G	0.23 ± 0.06	0.15 ± 0.07
33 Polyhymnia	S	0.07 ± 0.11	0.14 ± 0.07
80 Sappho	S	0.25 ± 0.05	0.14 ± 0.05
9 Metis	S	0.14 ± 0.04	0.13 ± 0.03
78 Diana	C	0.00 ± 0.08	0.13 ± 0.04
192 Nausikaa	S	0.00 ± 0.11	0.13 ± 0.05
356 Liguria	C	0.12 ± 0.06	0.13 ± 0.05
4 Vesta	V	0.28 ± 0.05	0.12 ± 0.04
7 Iris	S	0.18 ± 0.10	0.11 ± 0.03
41 Daphne	C	0.13 ± 0.08	0.11 ± 0.04
144 Vibia	C	0.18 ± 0.10	0.11 ± 0.04
8 Flora	S	0.16 ± 0.05	0.10 ± 0.03
27 Euterpe	S	0.34 ± 0.08	0.10 ± 0.05
532 Herculina	S	0.37 ± 0.15	0.09 ± 0.05
694 Ekard	CP:	0.00 ± 0.10	0.09 ± 0.04
19 Fortuna	G	0.06 ± 0.04	0.076 ± 0.027
2 Pallas	B	0.05 ± 0.02	0.075 ± 0.011
46 Hestia	P	0.00 ± 0.11	0.074 ± 0.024
324 Bamberga	CP	0.15 ± 0.04	0.066 ± 0.008
139 Jucwa	CP	0.10 ± 0.10	0.061 ± 0.025
1 Ceres	G	0.03 ± 0.03	0.041 ± 0.005

TABLE VI
Radar-Based Pole Constraints

Target	Obs'n. Year ^a	$B_{max}(\delta_{rad}=0)^b$	B^c	$ \delta_{rad} ^d$	Target	Obs'n. Year ^a	$B_{max}(\delta_{rad}=0)^b$	B^c	$ \delta_{rad} ^d$
5 Astraea	1983	236 ± 27	180 ± 20	0 - 57	97 Klotho	1981	77 ± 14	≥ 35	0 - 71
	1987	"	175 ± 20	0 - 58		1993-4 G	277 ± 50	310 ± 20	0 - 37
6 Hebe	1985	811 ± 61	≥ 550	0 - 54	105 Artemis	1988	219 ± 55	≥ 70	0 - 78
7 Iris	1995	3610 ± 550	2840 ± 100	0 - 53	139 Juewa ^e	1983	268 ± 53	≥ 70	0 - 79
8 Flora	1981	338 ± 36	400 ± 30	0 - 23			or	or	134 ± 27
16 Psyche	1980	1940 ± 210	840 ± 40	56 - 70	144 Vibia	1984	307 ± 40	≥ 130	0 - 70
	1985	"	875 ± 100	52 - 71			192 Nausikaa	1985	267 ± 38
18 Melpomene	1985	404 ± 52	≥ 270	0 - 58	194 Prokne	1990 G	1260 ± 250	750 ± 50	0 - 66
	1995 G	1450 ± 190	≥ 810	0 - 64			230 Athamantis	1985	135 ± 23
19 Fortuna	1982	951 ± 175	700 ± 50	0 - 59	324 Bamberga	1991 G	225 ± 15	≥ 195	0 - 30
	1986	"	≥ 330	0 - 75			804 ± 55	≥ 720	
20 Massalia	1987	567 ± 95	≥ 380	0 - 60	356 Liguria	1983	129 ± 22	≥ 115	0 - 48
21 Lutetia	1985	442 ± 75	58 ± 10	76 - 85	393 Lampetia ^f	1986	89 ± 7	100 ± 10	0 - 20
27 Euterpe	1986	414 ± 87	≥ 260	0 - 64			or	or	139 ± 44
33 Polyhymnia	1985	101 ± 19	≥ 70	0 - 60	532 Herculina	1987	720 ± 97	≥ 450	0 - 61
41 Daphne	1985	1020 ± 130	≥ 540	0 - 65	554 Peraga	1984	220 ± 40	≥ 190	0 - 51
46 Hestia	1982	170 ± 19	≥ 90	0 - 64	694 Ekard	1983	633 ± 105	≥ 250	0 - 73
78 Diana	1990	504 ± 87	465 ± 30	0 - 48	796 Sarita	1991	188 ± 37	≥ 130	0 - 60
80 Sappho	1983	183 ± 28	170 ± 40	0 - 62					
84 Klio	1985	---	≥ 105	---					

^a Year of radar observation. Goldstone observations are identified by a G.

^b Predicted maximum-breadth echo bandwidth (in Hz), taken from Table II.

^c Zero-crossing bandwidth (in Hz) of the weighted sum of all spectra. Where SNR is sufficiently high, we use the direct estimates of B listed in Table IV. For weak spectra we treat the values of B_{eq} listed in Table IV as lower bounds on B ; in cases where a point estimate and standard deviation are listed for B_{eq} , we subtract one standard deviation from the point estimate and use the result as our lower bound on B .

^d Absolute value of the sub-radar latitude (in degrees) over the duration of radar observations, computed as $|\delta_{rad}| = \cos^{-1} [B / B_{max}(\delta_{rad}=0)]$. All stated ranges are at the 95% confidence level.

^e Top and bottom entries for Juewa refer to $P = 20.9$ hr and $P = 41.8$ hr, respectively.

^f Top and bottom entries for Lampetia refer to $P = 38.7$ hr and $P = 19.35$ hr, respectively.

TABLE VII
Polarization Ratios Obtained for Iris

Year	SNR	λ (cm)	δ_{rad} ($^{\circ}$)	μ_c
1980	22	13	-69 ± 10	0.08 ± 0.03
1984	28	13	-21 ± 8	0.19 ± 0.03
1991	19	3.5	-56 ± 10	0.19 ± 0.05
1995	60	3.5	-34 ± 8	0.33 ± 0.04

TABLE VIII
A Posteriori Model for Lutetia^a

D_{IR}	Pole direction ^b		δ_{IR}	P	Ellipsoid diameters	δ_{rad}	$\langle A_{\text{proj}} \rangle$	D_{eff}	$B_{\text{max}}(\delta_{\text{rad}}=0)$
	λ	β							
96 ± 10 (4.1)	228 ± 11	$+13 \pm 5$	$+11 \pm 12$	8.16	$130 \times 104 \times 74 \pm 17\%$	$+81 \pm 5$	10600 ± 3100	116 ± 17	442 ± 75

^a Listed parameters are defined in Table II.

^b A second pole solution at $(\lambda, \beta) = (48^\circ \pm 11^\circ, +5^\circ \pm 5^\circ)$ is in only marginally poorer agreement with the optical and radar data, and yields a similar model ellipsoid.

TABLE IX
Dual-Circular vs. Dual-Linear Data for Daphne

Pol.	SNR	B_{eq} (Hz)	B (Hz)	σ_{pol} (km ²)	$\hat{\sigma}_{\text{pol}}$	μ
OC, SC	11	500 ± 20	560 ± 20	2900 ± 770	0.11 ± 0.04	0.13 ± 0.08
SL, OL	12	570 ± 30	850 ± 30	3300 ± 840	0.12 ± 0.04	0.26 ± 0.08

TABLE X
Radar Data for Artemis on Two Different Dates

Date	SNR	B_{eq} (Hz)	B (Hz)	σ_{oc} (km ²) ^a	μ_c
1988 Jun 10	20	58 ± 5	130 ± 30	1790 ± 86	0.22 ± 0.05
1988 Jun 11	20	52 ± 5	120 ± 20	1720 ± 83	0.06 ± 0.05

^a Stated errors on σ_{oc} reflect the contributions of receiver noise but not absolute calibration uncertainties, as appropriate for date-to-date comparisons.

TABLE XI
Radar Data for Lampetia by Rotation Phase Interval^a

Interval	SNR	σ_{pol} (km ²)	σ_{tot} (km ²)	μ	B_{eq} (Hz)	$B_{2\sigma}$ (Hz)	$f_{2\sigma}$ (Hz)	f_{med} (Hz)	f_{peak} (Hz)
16 OC	26	1690 ± 61	1780 ± 63	0.05 ± 0.04	70	79	-4.0	1.5	5.7
17 OC	24	1490 ± 56	1730 ± 67	0.16 ± 0.04	65	74	-3.4	6.5	17.0
18 OC	25	1490 ± 56	1670 ± 62	0.13 ± 0.04	66	80	2.3	2.5	-2.9
19 SL	20	1190 ± 56	1390 ± 64	0.16 ± 0.05	60	71	-0.5	-3.8	-11.4
20 SL	17	1070 ± 58	1140 ± 59	0.07 ± 0.06	69	77	3.4	0.8	-2.9
16 OC + 20 SL ^b	30	---	---	---	72	87	-0.8	1.3	0.0
16-18 OC	44	1550 ± 35	1730 ± 42	0.113 ± 0.023	70	91	3.7	3.2	0.0
19-20 SL	26	1130 ± 42	1260 ± 46	0.117 ± 0.037	65	79	1.5	-1.5	-2.9

^a Listed parameters include the SNR of the "polarized" (OC and/or SL) spectral sum; the polarized cross section σ_{pol} ; the total (polarized + depolarized) cross section σ_{tot} ; the polarization ratio μ = depolarized/polarized; the equivalent bandwidth B_{eq} ; the bandwidth $B_{2\sigma}$ measured between the innermost two-sigma crossing points; the frequency $f_{2\sigma}$ midway between the innermost two-sigma crossing points; the median frequency f_{med} , for which half of the integrated signal is at higher frequencies and half at lower; and the frequency f_{peak} at which the peak signal occurs. All parameters were computed for unfolded spectra. Cross sections, polarization ratios, and f_{med} were computed for unsmoothed ($\Delta f = 2.8$ Hz) spectra; $B_{2\sigma}$ and $f_{2\sigma}$ were computed for spectra smoothed to 10 Hz resolution; f_{peak} was computed for 20 Hz resolution. Listed B_{eq} values correspond to 2.8 Hz resolution for multi-date sums, and roughly 5 Hz for individual dates. These resolution values were chosen through the same procedure described for B_{eq} in footnote c of Table IV. Listed cross section uncertainties reflect only the contributions of receiver noise, as appropriate for date-to-date comparisons.

^b Due to systematic discrepancies between OC and SL cross sections (see text), no cross section or polarization ratio estimates are given for the combined "16 OC + 20 SL" spectrum.

TABLE XII
Radar Parameters by Taxonomic Class ^a

Class	μ_c				$\hat{\sigma}_{oc}$			
	mean	SD	range	N	mean	SD	range	N
BFGP	0.076	0.075	0.23	9	0.095	0.056	0.18	9
C ^b	0.123	0.054	0.18	8	0.150	0.044	0.12	7
S	0.174	0.125	0.37	14	0.147	0.043	0.13	14
M	0.155	0.107	0.23	4	0.276	0.105	0.27	5
V	0.28	---	---	1	0.12	---	---	1
<i>All</i>	0.139	0.104	0.37	36	0.152	0.078	0.40	36

^a Means, standard deviations, ranges, and sample sizes for polarization ratio and radar albedo, listed as a function of taxonomic class. Nine asteroids classified as B, FC, G, P, and CP by Tholen (1989) are grouped here as the "BFGP" sample. Sarita has been included in the M class.

^b Due to period ambiguity, Lampetia's radar albedo is highly uncertain (see Table IV) and is not included in our analysis.

TABLE XIII
Probabilities Derived From Linear Regression Analysis ^a

	BFGP	C	S	M	All
μ_C vs. D_{IR}	0.50	0.37	0.34	0.81	0.64
μ_C vs. p_V	0.66	0.36	0.49	0.22	0.025
$\hat{\sigma}_{OC}$ vs. D_{IR}	0.16	0.78	0.20	0.49	0.045
$\hat{\sigma}_{OC}$ vs. p_V	0.36	0.16	0.45	0.044	0.77
$\hat{\sigma}_{OC}$ vs. μ_C	0.49	0.63	0.16	0.046	0.71

^a Probabilities that the null hypothesis of uncorrelated variables is valid. Small values indicate significant correlations between variables.

Table XIV (Continued)

^a For each variable, eight statistical tests have been performed on our four single-class MBA samples. Each of these procedures tests a particular assumption about how this variable is distributed for the four parent MBA populations. The number listed in the table is the probability that this default assumption – the null hypothesis H_0 – is valid. Small probabilities indicate that H_0 is unlikely to be valid, and hence that an alternative hypothesis H_A is favored. H_A generally involves parent distributions which differ from each other or from a particular theoretical distribution. The null and alternative hypotheses for our tests are listed below:

Shapiro-Wilk:

- H_0 : The parent population for this taxonomic class has a normal distribution in this variable.
- H_A : The parent population for this taxonomic class does not have a normal distribution in this variable.

Levene's test:

- H_0 : The four single-class parent populations have equal variance in this variable.
- H_A : At least two of the four single-class parent populations have different variances in this variable.

Kruskal-Wallis test:

- H_0 : The four single-class parent populations have identical distributions in this variable.
- H_A : The four single-class parent populations have identical distributions in this variable, except that at least two of the four medians differ from each other.

Dunn's *post hoc* test (performed after the Kruskal-Wallis test):

- H_0 : The two single-class parent populations being considered have identical distributions in this variable.
- H_A : The two single-class parent populations being considered have identical distributions in this variable, except that the medians differ from each other.

one-way unblocked analysis of variance (ANOVA):

- H_0 : The four single-class parent populations have identical normal distributions in this variable.
- H_A : The four single-class parent populations have identical normal distributions in this variable, except that at least two of the four means differ from each other.

Newman-Keuls, Tukey "honestly significant difference," and Scheffé *post hoc* tests (performed after ANOVA):

- H_0 : The two single-class parent populations being considered have identical normal distributions in this variable.
- H_A : The two single-class parent populations being considered have identical normal distributions in this variable, except that the means differ from each other.

TABLE XV
MBA Near-Surface Densities by Taxonomic Class

Class	$\hat{\sigma}_{OC, spec} =$ $\hat{\sigma}_{OC} (1 - 2 \mu_C)$	$R =$ $\hat{\sigma}_{OC, spec} / 1.2$	d_{bulk} (g cm ⁻³)	d_{solid} for $p = 0.5$ (g cm ⁻³)
BFGP	0.079 ± 0.046	0.066 ± 0.038	1.7 ± 0.6	3.4 ± 1.2
C	0.112 ± 0.031	0.093 ± 0.026	2.0 ± 0.3	4.0 ± 0.6
S	0.100 ± 0.055	0.083 ± 0.046	1.9 ± 0.7	3.8 ± 1.4
M	0.213 ± 0.158	0.178 ± 0.132	2.9 ± 1.5	5.8 ± 3.0

TABLE XVI

Main-Belt Asteroid Radar Opportunities at Arecibo, 1999-2001

Asteroid	Peak-SNR Date	Dist. (AU)	H	Class	Diam. (km)	Per. (hr)	RA, Dec. (°)	SNR	Asteroid	Peak-SNR Date	Dist. (AU)	H	Class	Diam. (km)	Per. (hr)	RA, Dec. (°)	SNR
200 Dynamene	1999 1 18.1	1.598	8.3	C	128	19	126, 24	35	324 Bamberg	2000 9 22.4	1.050	6.8	CP	229	29	49, 35	356
313 Chaldaea	1999 1 29.5	1.167	8.9	C	96	8	87, 5	42	914 Palisana	2000 9 28.4	1.259	8.8	CU	77	16	326, 33	30
739 Mandeville	1999 2 3.3	1.442	8.5	X	107	12	145, 15	30	111 Ate	2000 10 2.8	1.637	8.0	C	135	22	3, 9	30
19 Fortuna	1999 2 6.8	1.523	7.1	G	200	7	146, 11	50	391 Ingeborg	2000 10 14.7	0.655	10.1	S	30	16	24, 20	113
4 Vesta	1999 2 7.8	1.463	3.2	V	510	5	139, 23	198	192 Nausikaa	2000 10 18.0	0.835	7.1	S	103	14	26, 22	257
10 Hygiea	1999 2 20.5	2.111	5.4	C	407	28	147, 9	73	12 Victoria	2000 10 20.5	1.238	7.2	S	113	9	36, 20	54
8 Flora	1999 3 26.3	1.498	6.5	S	136	13	191, 6	51	30 Urania	2000 10 26.0	1.072	7.6	S	100	14	31, 17	92
404 Arsinoe	1999 4 11.8	1.140	9.0	C	98	9	204, 17	58	230 Athamantis	2000 10 26.6	1.251	7.4	S	109	24	30, 20	82
387 Aquitania	1999 5 7.3	1.449	7.4	S	100	24	221, 16	38	16 Psyche	2000 12 1.8	1.668	5.9	M	253	4	75, 18	32
41 Daphne	1999 5 21.8	1.085	7.1	C	174	6	251, 6	113	38 Leda	2000 12 24.4	1.349	8.3	C	116	13	91, 28	43
105 Artemis	1999 6 4.4	1.070	8.6	C	119	17	262, 16	134	128 Nemesis	2000 12 27.2	1.666	7.5	C	188	39	103, 27	62
737 Arequipa	1999 8 6.3	0.990	8.8	S	44	14	321, 4	30	505 Cava	2001 1 6.6	1.174	8.6	FC	115	8	119, 27	62
219 Thusnelda	1999 8 24.3	0.854	9.3	S	41	30	322, 5	74	145 Adcona	2001 3 22.1	1.494	8.1	C	151	8	194, 16	37
198 Ampella	1999 9 10.5	0.919	8.3	S	57	10	340, 12	65	13 Egeria	2001 3 26.7	1.486	6.7	G	208	7	193, 13	56
85 Io	1999 9 30.4	1.256	7.6	FC	155	7	12, 10	63	532 Herculina	2001 4 19.9	1.377	5.8	S	222	9	219, 14	93
13 Egeria	1999 11 13.1	1.514	6.7	G	208	7	44, 20	43	2 Pallas	2001 5 6.3	2.259	4.1	B	525	8	257, 23	45
216 Kleopatra	1999 11 16.3	1.142	7.3	M	135	5	61, 11	72	74 Galatca	2001 8 14.3	1.260	8.7	C	119	9	351, 1	31
59 Elpis	1999 11 24.8	1.496	7.9	CP	165	14	68, 8	43	253 Mathilde	2001 8 19.5	0.992	10.2	C	58	418	353, 2	212
249 Ilse	1999 12 9.5	1.067	11.3	?	35	85	42, 35	34	54 Alexandra	2001 9 7.3	1.338	7.7	C	166	7	351, 10	57
29 Amphitrite	1999 12 9.7	1.404	5.9	S	212	5	77, 33	47	407 Arachne	2001 9 10.7	1.465	8.9	C	95	44	345, 5	35
554 Peraga	1999 12 23.1	1.066	9.0	FC	96	14	96, 25	88	270 Anahita	2001 9 19.5	0.891	8.8	S	51	15	0, 5	63
6 Hebe	1999 12 31.9	1.263	5.7	S	185	7	73, 1	54	19 Fortuna	2001 9 20.0	1.101	7.1	G	200	7	5, 4	141
14 Irene	2000 1 4.5	1.494	6.3	S	167	15	96, 27	57	67 Asia	2001 9 21.3	1.119	8.3	S	58	16	6, 7	32
18 Melpomene	2000 1 8.9	1.269	6.5	S	141	12	119, 10	68	36 Atalante	2001 10 2.4	1.071	8.5	C	106	10	40, 34	65
7 Iris	2000 1 23.9	1.248	5.5	S	200	7	135, 9	95	704 Interamnia	2001 10 10.3	1.688	5.9	F	317	9	5, 32	58
98 Ianthe	2000 2 21.3	1.203	8.8	CG	104	16	155, 23	73	247 Eukrate	2001 10 18.5	1.161	8.0	CP	134	12	14, 28	98
288 Glauke	2000 2 28.8	1.338	9.8	S	32	1150	154, 15	63	60 Echo	2001 10 29.8	1.192	8.2	S	60	25	27, 9	35
45 Eugenia	2000 3 16.0	1.607	7.5	FC	215	6	174, 8	32	66 Maja	2001 11 12.6	1.201	9.4	C	73	10	48, 22	33
1 Ceres	2000 3 22.2	1.601	3.3	G	933	9	189, 15	467	211 Isolda	2001 11 14.6	1.607	7.9	C	143	18	46, 21	39
2 Pallas	2000 4 5.7	1.680	4.1	B	525	8	120, 0	66	11 Parthenope	2001 11 15.9	1.476	6.6	S	153	8	59, 13	38
146 Lucina	2000 4 7.6	1.603	8.2	C	132	19	201, 13	35	4 Vesta	2001 11 26.8	1.589	3.2	V	510	5	65, 14	149
51 Nemausa	2000 4 7.7	1.225	7.4	CU	148	8	187, 2	48	712 Boliviana	2001 12 16.1	1.194	8.3	C	128	12	92, 9	72
393 Lampetia	2000 8 23.4	0.977	8.4	C	97	39	333, 16	226	40 Harmonia	2001 12 16.8	1.266	7.0	S	108	9	88, 22	46
88 Thisbe	2000 9 19.9	1.448	7.0	CF	201	6	1, 10	53									

Note. SNR values refer to weighted spectral sums for a single observing date, and are estimated using asteroid properties tabulated in the JPL Horizons data base and nominal values for Arecibo radar system performance. Only opportunities with single-date SNR > 30 are listed. Note that all but four of the experiment-summed SNR values listed in Table IV for previous observations are less than 30.